DOCTOR OF PHILOSOPHY

Models for Testing Contemporary Ultrasound Systems

Joy, Joyce

Award date:
2016

Models for Testing Contemporary Ultrasound Systems

Joyce Joy

January 2016

A thesis submitted to the University of Dundee for the degree of Doctor of Philosophy

To my loving husband and dear parents

Table of Contents

ACKNOWLEDGEMENTS

This thesis would have remained a distant dream has it not been for several wonderful people. First and foremost, I would like to express my deepest gratitude to Prof. Sandy Cochran, my supervisor. I have been very fortunate to have his expertise, experience, enthusiasm, valuable support and guidance in making this possible. There were times when I crumbled and struggled and without his helping hand, this would never have been possible. Thank you Sandy for being the best supervisor and mentor I ever had.

I am also indebted to Prof George Corner, my second supervisor and guide for his immense help and advice throughout my project. He has always been there for me whenever I needed him. Special thanks to Dr. Sarah Vinnicombe for her immense help and support during past one year for the therapeutic ultrasound work. I would also like to thank Mr David Lines, Diagnostic Sonar Ltd for his invaluable support and help in improving the Dynamic Phantom. I would also like to thank Dr. Paul Bibire, University of St. Andrews for his significant help in proofreading this thesis.

I would also like to acknowledge other wonderful people I met on my way, which taught me so much both professionally and personally, some of them are: Dr. Graeme McLeod, Dr. Roos Eisma, Dr. Christine Demore, Dr. Zhihong Huang, Dr. Robert Ssekitoleko, Mr. Ioannis Karakitsios and Dr. Shaozhen Song.

More than anyone, I would like to thank to my brother, in-laws and friends, especially, Dr. Praveen Cheriyan Ashok and Dr. Bavishna Balagopal for motivating and supporting me. On a personal note, I would like to express my thanks to my dear parents for instilling the importance of education in me from my childhood and encouraging me to dare to dream. Last, but definitely not the least, my loving husband, Manu without whom I would not have come this far. Thank you dear for being patient and for not giving up on me.

CERTIFICATION

This is to certify that Joyce Joy has complied with all the requirements for the submission of this Doctor of Philosophy thesis to the University of Dundee,

Supervisor: Prof. Sandy Cochran

Signature: 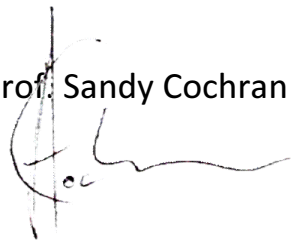 Date: 20.01.2016

DECLARATION CONCERNING THESIS PRESENTED FOR THE DEGREE OF

DOCTOR OF PHILOSOPHY

I *Joyce Joy*,

solemnly and sincerely declare, in relation to the thesis entitled:

Models for testing Contemporary Ultrasound Systems,

that I am the author of this thesis, that all references cited have been consulted by me; that the work of which the thesis is a record has been done by me, and that the material has not previously been accepted in whole, or in part, for any other degree or diploma.

Signature:  Date: 20.01.2016

LIST OF FIGURES

LIST OF TABLES

LIST OF ABBREVIATIONS

AIUM	American Institute of Ultrasound in Medicine
APS	Ammonium Peroxodisulfate
ARF	Acoustic Radiation Force
CAHiD	Centre of Anatomy and Human Identification
cm	Centimeter
CT	Computed Tomography
dB	Decibels
DoE	Days of Embalming
FDA	Food and Drug Administration
FEC	Formalin Embalmed Cadavers
FFC	Fresh Frozen Cadavers
FSGE	Fast Spoiled Gradient Echo
FUS	Focused Ultrasound Surgery
H&E	Haematoxylin and Eosin
HIFU	High Intensity Focused Ultrasound
IP	In-plane
KPa	Kilo Pascal
LMM	Linear Mixed Models
MESH	Medical Subject Heading
MHz	Megahertz
mm	Millimetres
ms	Milliseconds
MRgFUS	MR guided Focused Ultrasound Surgery
MRI	Magnetic Resonance Imaging
NDT	Non-Destructive Testing
NHS	National Health Service
OCE	Optical Coherence Elastography
OCT	Optical Coherence Tomography
OP	Out-of-plane
PBS	Phosphate Buffer Solution
PhS-OCT	Phase Sensitive Optical Coherence Tomography
PRF	Proton Resonance Frequency
PRFS	Proton Resonance Frequency shift
QA	Quality Assurance
REML	Restricted Maximum Likelihood
RF	Radio Frequency
ROI	Region of Interest
RTE	Real-time Tissue Elastography
Rx	Receiver
SONAR	Sound Navigation and Ranging
SPL	Spatial Pulse Length
SSI	Supersonic Shear Imaging
SWE	Shear Wave Elastography
SW-OCE	Shear Wave Optical Coherence Elastography
T_E	Echo Time

T_R	Repetition Time
TEC	Thiel-embalmed Human Cadaver
TMM	Tissue Mimicking Materials
Tx	Transmitter
UFAW	Universities Federation for Animal Welfare
UGRA	Ultrasound Guided Regional Anaesthesia
US	Ultrasound
W	Watts
µUS	Microultrasound
2D	Two dimensional
3D	Three dimensional

ABSTRACT

Medical ultrasound systems are undergoing continuous development. Five areas of particular recent interest are shear wave elastography, interventional ultrasound, microultrasound, and therapeutic ultrasound. These new developments motivate demand for new tissue models. The work discussed in this thesis presents different tissue models for these areas of contemporary ultrasound systems development.

Acoustic test objects, known as phantoms, are the most widely used basis for testing medical ultrasound systems, but they have many limitations. Hence, the recent advancement in medical simulation, soft-embalmed Thiel human cadaver models being considered for their suitability as a model for testing shear wave elastography and interventional ultrasound systems. The results indicate significant similarities between the Thiel-embalmed cadavers, and human's *in-vivo* tissues in relation to their tissue stiffness measured with SWE. The use of these cadaveric models has also shown to bring benefits for interventional ultrasound systems testing and research. This is demonstrated with two specific case studies on ultrasound guided regional anaesthesia.

Another aspect considered in this work is the suitability of Thiel-embalmed human breast tissues for testing therapeutic ultrasound systems. The results indicate that these models are unsuitable for therapeutic ultrasound systems testing because of their inability to produce lesions during sonication which can be seen visually or under histopathological examination. For testing microultrasound systems, mice preserved with the Thiel method have been assessed and shown to be a suitable model because of its small size, reusability and easier accessibility. This thesis has assessed the use of preserved human and animal tissue models for testing contemporary ultrasound systems.

CHAPTER 1

Introduction

1.1 MODELS FOR TESTING CONTEMPORARY US SYSTEMS

Medical ultrasound systems are developing continuously. With the contemporary developments in the ultrasound (US) field such as the use of US for interventional (Buscarini 2011) and therapeutic (Crum 2010) purposes and the development of newer imaging techniques such as shear wave elastography (SWE) (Bercoff 2004) and microultrasound (μUS) systems, there is an increasing demand for new tissue models and testing methods. This thesis aims at looking into new tissue models for testing four areas of US developments: SWE, interventional US, high frequency μUS imaging and therapeutic US systems.

SWE is a recent development in the elastography field which can produce quantitative stiffness maps of tissue (Bercoff 2004, Bercoff 2010). Because of the changes in the elasticity of cancerous tissue compared to the healthier tissue, SWE is currently widely used for the diagnosis of breast cancer (Evans 2010). Current methods of testing these systems use acoustic test objects made of tissue mimicking materials (TMMs) with varying stiffnesses.

Another development in the application of US is its use for interventional purposes. Interventional ultrasound, i.e., US-guided interventions, refers to diagnostic or therapeutic minimally invasive procedures guided by real-time US imaging (Holm and Skjoldbye 1996). An example is the use of US in guiding needles during regional anaesthesia. Ultrasound guided regional anaesthesia (UGRA) has been used clinically for over two decades and is still being developed in various ways (Andrew 2006), particularly in clinical procedures. Currently the testing of these interventional procedures makes use of basic TMMs.

High frequency μUS imaging has become an important imaging tool for many clinical and pre-clinical applications that requires high resolution imaging. This technique offers imaging resolution in the order of several tens of micrometers. Imaging systems for μUS have been developed extensively in recent years (Qiu 2013). Basic TMMs and wire phantoms are currently being used for testing these systems.

Along with its use as an imaging technique, therapeutic uses of US has also seen development in the recent years, owing to its capability of focusing the US energy to

very small diameters (in the order of a few millimetres) using High Intensity Focused Ultrasound (HIFU) transducers. This has led to demand for this technology in the field of Focused Ultrasound Surgery (FUS). FUS has seen several clinical applications in the past 20 years, especially in treating prostate cancer, breast cancer, pancreatic cancer and for liver and kidney tumours and for uterine fibroids (Kennedy 2003). The standard testing approach for these therapeutic US systems uses heat sensitive TMMs and acoustic test objects with inclusions (Takegami 2004).

1.2 MOTIVATION

Most of the new US technologies uses acoustic test objects that contains TMM with embedded targets or inclusions during system development. Even though the TMM-based acoustic test objects are readily available, they have several limitations when used for US research and testing. One of the major limitations is the anatomical differences they have when compared to that of the human body.

This leads to an unmet need for a qualitative, anatomical model during testing and development of US systems. One of the options is to use human cadavers as test objects for medical research as a substitute for *in-vivo* human tissue. Human cadavers are available in various forms such as fresh frozen cadavers (FFC) (Kang 2009), formalin embalmed cadavers (FEC) (Balta 2014) and soft-embalmed cadavers. Unlike with FFC and FEC, it may be possible to obtain US images of soft-embalmed human cadaveric tissues considering the way it is preserved.

Because of their US compatibility and anatomical similarity, these soft-embalmed cadavers might be a suitable model during testing and development of US systems. This thesis primarily focuses on characterising cadavers embalmed using a particular soft-embalming technique called Thiel embalming (Thiel 1992a, Thiel 1992b, Thiel 2002) to assess their suitability in using them as a test phantom for contemporary US technologies. The suitability of these phantoms for various aspects such as US diagnostic, therapeutic and intervention are separately assessed.

1.3 CONTRIBUTIONS TO KNOWLEDGE

This thesis discusses and analyses different models and techniques for research and testing of US systems. As such, the work on which it is based has contributed to knowledge in a number of distinct areas within the same overall domain.

As discussed in the previous section, the most commonly used TMMs have several limitations. To understand further and to create a baseline, it was necessary to evaluate these tissue mimics and the work discussed in this thesis started by preparing and characterising the most commonly used TMMs. A wide range of TMMs were prepared and tested in the laboratory, together with their acoustical and mechanical properties. The dissertation also collects the detailed recipes of the various TMMs together in Appendix I.

Irrespective of the wide use of acoustic test objects with artificial TMMs, the need for an anatomically significant, qualitative tissue model for US systems testing still remains. A feasible solution would be to use Thiel-embalmed human cadavers (TEC). The work discussed in this thesis has assessed the suitability of TEC for their use as a model for testing various different areas of US development.

The suitability of the TEC models for testing SWE system is evaluated by conducting a quantitative analysis of TEC tissue stiffness and comparing the results with the *in-vivo* human volunteer data. TEC models embalmed in tank and bags were selected for the study. It was shown that the TEC models embalmed in bags appeared stiffer and hence varied significantly with the *in-vivo* human tissue stiffnesses. However, the results indicate good similarity between the tissue stiffness values of the TEC embalmed in tanks and human volunteers (Joy 2015).

The suitability of the TEC model for US interventional research was assessed using two case studies. The first case study assessed TEC for a specific nerve stiffness study and the results supported the use of SWE system for nerve blocks in UGRA because of significant differences between the neural and extraneural tissue (Johnson 2009, Munirama 2012, Munirama 2013). The second case study used the TEC model to study the visibility of different types of needles, when used for UGRA nerve blocks. Technical, discrete studies like needle insertion cannot be conducted on human volunteers for

ethical reasons. A good tissue model like TEC with similar anatomical detail and needle feedback is extremely important. The results from the case studies indicate that TEC model is extremely beneficial for interventional US research (Munirama 2015).

The suitability of TEC breast tissue for pre-clinical breast cancer therapeutic US research was also assessed. The results indicated that the TEC model may not be suitable for breast cancer research as it failed to produce any lesions on sonicating. This was later explained to be because of differences in the US attenuation coefficient values between the two. The study recommended using fresh human *ex-vivo* or *in-vivo* animal models for breast HIFU pre-clinical trials (Joy 2015b).

In order to meet the demand for a small, anatomical model for testing high frequency, µUS systems, readily accessible, qualitative, reusable Thiel mice models were considered. Different embalming protocols were tested to find the optimum embalming procedure. It was observed that the Thiel protocol used in embalming human cadavers was suitable for embalming small animals like mice, preserving its anatomical characteristics. Among the various protocols tried, mice embalmed with the original Thiel protocol showed the greatest similarity to fresh dead mice in terms of organ and tissue preservation and mechanical properties (Song 2015).

1.4 OUTLINE OF THE THESIS

This thesis is about US models for testing contemporary US systems. Because of the multidisciplinary nature of the work presented and to make the thesis as useful as possible for readers from different backgrounds, it is divided into two main sections.

Section I discusses the general theory and specific literature for each further part of the work detailed in the next two sections. The section consists of two Chapters: Chapters Two and Three. The broad introduction of medical US given in Chapter Two includes a review of medical US imaging, interventional US and therapeutic US. This Chapter discusses literature to provide basic understanding for introducing the reader to the terminologies used in the rest of the thesis. The focus of Chapter Three is on artificial ultrasound test objects and TMMs. This Chapter discusses different TMMs and their US characteristics.

Section II presents all the work done in assessing the suitability of qualitative TEC models for supporting US research and development. There are four Chapters in Section II: Chapters Four to Seven.

Chapter Four reports the use of SWE with the TEC models and begins with a background section on human cadaver models. This is followed by a specific case study to assess quantitatively the tissue stiffnesses of TECs using SWE. Chapter Five demonstrates the use of TEC as a model for interventional US research using two case studies. The Chapter begins with a brief background, followed by two main sections each devoted to an individual case study.

Chapter Six assesses the use of TEC breast tissue for therapeutic US breast cancer research. The Chapter begins with a background section on breast cancer and MRI guided focused ultrasound surgery (MRgFUS) and is followed by the experiments to compare TEC breast tissue with fresh human breast tissue. Chapter Seven is dedicated to demonstrating the possibilities of using a Thiel-embalmed mouse model as an easily accessible ultrasound TMM for high frequency systems testing. This Chapter begins by describing embalming protocols and two case studies demonstrating the use of Thiel mice during the development of high frequency, μUS systems is described further.

Having covered several topics in areas related to US models in contemporary research, Chapter Eight seeks to draw conclusions about these aspects and discusses the future outlook in each specialist area.

1.5 LIST OF PUBLICATIONS

Peer Reviewed

Joy J, McLeod G, Lee N, Munirama S, Eisma R, Corner GA, Cochran S. Quantitative analysis of Thiel human cadavers using shear wave elastography. Annals of Anatomy. 202: 52-56.

Joy J, Riedel F, Valente AA, Cochran S, and Corner GA (2014). Automated performance assessment of ultrasound systems using a dynamic phantom. Ultrasound. 22: 199-204.

Munirama S, **Joy J**, Columb M, Habeshaw R, Eisma R, Corner GA, Cochran S and McLeod G (2015). A randomised, single-blind technical study comparing the ultrasonic visibility of smooth-surfaced and textured needles in a soft embalmed cadaver model. Anaesthesia. 70: 537–542.

Munirama, S, **Joy J**, Eisma R, Corner GA, Cochran S and McLeod, G (2013). Shear Wave Elastography: Novel Technology for Ultrasound-guided Regional Anesthesia. Anesthesiology. 119(3): 698.

Proceedings

Joy J, Riedel F, Valente AA, Cochran S, and Corner GA (2011). Validation of an automated dynamic phantom to assess the performance of ultrasound system. Fourth International Conference on Biomedical Engineering and Informatics (BMEI), October 15-17, Shanghai, 4: 2355-2359.

Joy J, Yang Y, Karakitsios I, Eisma R, Purdie C, Melzer A, Cochran S and Vinnicombe, S. “Soft-embalmed Human Breast Tissue as a Model for Pre-clinical Trials of HIFU - Preliminary Results.” Journal of Therapeutic Ultrasound 3 (Suppl 1): P44-P44.

Song, S, **Joy J**, Wang R, Huang Z. Mapping tissue shear modulus on Thiel soft-embalmed mouse skin with shear wave optical coherence elastography. Optical Elastography and Tissue Biomechanics II. 9327: 1-6.

Munirama S, **Joy J**, Columb M, Habeshaw R, Eisma R, Corner GA, Cochran S and McLeod G (2012). A comparison of intraneural and extraneural shear modulus in the Thiel-embalmed human cadaver. Anaesthesia 67(11): 1294-1294.

Munirama S, **Joy J**, Columb M, Habeshaw R, Eisma R, Corner GA, Cochran S and McLeod G (2011). Visibility of echogenic and non-echogenic needles in the Thiel cadaver. British Journal of Anaesthesia 107(5): 836-836.

Oral and Poster Presentations

Joy J, Lee N, Demore C, Cui L, Munirama S, Eisma R, Corner GA, McLeod G, Cochran, S (2014). Quantitative assessment of soft embalmed human cadavers with ultrasound shear wave elastography. Proceedings of the 12th International Tissue Elasticity Conference, October 1-4, Lingfield, UK. pp 104.

Joy J, McLeod G, Lee N, Munirama S, Eisma R, Corner GA, Cochran S (2013). Quantitative assessment of soft embalmed human cadavers with ultrasound shear wave elastography. Bio-Engineering Conference, September 16th-18th, Glasgow, UK.

Joy J, Kotopoulis S, Wang H, Mulvana H, Bush N, Bamber J, Cochran S (2012). Assessment of the mouse model for pre-clinical development of focused ultrasound surgery. The 44th Annual Meeting of the British Medical Ultrasound Society, December 10-12, Telford, UK.

Joy J, Yang Y, Karakitsios I, Eisma R, Purdie C, Melzer A, Cochran S and Vinnicombe, S (2014). A feasibility study of soft embalmed human breast tissue for pre-clinical trials of HIFU – Preliminary results. 14th International Symposium on Therapeutic Ultrasound, April 2 – 5, Las Vegas, USA. pp 260.

Joy J, Riedel F, Valente AA, Cochran S, and Corner GA (2011). Automated Transducer Testing and Calibration with a Dynamic Phantom. IEEE International Ultrasonic Symposium, October 18-21, 2011, Caribe Royale, Orlando, Florida, USA.

Joy J, Lee N, Liao X, Corner G, Huang Z, Eisma R, Cochran S. Quantitative Comparison of Tissue Mimicking Materials for Ultrasound Imaging and Therapy. The 44th Annual Meeting of the British Medical Ultrasound Society, December 10-12, Telford, UK.

SECTION I

Background

This is the first section of the thesis and the Chapters in this section aim to provide all the necessary background to understand the work presented in the next two sections. This section consists of two Chapters.

Chapter Two introduces general background and theory as common foundations of all the techniques and procedures used for the work. Specific literature required to understand different Chapters is provided elsewhere, in the corresponding Chapter background sub-sections.

Chapter Three introduces different artificial ultrasound phantoms and their acoustic and mechanical characteristics. This Chapter also provides results of acoustical and mechanical characterisation of several TMMs prepared during the present work.

CHAPTER 2

Literature Review

2.1 HISTORY OF ULTRASOUND

Ultrasound is the term applied to mechanical pressure waves with frequencies above 20,000 Hz, i.e. beyond the audible range (Lutz 2011). The development of US can be dated back to the 1720's when Lazzaro Spallanzani, an Italian priest and physiologist, provided experimental evidence about the non-audible sound existing around us (Joseph 1995). He demonstrated that blindfolded bats navigated around obstacles in the dark using sound waves rather than light. However, the real breakthrough in US technology was in 1880 with the discovery of the piezoelectric effect by Pierre and Jacques Curie from France. This led to the development of ultrasonic transducers which are a key component in any US system.

During the Second World War, of under-water sound navigation and ranging (SONAR) devices named hydrophones were invented for submarine detection. The development of medical US can be traced back to the 1940s, when thermal energy generated from US was used in ultrasonic therapy (hyperthermia). US was then used to treat conditions such as arthritic pain, ulcers, asthma and urinary incontinence.

Prior to the use of US in diagnostics, US was applied as a therapeutic tool in physical therapy. HIFU is now a growing field which has been employed clinically from the 1950s. In 1952, it was reported that HIFU could be used to treat glaucoma. The use of HIFU as a therapeutic tool has shown fast development in the past ten years. The capability of HIFU transducers to focus the US energy to very small diameters, in ranges down to a few microns, has made this technology of interest in the field of FUS.

US was first used as medical diagnostic tool in 1942 by Karl Dussik, a neurologist from the University of Vienna, to locate brain tumours and cerebral ventricles (Joseph 1995). Since then, developments in the medical US field have been so remarkable that US imaging is now a well-established technology in medical field, confirmed by the fact that it accounts for around one in four of all imaging procedures worldwide (Wells 2006). Figure 1 shows the growth in the number of US, Computed Tomography (CT) and Magnetic Resonance Imaging (MRI) imaging tests in England over last two decades, clearly indicating the numerical increase of US over CT and MRI.

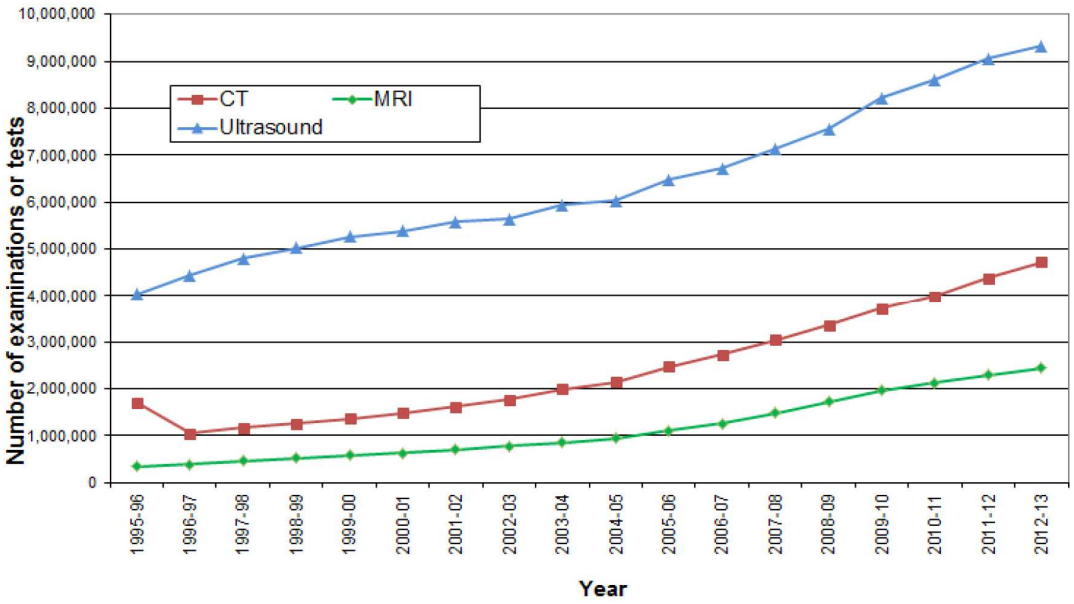

Figure 1: Growth in the number of US, CT and MRI imaging exams in England from 1995-96 to 2012-13 indicating the significant increase of US imaging compared to CT and MRI (National-Statistics 2013).

Figure 2 shows the hierarchical tree showing the various technologies and developments based on US. The three main areas that use US are non-destructive testing (NDT), SONAR and medical US. The highlighted boxes in the Figure are the main areas of interest for this thesis and will be described in detail in this Chapter. The four main areas where the testing methods have been assessed are B-mode imaging, therapeutic US, interventional US, SWE and high frequency µUS imaging.

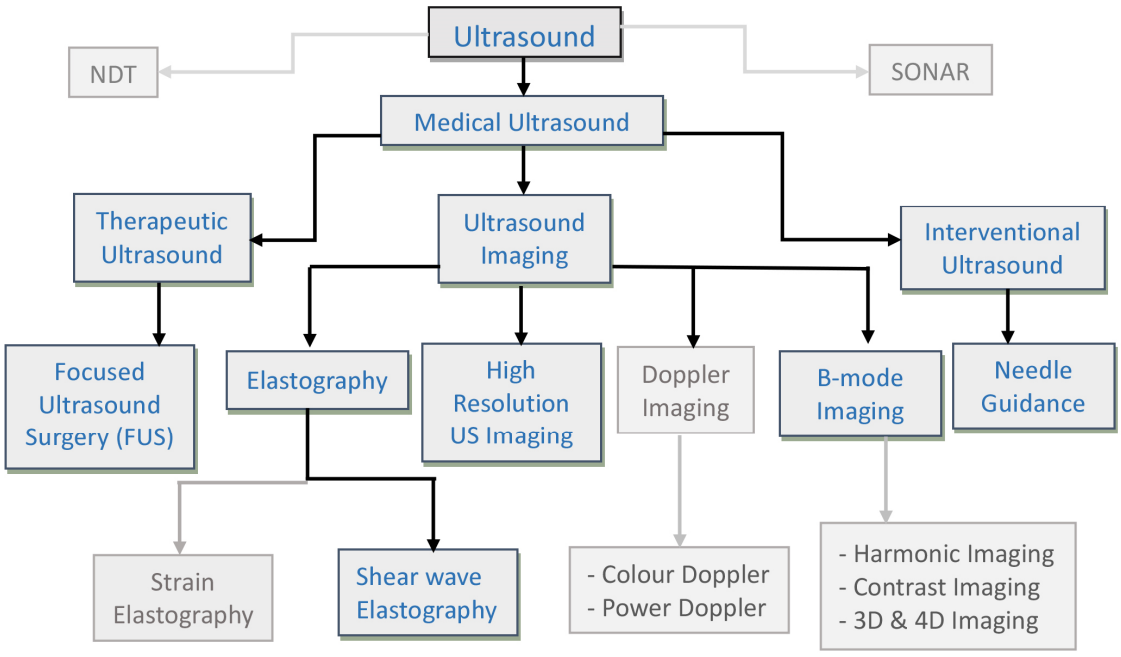

Figure 2: Developments in the field of US.

2.2 GENERATION AND PROPAGATION OF US

Piezoelectric materials are able to convert mechanical vibrations into electrical energy in a process termed the piezoelectric effect. Conversely, when a voltage is applied to the piezoelectric material, mechanical vibrations are produced, resulting in the transmission of US waves to the surrounding medium in a process termed the inverse piezoelectric effect. Typical simple US transducers are made of thin discs of an artificial ceramic material such as lead zirconate titanate whose thickness determines the resonant frequency (Mikla and Mikla 2014).

US causes molecules in the medium to vibrate as it propagates. US can travel in four modes in solids, based on the direction of displacement of particles, i.e. longitudinal (or compressional) waves, transverse (or shear) waves, surface waves, and, in thin materials, plate waves. The most commonly used modes of propagation in US imaging are longitudinal and shear waves. Within the waves, regular pressure variations occur, resulting in compression i.e. regions of high pressure and high amplitude, and rarefaction i.e. low pressure zones (ter-Haar and Duck 2000) (Figure 3). The orange to blue colour change indicates the movement of the wave and the direction of its propagation.

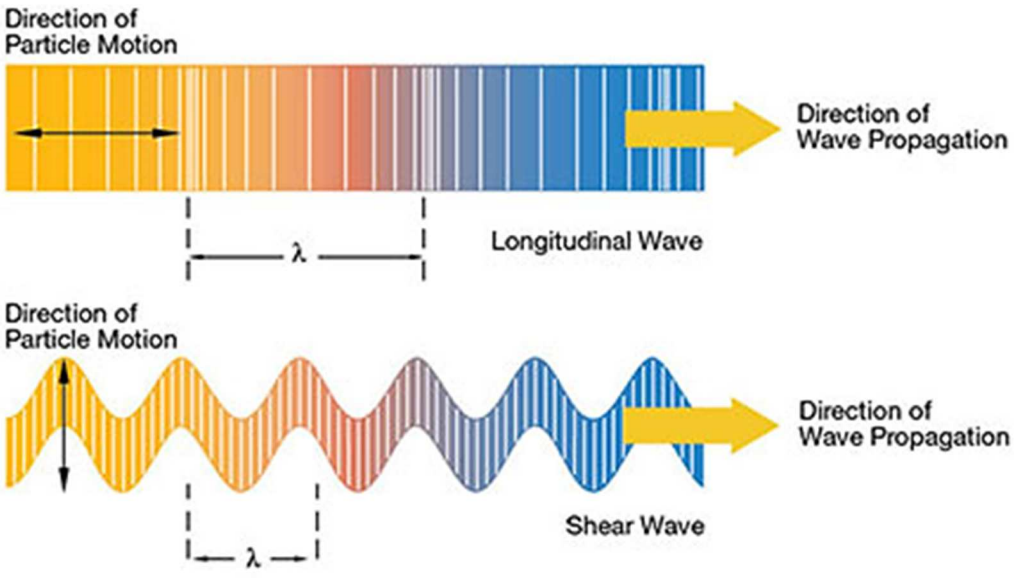

Figure 3: US wave propagation

For longitudinal waves, the distance between two adjacent compressions (or rarefactions) determines the wavelength, λ. Whereas for shear waves, λ is the distance

between two adjacent peaks and the frequency, *f* in both cases can be calculated by knowing the propagation velocity, *c*, using Equation 1.

$$f = {}^{c}/_{\lambda} \quad (1)$$

The value of *c* depends on the mechanical properties of the medium. The average speed of ultrasound longitudinal waves in tissue is taken to be 1540 $m.s^{-1}$. Shear waves have a slower velocity (1 to 10 $m.s^{-1}$) and shorter wavelength than longitudinal waves of the same frequency.

2.2.1 Acoustic Power and Intensity

The total acoustic power emitted by US is of great importance for the safe use of US imaging. Acoustic power is the rate of energy emitted by a transducer every second. It is measured in joules/second i.e. watts (W). In the case of diagnostic beams, acoustic power varies from as little as 1 mW to few hundred mW (Martin and Ramanarine 2010). Like acoustic power, the knowledge of the distribution of power throughout the scan plane of an US beam is also highly important, as there could be regions of high intensity in the non-uniform US beam which would heat some regions more strongly than the surrounding tissues. These differences in power can be calculated by averaging the acoustic power over an area and this is described as acoustic intensity, with the unit of $W.cm^{-2}$ (ter-Haar and Duck 2000).

2.2.2 Acoustic Impedance

Acoustic impedance, *Z*, is a material characteristic and is a measure of how sound propagates through a material. It is a physical representation of how the wave energy is shared between elastic and inertial components as it propagates through the material. *Z* depends on the physical characteristics of the material, bulk modulus and density. It is related to the material density, ρ, and acoustic velocity, *c* as shown in Equation 2:

$$Z = \rho . c \quad (2)$$

Changes in acoustic impedance control transmission and reflection at material interfaces. The greater the acoustic mismatch, the greater the percentage of US reflected and the less transmitted. Soft tissue/bone and soft tissue/air interfaces are examples. *Z* for soft tissue (average) is 1.63 MRayl and for bone is 7.38 MRayl and the percentage amplitude reflection is approximately 41%. *Z* for air is about 0.0004 and

hence the percentage amplitude reflection at soft tissue/air interface is approximately 99.9% (Nimrod 2005) Further description of reflection coefficient is given in section 3.4.

2.2.3 Attenuation

Attenuation is the reduction in the intensity of an US signal as it traverses a medium. It occurs because of the absorption of US energy by conversion to heat, reflections, refractions, scattering and diffraction, all well-known optical phenomena. US is heavily attenuated and this attenuation increases markedly with frequency reducing the penetration depth. The total attenuation in a medium is generally defined in the clinical domain in terms of the distance within the medium at which the strength/intensity of ultrasound is reduced to half its initial value, termed the 'half-value thicknesses' (Lutz 2011).

Attenuation in soft tissues is approximately 0.5 decibels (dB) per centimetre (cm) of tissue per megahertz (MHz) (Browne 2003). Likewise the dependency of acoustic mismatch on amount of beam reflection, the acoustic speed differences between media cause the transmitted beam to undergo refraction or bending. The reduction in acoustic intensity because of beam spreading with increasing depth relates to diffraction. As air and gas reflect almost all the US energy, an acoustic shadow is formed behind gas bubbles and hence US is not suitable for imaging tissues containing air, such as the lungs.

2.3 US IMAGING

The echo principle is the basis of most ultrasound imaging techniques. After emitting US, the transducer listens for echoes and the received signals are analysed to calculate the distance travelled and the intensity. This gives information about the reflector location and properties. The echoes collected from an area are combined to form an echo pattern and this forms the basis of US images (Martin 2010).

The main components of a typical US transducer consists of; piezoelectric element, matching layer, backing layer, acoustic lens and connection and housing assembly (Gibbs 2011). According to the differences in the geometric structure of the piezoelectric material, transducers are divided into two types: single element transducers and array transducers. Single element transducers are simple transducers with a single piezoelectric element, mostly used for NDT, SONAR and basic US testing applications. In

contrast, array transducers contain an array of piezoelectric elements and can be further divided into linear, curvilinear or sector, and phased array transducers.

Linear array transducers are typically made of 128 - 256 piezoelectric elements in a row and produce parallel scan lines to give a rectangular field of view with the width of the image approximately equal to the length of the transducer head. They operate at frequencies higher than 4 MHz and are mainly used for imaging superficial structures such as thyroid, vascular and musculo-skeletal applications (Gibbs 2011).

Curvilinear array transducers are similar to linear array transducers, but with a curved (convex) transducer face to provide a wider field of view. The operating frequencies are lower, typically around 3.5 MHz or less, and they are mainly used for imaging deep-lying structures such as the kidney, liver, gall bladder and uterus.

Phased array transducers are similar to linear array transducers, with flat transducer faces with piezoelectric elements placed in a row alongside one another. However, the US beam can be electronically steered to any angle, thus producing an image with a wider field of view like curvilinear transducers. Because of the small transducer surface and wider field of view, they are typically used for cardiac imaging where it is hard to image the heart because of the presence of the ribs.

2.3.1 Anatomical Imaging

2.3.1.1 A-mode

A-mode (amplitude mode) imaging is the oldest US imaging technique where a single element transducer produces an US signal, and the echoes from the subject are displayed in an x-y graph with the x-axis representing the time to receive the echoes and the y-axis the amplitude (intensity) of the signal. This imaging technique is rarely used clinically today because of the limited amount of information it provides (Lutz 2011).

2.3.1.2 B-mode

B-mode (brightness mode) is a similar imaging technique to A-mode. It acquires signals from different lines, like in A-mode and converts the echoes into a grey scale based on the amplitude of the signals. The amplitude data acquired from different scan lines are combined to obtain a two dimensional (2D) grey scale image of the object scanned.

Areas of high reflectivity appears as white; low reflectivity as grey and no reflectivity as black in the grey scale image. When the echoes are produced by broad, well-defined boundaries of organs or large vessels, they can be easily identified. However, interference effect from scatterers smaller than the wavelength of the beam results in a granular appearance in the image called ‘speckle’.

2.3.1.3 M-mode

M-mode (motion mode) is used to image moving structures such as heart valves. A B-mode image is initially acquired and the area of interest is marked with a line in the image. Movement of structures intersecting that line is recorded over time and the M-mode will represent how the structures moved towards or away from the scanning probe.

2.4 US ELASTOGRAPHY

US elastography is an US imaging technique, used for analysing the elasticity of soft tissues. Malignant tissues tend to be 'harder' (stiffer) than benign and healthy tissues (Mischi 2014). Several studies has been conducted to assess the reason for this change and a working hypothesis is that the elastic properties of the tissue is associated with collagen density and degree of cross-linking (Paul 2015). Because of this correlation between elasticity values and tissue condition, elastography has become an important tool for cancer diagnosis. The elasticity is generally defined in terms of Young’s modulus, *E*. *E* is the ability of a material to withstand changes in length when a tensile or compressive force is applied i.e. it is the ratio of stress to strain. Further description of *E* can be found in Chapter Three. A pressure is applied to the examined medium and the induced strain distribution is estimated by tracking the tissue motion to produce a strain image, termed the elastogram (Bercoff 2010). Hard tissues will have smaller deformation or strain compared to softer ones. Based on the differences in the methods used for producing the compression, elastography can be divided into two main categories; strain elastography and SWE.

2.4.1 Strain Elastography

Strain elastography, (aka static elastography), measures the strain, σ, produced in the tissue induced by a stress, ϵ, with a mechanical source, usually the US transducer (Figure

4). The operator exerts a uniform compression (force) on the area of examination using the transducer face and the relative deformation of the tissue is calculated using cross-correlation between the radio frequency (RF) signals before and after applying the force, for each scan line. This produces a colour coded elastogram, displaying the spatial distribution of strain, imposed on top of the US B-mode image (Ophir 1991).

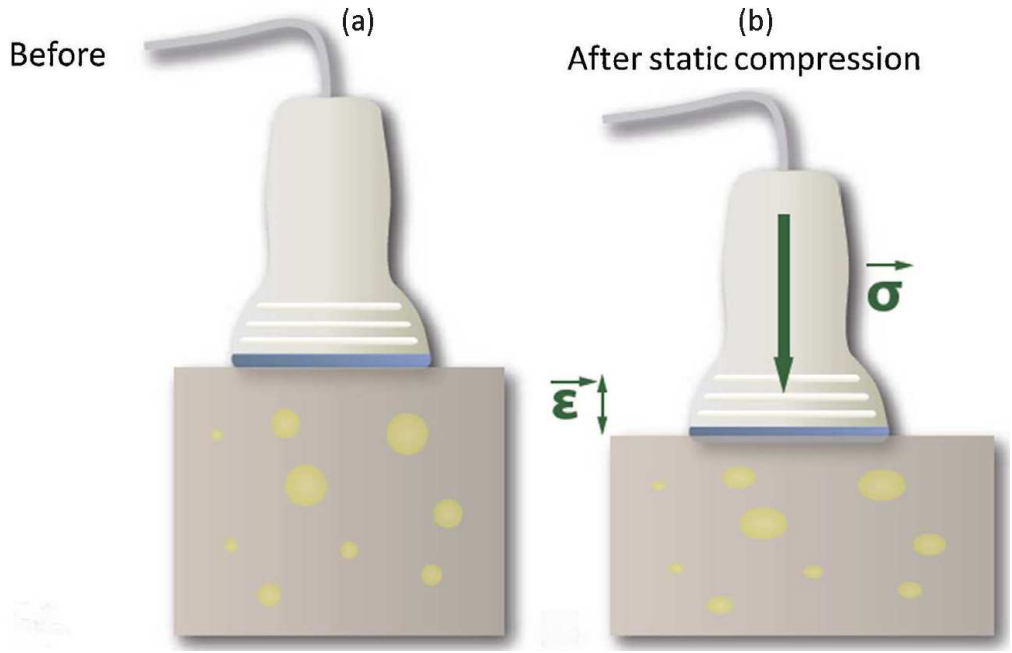

Figure 4: Strain induced because of stress applied by the US transducer (Gennisson 2013).

Strain elastography is the most commonly used elastography technique and has found applications in breast, liver, prostate, thyroid, pancreas, gynaecological malignancies, testicular masses, musculo-skeletal tumours and lymph node imaging (Barr 2014).

Figure 5 shows a static elastography image obtained during an US endoscopy examination of pancreas.

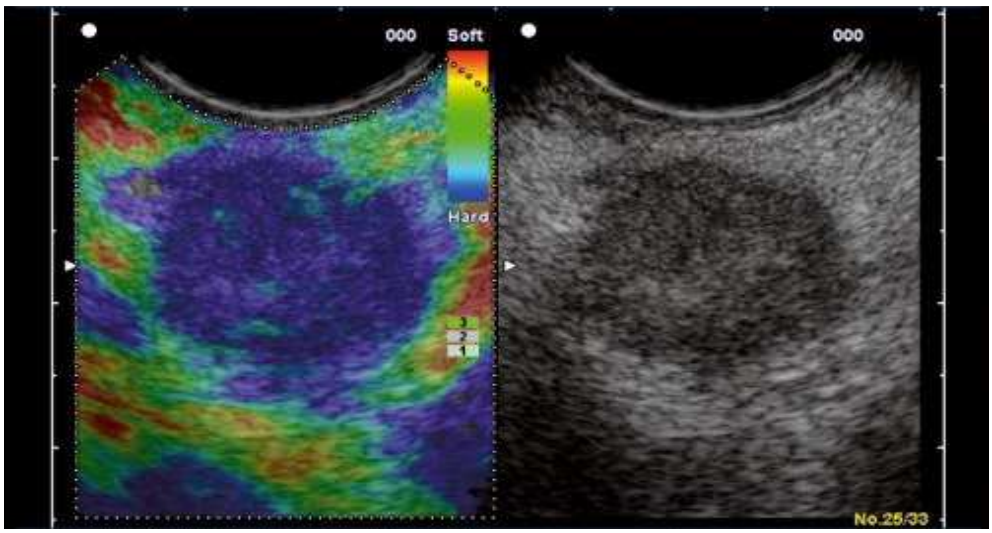

Figure 5: US static elastography image obtained during an US endoscopy examination of pancreas (Hitachi 2015).

While promising results have been demonstrated, many drawbacks have also been reported, including poor reproducibility, inter-operator variability and lack of quantitative information. The resulting elastogram can be analysed qualitatively by comparing the region of interest (ROI) with a reference tissue, usually the adjacent tissue, under the assumption that it is normal or healthy.

2.4.2 Shear Wave Elastography

SWE (aka transient elastography) uses US shear waves to quantitatively assess tissue elasticity, *E*. The beating heart is a natural source of shear waves, but the vibrations are confined only to the near vicinity. Alternatively, by focusing an US wave to a given location, an acoustic radiation force (ARF) can be produced in the medium because of the momentum transfer from the acoustic beam to the medium (Torr 1984). This was first proved in 1998 (Sarvazyan 1998) and the study used ARF, induced by a focused US transducer to trigger the shear wave generation in the tissue. ARF methods were further investigated in several studies for calculation of tissue elasticity maps through post-processing the shear wave speed data (Nightingale 2001, Nightingale 2002, Fahey 2008, Wells and Liang 2011). The shear wave propagating in a lateral direction, induced by ARF, is tracked to calculate the shear wave speed, v_s, as shown in Figure 6.

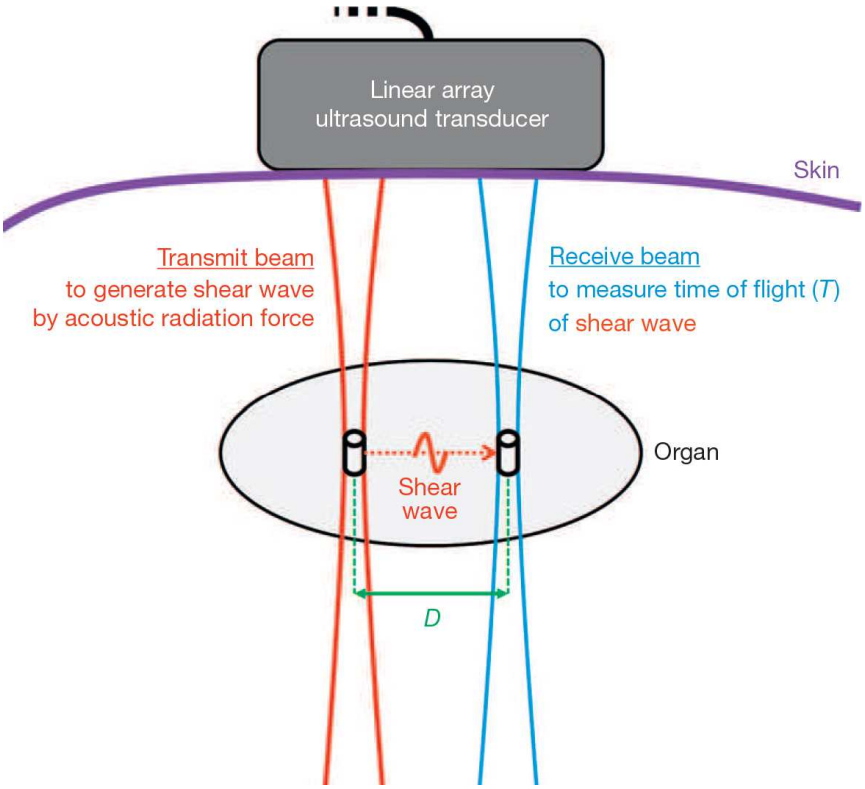

Figure 6: Principle of shear wave generation and detection using US transducer (Mischi 2014).

On knowing v_s, young's modulus, E can be derived using Equation 3.

$$E = 3.\rho.v_s^2 \quad (3)$$

where,

ρ is the density of tissue and is approximately 1000 Kg.m^{-3} (Szabo 2014).

As the mechanical excitation for the shear wave production is applied remotely by the ARF, SWE is operator independent. However, shear waves are very weak and travel at much smaller speeds (1 to 10 m.s^{-1}) compared to the longitudinal waves. They are heavily attenuated and hence they die out within a few millimetres (mm) of propagation. A solution would be to generate higher US powers at the focus, thus generating a stronger shear wave. However, this could lead to overheating of the transducer and there are many concerns over usage of higher acoustic powers (Bercoff 2008).

2.4.2.1 Supersonic SWE

(a) Supersonic Shear Wave Generation

A new technique called supersonic SWE was reported in 2004, providing quantitative *E* mapping of the tissue in less than 30 milliseconds (ms) (Bercoff 2004). A novel technology was introduced, termed as 'SonicTouch^{TM}', to produce shear wave sources moving at supersonic speed within the tissue (Bercoff 2008, Bercoff 2010, Fink and Tanter 2010, Bercoff 2011). The technique allows focusing of successive US beams at different depths, thus creating a shear wave source moving faster than the shear wave it produces (Figure 7b). This results in constructive interference of the shear waves into a 'Mach cone' shape (Figure 7c), thereby increasing the shear wave generation efficiency by a factor of 4 - 8 compared to a non-supersonic source (Figure 7a).

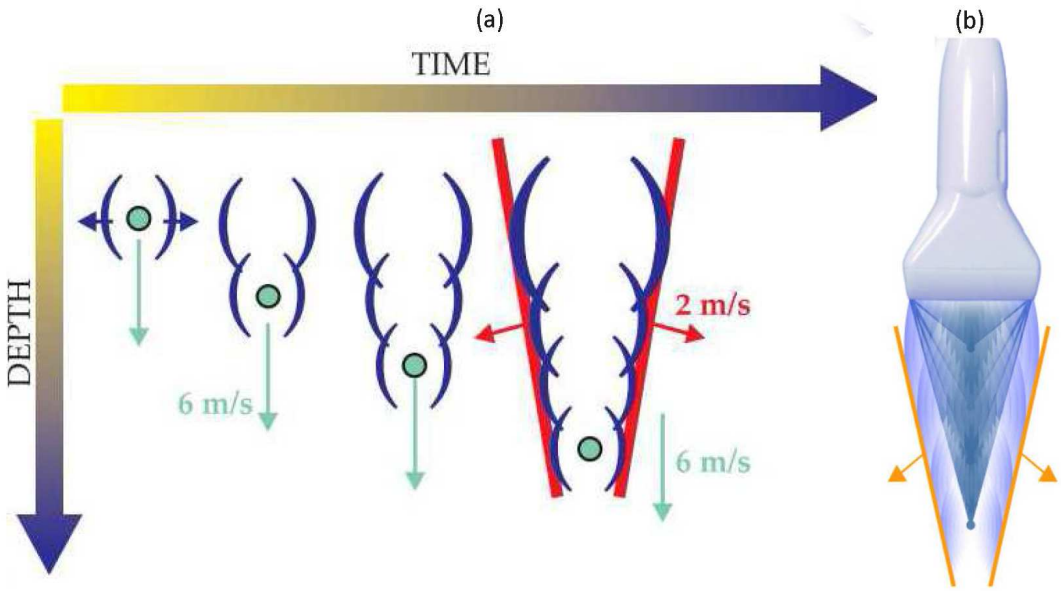

Figure 7: (a) ARF induced by SonicTouch^{TM} where the source is moved along the beam axis, creating two-plane and strong shear waves (Fink and Tanter 2010), resulting in the (b) 'Mach' cone shape of intense shear waves in two planes (Bercoff 2008).

Another term used to define this shear wave propagation is the Mach number, the ratio of the speed of the shear wave to the speed of the moving source. Because of the large difference between the speed of ultrasonic waves creating the ARF, around 1500 m.s^{-1}, and the speed of generated shear waves, of the order of 1 m.s^{-1}, extremely high Mach numbers can be produced in the medium, up to 1500. Studies show that these shear wave sources can be generated anywhere in the medium, at any time by focusing

appropriate US beams (Bercoff 2004). Supersonic SWE uses ultrafast imaging methods to image the shear waves while they are travelling through the medium.

(b) Ultrafast Imaging

Shear waves propagate through a 3 - 6 cm wide imaging plane in about 10 - 20 ms. A frame rate of at least 1 KHz are required to ensure the capture of shear waves with adequate detail. As conventional US imaging systems have frame rates of 50 - 60 Hz, they are unsuitable for the purpose. The first US system which is capable of imaging at such fast frame rates was developed by Supersonic Imagine (Aix-en-Provence, France). The image acquisition is performed in three steps as shown in Figure 8.

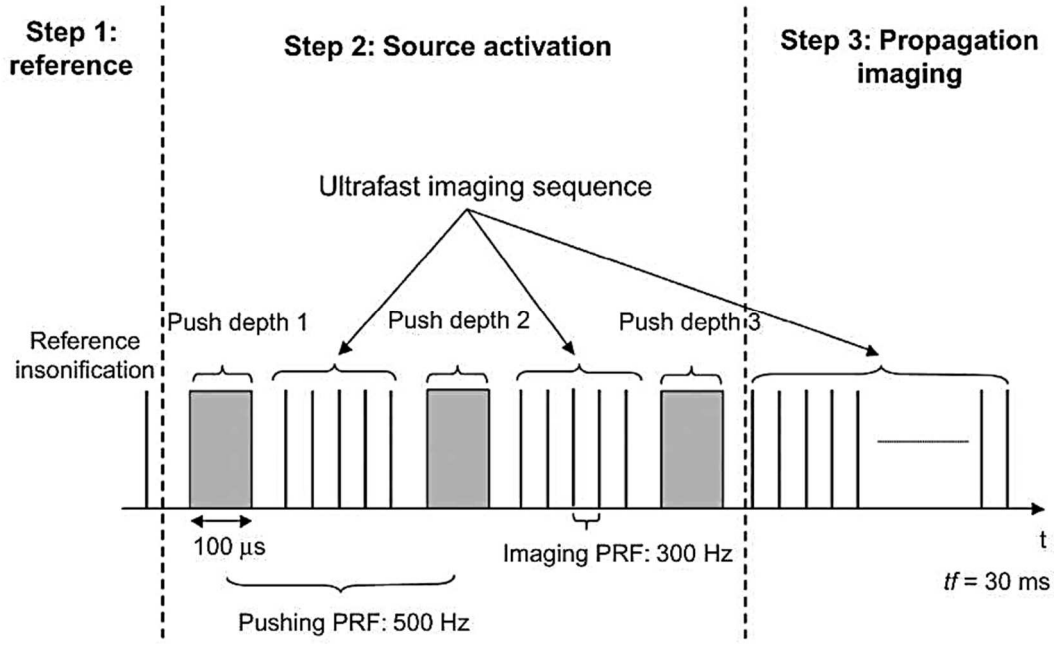

Figure 8: Emission sequence for a supersonic SWE system (Szabo 2014).

Reference imaging: An US image of the whole imaging plane is captured, and will be used as a reference image at later stage to analyse the displacement caused because of the shear wave propagation.

Source activation (aka pushing mode): The supersonic source is then triggered by continuously focusing the US beam at different depths. Each push in the 'pushing' beam is approximately 100 µs long (Figure 8). US images are captured at high frame rates in between the successive pushes (Figure 9) to monitor the supersonic source activation.

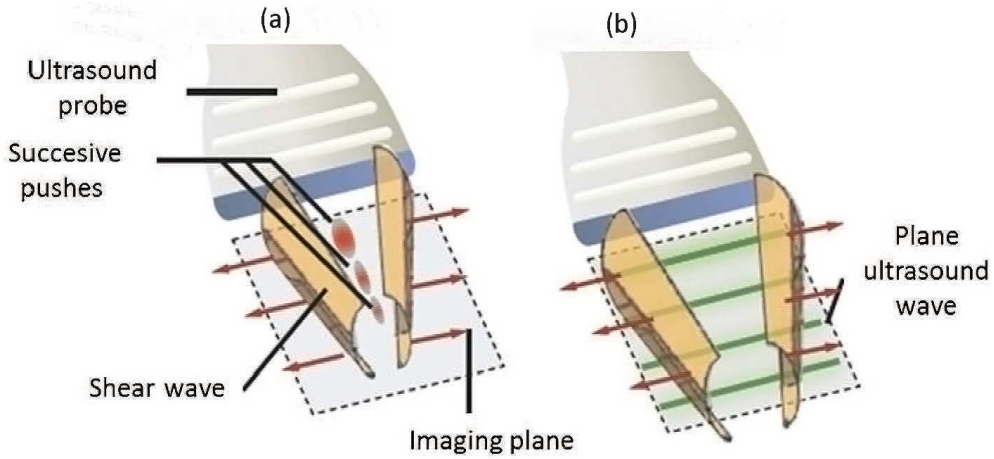

Figure 9: Schematic representation of the supersonic Mach cone with (a) successive pushes and (b) ultrafast imaging (Gennisson 2013).

The time-of-flight of the US wave from the imaging transducer to and from the ROI determines the maximum achievable frame rate. For example, a maximum frame rate of 20,000 Hz is achievable for a typical 4 cm deep breast image. A Supersonic Imagine SWE scanner is capable of switching between the source activation and imaging modes, thus, allowing real-time triggering of the supersonic source and capture of the resulting shear waves (Bercoff 2004).

Propagation Imaging: Ultrafast imaging (Figure 9a) is continued after the propagation of shear waves through the medium for a small period. The total sequence, from the reference image acquisition to the propagation imaging lasts only up to few tens of ms.

(c) Real-time Display of Elasticity

The tissue displacements induced by the propagation of shear waves are recorded and quantified using Doppler imaging methods to produce video of the particle velocities. Representation of shear wave propagation is thus obtained and v_s is estimated at each pixel using cross-correlation algorithms. Figure 10a shows images of four frames from an ultrasound video, representing displacements in a TMM phantom with a 10 mm diameter stiff inclusion. The grey scale shows displacements from -10 to + 10 µm. The conventional US B-mode image in Figure 10b, obtained by sampling the video in Figure 10a, barely shows the inclusion.

Figure 10c is the quantitative, colour coded map of *E* produced by supersonic SWE. A strain elastography image of the same inclusion acquired using a commercial US scanner

is shown in Figure 10d.As seen from Figure 10a, *E* is displayed in kilopascal (kPa) using a colour coded image superimposed on a B-mode image with stiffer tissues in red and softer tissues in blue. Figure 11 shows the US and elastography images of breast tissue indicating the presence of ductal carcinoma obtained using a supersonic SWE scanner.

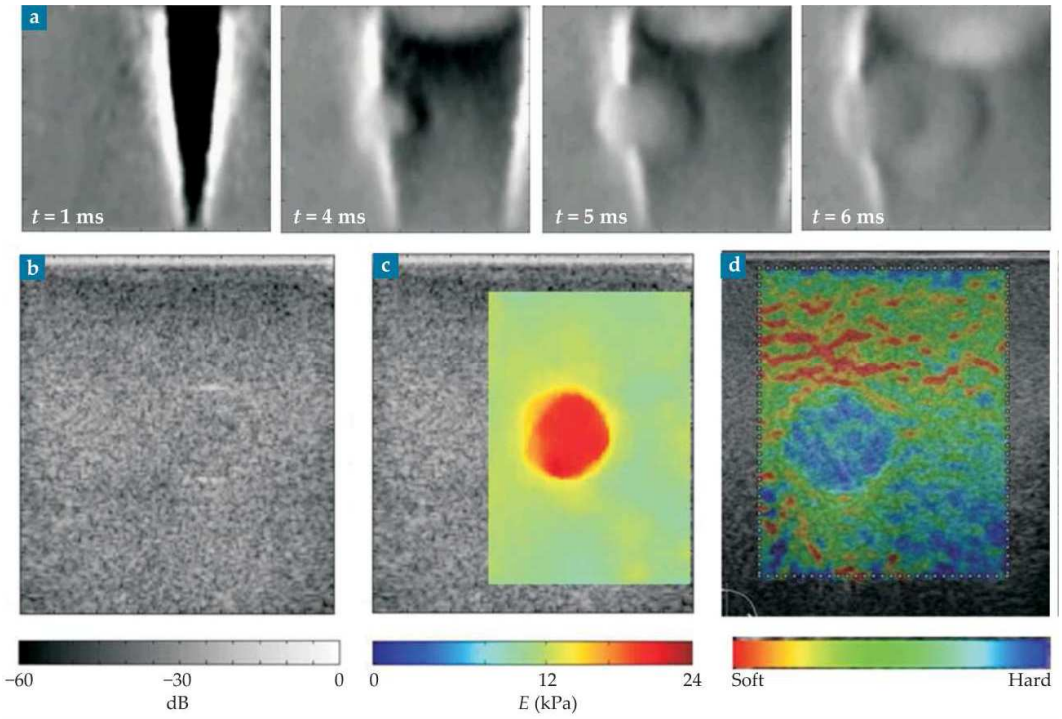

Figure 10: (a) US image frames showing the tissue displacement induced because of the shear wave push. The Supersonic SWE quantitative elastogram (c) is compared with (b) US B-mode and (d) strain elastography images (Szabo 2014).

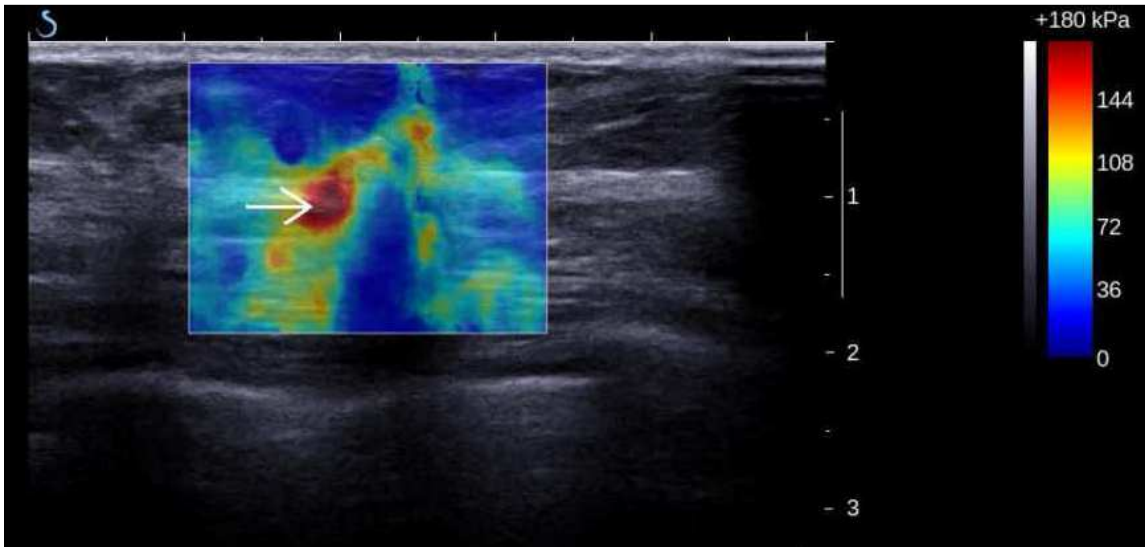

Figure 11: US and elastography images of breast invasive ductal cancer at 1 mm spatial resolution showing increased peritumoural stiffness (arrow). Adapted from (Evans 2010).

2.4.2.2 Applications of Supersonic SWE

The clinical potential of shear wave imaging, has been investigated for many potential applications such as breast cancer diagnosis (Evans 2010, Wendie 2012), liver fibrosis staging (Bavu 2009, Muller 2009, Bavu 2011), cardiovascular applications (Couade 2010, Lee 2012), prostate applications (Richard 2012, Ahmad 2013), abdominal imaging (Arda 2011), musculo-skeletal imaging (Gennisson 2012, Itoigawa 2015) and thyroid and neck imaging applications (Bhatia 2012, Magri 2012). The supersonic SWE technique has also been used for evaluating *in-vivo* and *ex-vivo* animal models to assess their suitability for specific applications (Ramnarine 2014, Jiang 2015). Supersonic SWE has also been used to characterise the tissue stiffnesses in TEC, as discussed in Chapter Four (Joy 2015).

2.5 THERAPEUTIC US

Some of the most common therapeutic applications of US are in extracorporeal lithotripsy (Pengfei 2011), ophthalmology (Packer 2005), dentistry (Ustun 2008, Ang 2010) and in HIFU. High intensity US waves can be focused to specific volumes in tissues. In the focus, the temperatures increases rapidly up to 60 °C or higher in a few seconds, thereby destroying the cells without harming the tissues nearby. This non-invasive method of destroying tissues in the US focus is variously known as HIFU therapy, FUS, US ablation (Habash 2006) and pyrotherapy (Kennedy 2003).

A diagram demonstrating the principle of HIFU is shown in Figure 12a and Figure 12b shows a 2 cm lesion produced in chicken breast tissue using a 1.09 MHz transducer sonicating at 40 W power for a duration of three minutes (min). The experiment was conducted in the laboratory and the tissue was at room temperature before sonications. The output power was measured from the calibrated power amplifier output panel.

The main difference in using US as a therapeutic modality as opposed to an imaging modality is that the former tends to use larger acoustic intensities than the latter (Coussios and Roy 2008), as well as lower frequencies. The increase in intensity is accomplished through combining greater peak intensities and longer pulse durations or using continuous waves. Using focused transducers, usually between 0.25-5 MHz, a sharp and accurate focus at varying distances up to many cm from the transducer can be created within the human body.

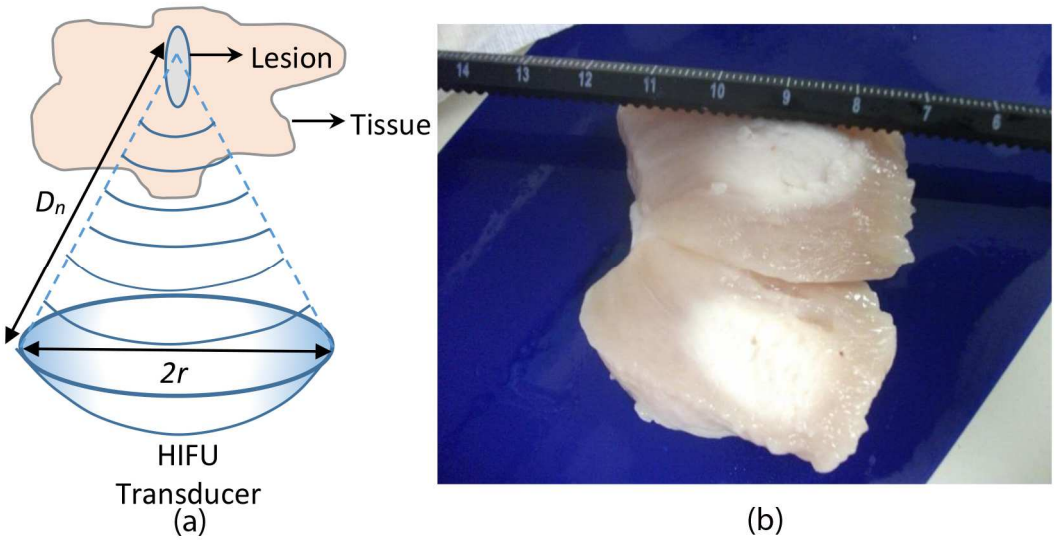

Figure 12: (a) Diagram showing the principle of HIFU and (b) 2 cm lesion produced in chicken breast tissue using a 1.09 MHz focused US transducer (Power – 40 W, Sonication time – 3 min).

The intensity of the ultrasound increases towards the focus, reaching its maximum at the focus. The focal intensity can be represented as

$$I = I_0 . \left(\frac{2 . \pi . r^2}{\lambda . D_n} \right) \quad (4)$$

where,

I_0 represents the average intensity at the transducer surface.

r is the flat radius of the transducer.

D_n is the focal distance.

λ is the wavelength (Duck 1998).

The versatility of US for a wide range of usage in medical therapies lies in the variety of its interactions with cells and tissues (Mitragotri 2005). When US at intensities above diagnostic ranges insonates tissue, it can trigger various thermal and mechanical effects (Wood and Loomis 1927). The immediate effect of US is the elevation in the temperature because of the conversion of energy into heat, causing coagulative necrosis in most tissues. As seen in Figure 12, focusing results in high intensities only in the focal region thereby reducing the potential for thermal damage to regions outside the focal zone where the intensity is much lower. In addition to the thermal effects of HIFU, the mechanical effects occurring at high intensities are cavitation and microstreaming (Zhou

2011). Both thermal and mechanical effects contribute towards cell necrosis (Nyborg and Wu 2006).

The first use of HIFU for therapeutic applications can be traced back to 1942 when Lynn et al demonstrated the production of US lesions in bovine liver without damaging the surrounding tissues. Then, in 1944, they illustrated the use of HIFU to treat neurological disorders by carrying out *in-vivo* studies on 37 animals (Lynn 1942, Lynn and Putnam 1944). However, most early research in HIFU was carried out by the Fry brothers at the University of Illinois, USA, in the 1950s. They illustrated that the lesions produced by focusing an US beam are well confined, thus preventing destruction of the neighbouring tissues (Fry 1954, Fry 1955, Fry 1958).

HIFU surgery has shown fast development in the past 20 years, especially in cancer treatments, including: prostate cancer (Rewcastle 2006), breast cancer (Huber 2001), pancreatic cancer (Feng 2005), liver and kidney tumours (Illing 2005) and in bone metastases (Liberman 2006). HIFU has also been used to treat uterine fibroids (Zowall 2008). The capability of HIFU transducers to focus the US energy to very small diameters, in the ranges of a few mms, has made this technology in demand in the field of FUS. Nowadays, several imaging modalities such as MRI, US and CT are used with HIFU procedures for visualising the targeted tissue to monitor the treatment, the most common being MRI and US.

2.5.1 Magnetic Resonance Guided Focused Ultrasound Surgery

2.5.1.1 MRI

MRI uses magnetic fields and RF pulses rather than the ionising radiations used in x-ray and CT. The human body contains approximately 70% water, which is composed of hydrogen and oxygen atoms. MRI relies on the magnetic property of hydrogen atoms to produce images. The hydrogen nucleus is composed of a single proton with no neutrons and the constant spinning motion of the protons in the nuclei produces a magnetic field, termed the magnetic moment. Normally these protons are oriented randomly and there is no net magnetic field. The components of an MRI machine include the primary magnets, gradient magnets, RF coils and the computer system.

Under the influence of an external magnetic field, B_0, produced by the primary magnets, the protons rotate around the axis of the applied magnetic field with a frequency ω_0, usually termed the precessional or Larmor frequency.

The magnetic field of an MRI system is measured in Tesla (T). The value of ω_0 is a constant dependent on the magnitude of B_0 and is defined by the Larmor Equation (Equation 5)(Epstein 2008).

$$\omega_0 = \gamma . B_0 \quad (5)$$

where,

γ is the gyromagnetic ratio and B_0 is the strength of the magnetic field.

The gradient coils generate secondary magnetic fields over the primary field and they are arranged in opposition to each other to produce positive and negative pulses. The arrangement of these gradient coils gives MRI the capability to image directionally along the x, y and z axes. There are three gradient coils named according to the axis along which they act and they are used to alter the local strength of the primary magnetic field, thereby changing the precession frequencies between slices. This can then be used for slice selection and localisation in the x, y and z axis, called spatial encoding of MR images. The z gradients runs along the long axis to produce axial images, y along the vertical axis to produce coronal images and x along the horizontal axis to produce sagittal images (Hornak 2008).

RF coils are used to emit RF pulses or secondary magnetic pulses at the precessional frequency and this results in some of the hydrogen protons being 'knocked' 180° out of alignment with the static magnetic field and being forced into phase with other hydrogen protons. Cessation of the RF pulses causes the hydrogen protons to return to their relaxed state or initial alignment, releasing energy as emitted pulses. RF coils receive the emitted pulses and, depending upon the constituents of different tissues, the released energy differs and this forms the basis of tissue differentiation in the MRI. The actual process of receiving the MR signal can be broken down into T1 relaxation and T2 decay; this is out of scope for this thesis and is not explained further.

MRgFUS is considered to be an effective combination of non-invasive surgery and precise real-time treatment monitoring. MRgFUS uses MRI to localise target tissue prior

to applying FUS, to monitor temperature in real-time through MR thermometry during the surgery, and to verify the results of the surgery after the treatment. MRI is used to visualise and quantify the thermal energy that is deposited in treated and surrounding tissues. Some of the important advantages of using MRI instead of US as an imaging modality during FUS relate to its ability to perform real-time thermometry and high resolution imaging (Nyborg and Wu 2006).

MRI is also superior to US in planning and monitoring the treatment and locating the focal point as US imaging lacks accuracy in detecting the margins of tumours and increases the uncertainties in detecting important structures such as nerves and bones in the treatment area. The Exablate 2000 (Insightec Ltd, Haifa, Israel) was the first commercial MRgFUS therapy delivery system and the first to be approved by the Food and Drug Administration (FDA) (Jolesz 2009). Figure 13 shows the Exablate MRgFUS system used in a configuration to treat uterine fibroids.

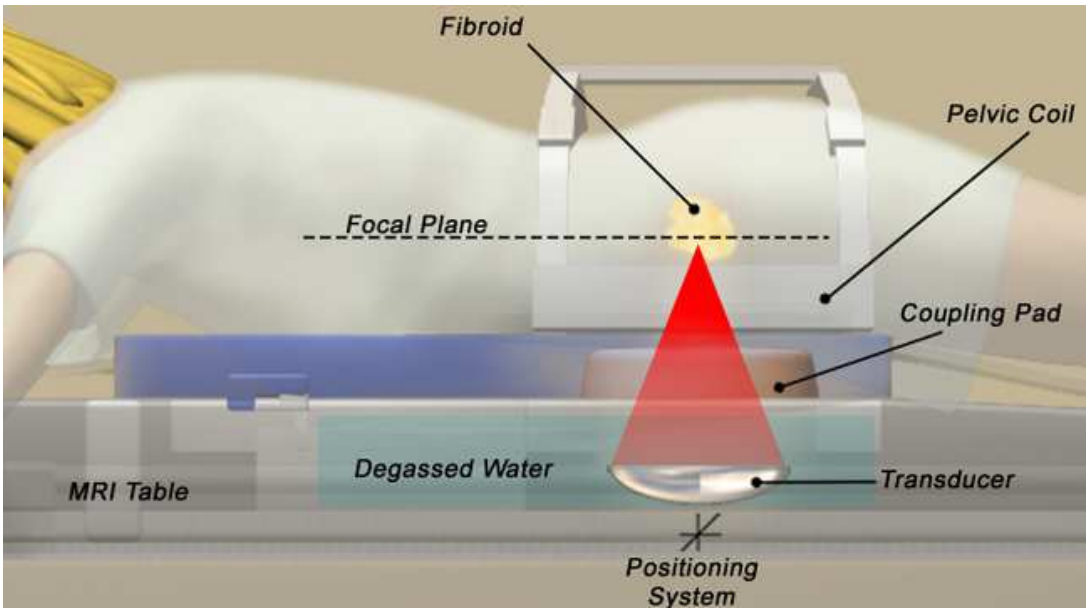

Figure 13: Exablate MRgFUS system configured to treat uterine fibroids (Bromilow 2012).

2.5.1.2 MRI Thermometry

As discussed previously, for image guidance during HIFU surgery, the capability of real-time thermometry makes MRI stand out from other imaging modalities. MR parameters such as the T1 (spin-lattice) relaxation time and the water proton resonance frequency (PRF) are temperature sensitive. Overviews of different MR thermometry methods monitoring changes in these parameters can be found in the literature (Wlodarczyk

1999, Bruno 2000). Out of these MR thermometry methods, PRF thermometry is preferred because of the linearity of frequency shift and higher sensitivity (Rieke and Butts Pauly 2008) and will be discussed further in Chapter Six.

2.6 INTERVENTIONAL US

Interventional ultrasound, i.e., US-guided interventions, refers to diagnostic or therapeutic minimally invasive procedures guided by real-time US imaging (Holm and Skjoldbye 1996, Buscarini 2011). One of the major applications of interventional US is for guiding needles during regional anaesthesia, thereby minimising nerve damage and further complications..

2.6.1 Ultrasound Guided Regional Anaesthesia

By allowing real-time imaging of nerves with direct needle guidance, UGRA offers a novel approach to locating and identifying nerves. A nerve block is considered to be successful when the tip of the needle is positioned as close as possible to the nerve without touching it and the local anaesthetic fluid will be observed real-time in the US image spreading around the nerve. US guidance offers the opportunity to enhance success, reduce complications, and improve training experience of regional anaesthesia (Carty and Nicholls 2007).

In UGRA, the term 'axis' is used to describe the nerve position relative to the US beam. A long axis or longitudinal view (Figure 14a) is an image of the nerve along its length and a short axis or transverse view (Figure 14c) is the image across the diameter of the nerve. Similar to the term 'axis', in describing the nerve position, the term 'plane' denotes the needle position relative to the US beam. The in-plane (IP) approach (Figure 14b) allows visualising the entire needle (shaft and the tip) whereas, in the out-of-plane (OP) approach (Figure 14d), only the needle tip can be visualised and will be seen as an echogenic dot in the image (Andrew 2006).

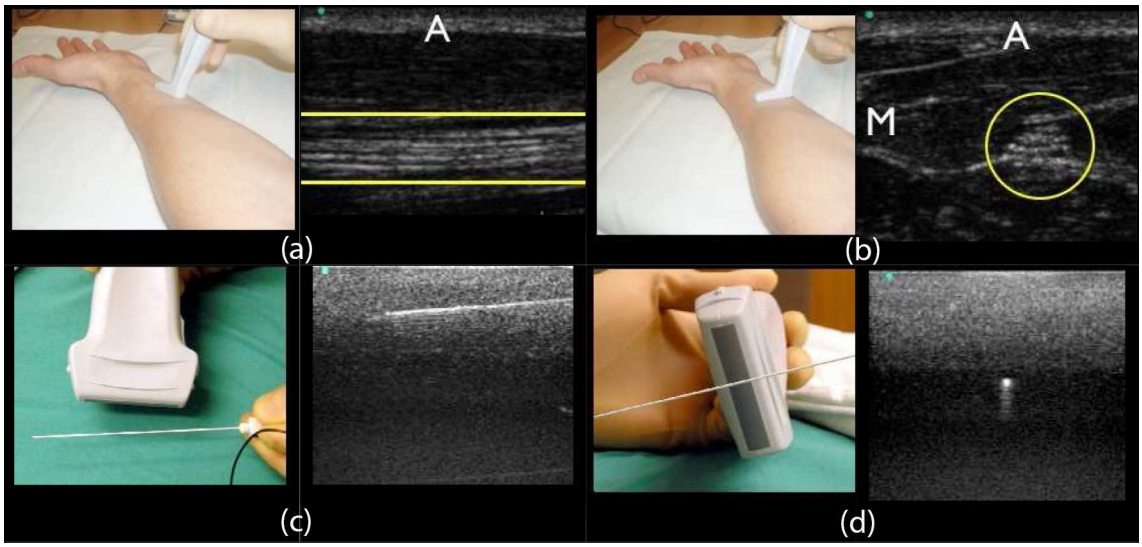

Figure 14: (a) Long axis and (b) short axis images of the median nerve. (c) IP and (d) OP approaches to inserting the needle and the corresponding US images of the needles: adapted from (Dartmouth-Hitchcock 2015).

IP and OP approaches have advantages and disadvantages. The IP approach provides the most direct visualisation of the needle tip but a disadvantage is the long needle path, which results in more tissue for the needle to cross. The OP approach is most similar to traditional approaches to regional block guided by nerve stimulation or palpation and uses a shorter needle path compared to the IP approaches. A disadvantage of the OP approach is the extent of the blind needle path i.e. the potential for anatomical structures that may lie beyond the scan plane. The IP approach is the most commonly used for UGRA because of the greater confidence and safety it offers (Grant and Auyong 2012).

2.6.2 Needle Visibility in UGRA

The safety, efficacy and level of confidence in using UGRA is directly influenced by the good visibility of needles during the procedure. Several issues related to poor visibility of needles during regional anaesthesia have already been documented (Schafhalter-Zoppoth 2004, Chin 2008). Factors such as the needle insertion angle and needle type directly affect the needle visibility. A steeper insertion angle results in greater reflection of the US waves incident on the needle away from the imaging array resulting in a poorer image and reduced needle visibility (Hocking and Mitchell 2012). Echogenic needles

(Figure 15) have been identified to be much more visible compared to non-echogenic ones because of their enhanced scattering compared to the former.

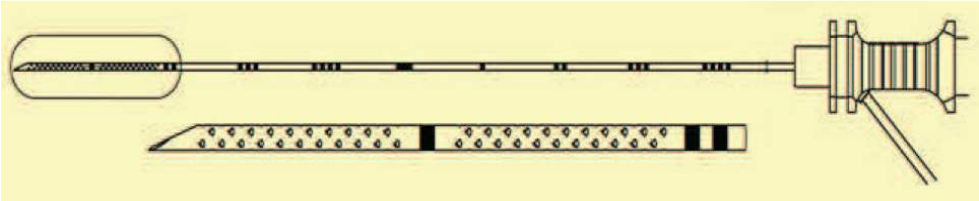

Figure 15: Schematic showing an echogenic needle tip, highlighting reflectors 2 cm from the needle tip to increase US reflection at steeper angles of needle insertion: adapted from (Raju and Grant 2013).

When compared to standard anaesthetic block needles, echogenic needles have increased shaft and tip visibility, irrespective of the anaesthesiologist's experience level, and can also improve suboptimal scanning technique, allow steeper insertion angles, reduce technical complications and thereby increase the confidence of anaesthesiologists (Guo 2012, Hocking and Mitchell 2012, Nakagawa 2015). A case study analysing the effect of needle insertion angles on the needle visibility, conducted in TEC is discussed in Chapter Five.

2.7 SUMMARY

This Chapter provided necessary background for the work presented in this thesis. The broad introduction to medical US included reviews of widely used medical US imaging, therapeutic US and interventional US systems. As a general introduction to US, the history, generation and propagation of US were discussed. B-mode US imaging and other specific US elastography imaging were presented, with a detailed review of SWE. The basic principles for using US for therapy included a review of HIFU principles followed by a general introduction to MRI, as the best means of guidance for HIFU. The review concluded by introducing UGRA as an interventional use of US imaging. This Chapter discussed literature to provide basic understanding to introduce the reader to the terminologies used in the rest of the thesis. Detailed descriptions of any techniques necessary for understanding specific work are included in the background sections in corresponding further Chapters.

CHAPTER 3

Tissue Mimicking Materials

3.1 INTRODUCTION

US phantoms include a wide range of objects such as test objects with inclusions/targets to mimic human organs/vessels, *in-vivo*/*ex-vivo* animal models, FFC and embalmed human cadavers. While the main use of such phantoms is for QA tests, *in-vivo* and *ex-vivo* models are more often used for research and in developing new treatment approaches and systems. The focus of this Chapter is TMMs and also presented are means of acoustic and mechanical characterisation of TMMs prepared in the laboratory.

3.2 ULTRASOUND TEST OBJECTS AND TISSUE MIMICKING MATERIALS

US test objects, or phantoms, are designed to allow measurements of parameters relating to the imaging performance of the system - transducer combination. They are composed of TMM, with most having simple homogenous structures. Phantoms that mimic heterogeneous organs have targets embedded within them and are generally termed anthropomorphic phantoms. These are available commercially and price can range from hundreds to thousands of pounds. They are preferred for training and QA testing of ultrasound systems and in clinical research and training. A range of ultrasound test objects is commercially available with several major manufacturers such as blue phantom (BluePhantom^{TM} 2015), CIRS Inc (CIRS-Inc), ATS Laboratories (ATS 1978), Gammex RMI (Gammex-RMI 1987) and Diagnostic Sonar Ltd (Diagnostic-Sonar-Ltd 2015).

3.2.1 Tissue Mimicking Materials

Commercial US phantoms are expensive and cannot be modified in size or acoustic and mechanical properties to suit specific applications. Custom made TMM can be made in any shape or size with desired material properties. To understand further and to create a baseline, it is necessary to evaluate these tissue mimics and the work discussed in this Chapter discusses the preparation and characterisation the most commonly used TMMs. To match with the variation in acoustic and mechanical properties of different human tissues (Table 2), a range of TMM with different properties are also used.

Table 1: Acoustic properties of human tissues (Zell 2007, Culjat 2010).

Material	Velocity (m/s)	Attenuation (dB/cm.MHz)	Density	Acoustic Impedance (MRayl)
Air	330	-	1.2	0.0004
Blood	1584	0.2	1060	1.68
Bone, Cortical	3476	6.9	1975	7.38
Bone, Trabecular	1886	9.94	1055	1.45
Brain	1560	0.6	1040	1.62
Breast	1510	0.75	1020	1.54
Cardiac	1576	0.52	1060	1.67
Connective Tissue	1613	1.57	1120	1.81
Cornea	1586	-	1076	1.71
Dentin	3800	80	2900	8
Enamel	5700	120	2100	16.5
Fat	1478	0.48	950	1.4
Liver	1595	0.5	1060	1.69
Marrow	1435	0.5	-	-
Muscle	1547	1.09	1050	1.62
Tendon	1670	4.7	1100	1.84
Soft Tissue(Average)	1561	0.54	1043	1.63
Water	1480	$0.0022*f^2$ (dB/cm)	1000	1.48

The most significant part of any US phantom is the TMM and for any TMM to approach the equivalence with human tissue, it should have similar acoustic properties to the tissue it mimics across a range of diagnostic frequencies. The comparison is usually made in terms of acoustic velocity, attenuation coefficient, and acoustic impedance. The International Electro-technical Commission (IEC) (IEC 1996) and American Institute of Ultrasound in Medicine (AIUM) (AIUM 1990) have developed standards for TMM acoustic properties. These recommend an acoustic velocity of 1540 ms^{-1}, and attenuation coefficients of 0.5 – 0.7 dB cm^{-1} MHz^{-1} for a frequency range of 2 - 15 MHz with a linear attenuation to frequency response (Browne 2003).

TMM can be broadly classified in two different groups, soft and hard. Soft TMMs are models used to represent soft tissues such as muscles, tendons, ligaments, nerves and blood vessels and the majority of these use isotropic, homogenous materials. Hard TMMs are used for hard tissues such as enamel, the rib cage and other bones and are mostly made of polymer composites. Acoustic properties and characteristics of hard TMM are outwith the scope of this thesis and not discussed further. Soft TMM has many sub-groups according to the base material used for its preparation, including agarose-

based, polyacrylamide gel-based (Zell 2007), evaporated milk-based, and many others as shown in Table 2.

Table 2: Different types of soft TMM and their acoustic properties (adapted from Culjat (2010)) (- Commercially available).*

Material	Velocity (m/s)	Attenuation (dB/cm.MHz)	Density	Acoustic Impedance (MRayl)
Agarose-based	1498-1600	0.04-1.4	1016-1100	1.52-1.76
Gelatine-based	1520-1650	0.12-1.5	1050	1.60-1.73
Magnesium silicate-based	1458-1520	0.85	-	-
Oil gel-based	1480-1580	0.4-1.8	1040-1060	1.54-1.67
Open cell foam-based	1540	0.46	-	-
Polyacrylamide gel-based	1540	0.7 dB/cm @ 5MHz	1103	1.7
Polyurethane	1468	0.13	1130	1.66
Polyvinyl alcohol-based	1520-1610	0.07-0.35	-	1.60-1.77
Tofu	1520	0.75	1059	1.61
Water-based	1518-1574	-	1000	1.48-1.60
Condensed milk-based*	1540	0.5	-	-
Urethane rubber*	1460	0.5-0.7	900	1.31
Zerdine *	1540	0.5-0.7	-	-

A range of different soft TMM samples were prepared in the laboratory, primarily for ultrasound B-mode imaging, and tested for acoustical and mechanical properties. Table 3 shows the list of TMMs prepared and tested. The recipes used for preparing these materials are a compilation of existing protocols and the detailed steps and references are given in the Appendix I.

3.3 ACOUSTIC CHARACTERISATION

Acoustic characterisation of TMM is essential to ensure that the properties are within the defined standard range. Testing involved measuring the acoustic velocity, attenuation coefficient, acoustic impedance and density. Acoustic properties of the sample can be calculated in two different ways, the pulse-echo method and the through-transmission method.

Table 3: TMMs made in the laboratory and sources for their recipes.

TMM	TMM- IMAGE	Source
Evaporated Milk based Liquid TMM	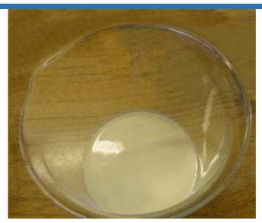	Madsen (1998)
Evaporated Milk Solid TMM (Agarose-based)		Madsen (1998)
EPP Grey TMM (Agarose-based)		Ramanarine (2001); Inglis (2006)
Polyacrylamide gel based TMM		Zell (2007)
Polyacrylamide gel based HIFU TMM	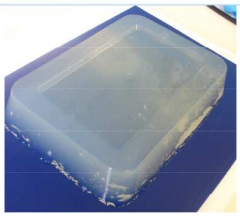	Teirlinck (1998);(Gabriela 2007);(Prokop 2003)
Agar TMM (Agarose-based)	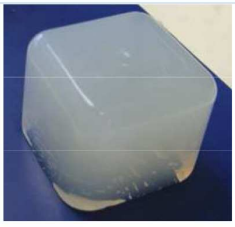	Zell (2007)

3.3.1 Pulse-echo Technique

The pulse-echo technique analyses the reflected sound waves from the sample to measure its acoustic properties. The technique is similar to echolocation used in

submarines and by bats, whales and dolphins for navigation. It is also widely used in SONAR by surface vessels and for NDT. The testing can be done either by the contact or immersion method. Samples are usually placed on strong reflectors such as a steel or glass plate to enhance the echoes from the base of the sample.

Usually a single transducer is used as the transmitter (Tx) and receiver (Rx) and the received signal is analysed to measure the acoustic properties of the sample. Good coupling between the transducer and the sample is essential to prevent signal loss. For the immersion method of pulse-echo testing, the sample is immersed in degassed water (Figure 16a) and for the contact method, an acoustic coupling layer (e.g. gel) is placed between the transducer and the sample (Figure 16b). Figure 16c shows the characterisation of EPP grey phantom using the pulse-echo contact method.

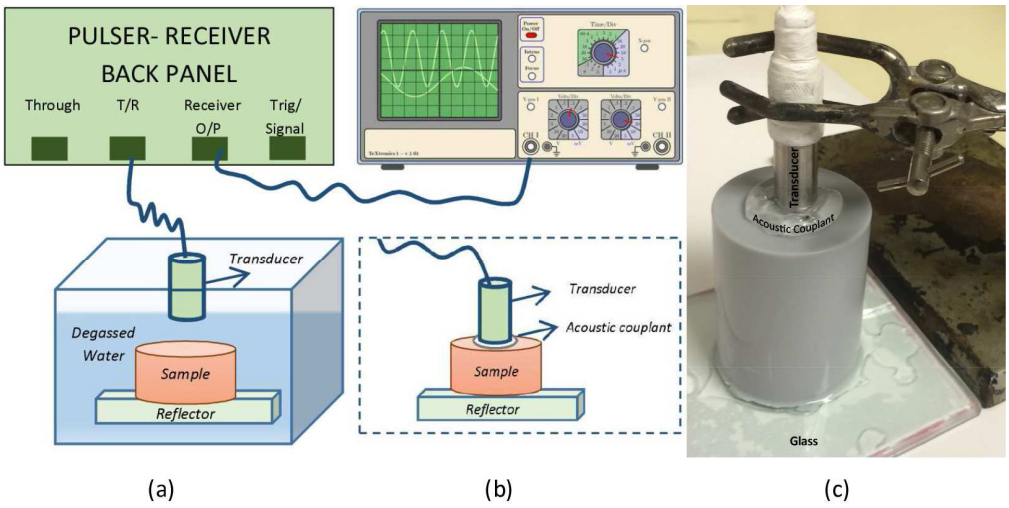

Figure 16: Acoustic characterisation using (a) immersion and (b, c) contact pulse-echo testing.

3.3.2 Through-transmission Testing

Through-transmission testing uses one transducer as the Tx and a second one as a Rx. Like pulse-echo testing, through-transmission testing can also be done either through the contact or immersion method. Figure 17a shows the schematic of transmission through immersion testing and Figure 17b shows the under-water image of evaporated milk solid TMM during the test.

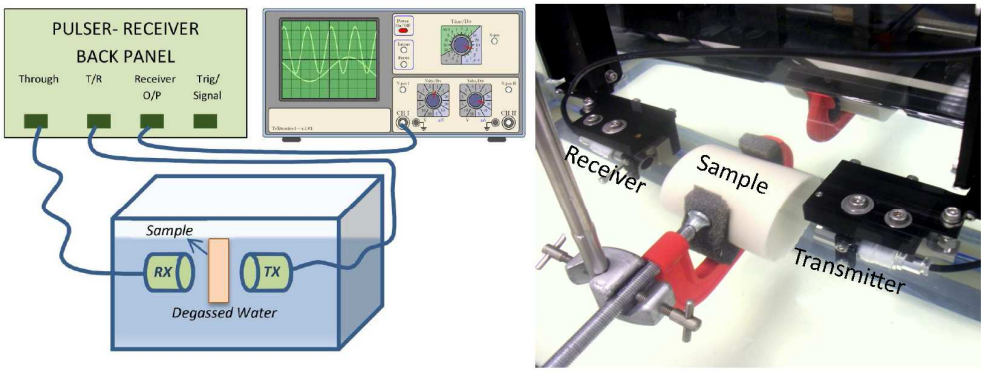

(a) (b)

Figure 17: Acoustic characterisation using through-transmission testing, (a) schematic and (b) experiment.

3.3.3 Materials and Methods

3.3.3.1 Speed of Sound

Speed of sound, c_s of any material is typically determined by time-of-flight measurements through a sample of known thickness. The measurements are calculated relative to the speed of sound in water at room temperature (1480m.s^{-1}) (Duck 1990).

Speed of Sound Calculations Using Pulse-echo Method

During the pulse-echo method of testing samples, the echoes from the top of the steel reflector are recorded in the degassed water medium without the sample. An example schematic of the echoes is shown in Figure 18. The distance from the top of the steel reflector to the transducer is calculated by

$$c_w = \frac{2D}{\Delta T_1} \tag{6}$$

where

c_w is the speed of sound in water (1480 m/s) at room temperature.

D is the distance from the top of the steel reflector to the transducer.

ΔT_1 is the round trip time of the pulse (time between the first and second echo signals).

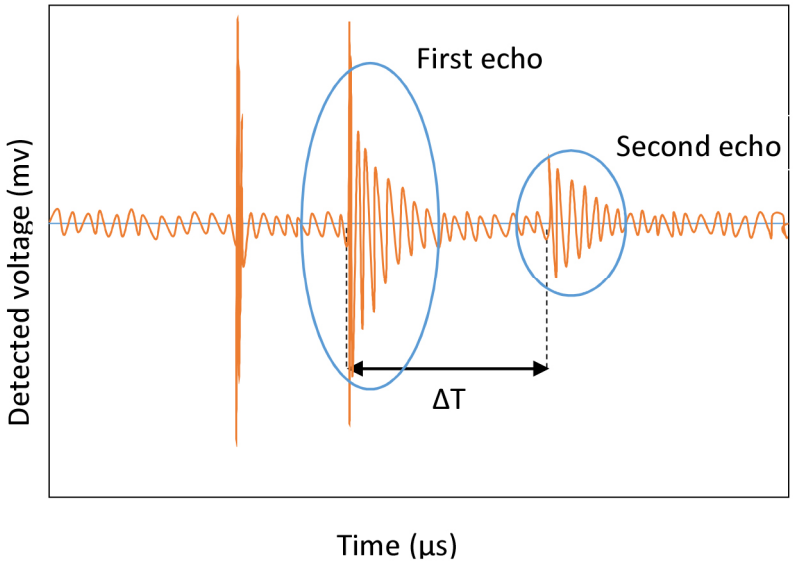

Figure 18: Representation of echo patterns during pulse-echo testing.

The sample to be tested is then placed on top of the steel reflector and the measurements are repeated. The speed of sound in the TMM, c_s can then be calculated from

$$\Delta T_2 = \frac{2d}{c_s} + \frac{2(D-d)}{c_w} \quad (7)$$

where

ΔT_2 is the round trip time of the pulse (time between the first and second echo signals) with the TMM placed on the reflector.

d is the thickness of the TMM sample.

Speed of Sound Calculations Using Through-transmission Method

In the through-transmission testing method, the TMM speed of sound calculations have almost the same steps as pulse-echo testing except that, instead of measuring the reflected signals from the samples, this method calculates c_s from the transmitted signal using a second Rx transducer as shown in the sample schematic in Figure 19.

The Tx and Rx are placed in degassed water with a distance larger than the near field distance (Section 3.4.3.3). The transmitted signal through water without the sample is measured from the Rx output. The sample is then placed in the sample holder and the measurements are repeated. The unknown sound velocity of the sample is calculated

from the temporal shift (ΔT) between the pulse transmit times with and without samples as:

$$c_s = \left(\frac{1}{c_w} - \frac{\Delta T}{d}\right)^{-1} \quad (8)$$

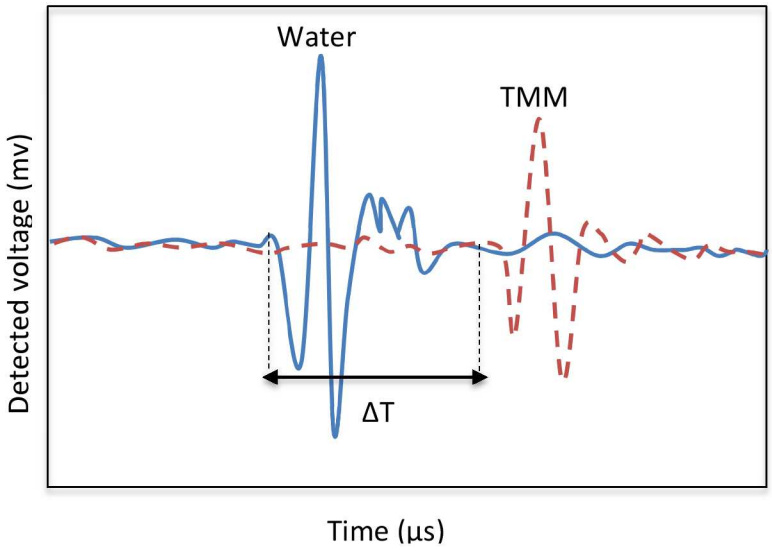

Figure 19: Temporal shift in the signal with and without samples; adapted from (Zell 2007).

3.3.3.2 Acoustic Impedance

Acoustic Impedance, *Z* of a material describes how mechanical energy propagates. The amount of energy reflected at the interface between two materials depends on the difference in their acoustic impedances. *Z* is proportional to both the speed of sound (c_s) and density (ρ) of the material and calculate by Equation 9.

$$Z = \rho . c_s \quad (9)$$

3.3.3.3 Attenuation Coefficient of TMM

Attenuation is the decrease in the amplitude of the sound waves when they pass through a medium. Attenuation generally increases with increasing frequency. Attenuation is usually expressed in terms of an attenuation coefficient and is a material constant. The unit of attenuation coefficient is $dB.cm^{-1}.MHz^{-1}$ and the attenuation coefficient of water is $2.5x10^{-4}.f^2$ $(dB.cm^{-1})$ (Zell 2007) as attenuation coefficient of water increases as frequency squared. The attenuation coefficient of TMM can be calculated

either by the pulse-echo immersion technique or through-transmission method and is relative to the attenuation coefficient of water.

Attenuation Coefficient Calculation Using Pulse-echo Testing

The set-up is again as shown in Figure 16 and the speed of sound in the sample is calculated using Equation (5). Samples of two different thicknesses are placed on the steel reflector and the amplitude measurements of the echo signal are made. The attenuation coefficient, α_s can be derived using Equation 10.

$$\alpha_s = \alpha_w - \frac{1}{2(d1 - d2)} [\ln A_{s1} - lnA_{s2}] \quad (10)$$

where,

A_{s1} and d_1 are the amplitude of the received pulse and the thickness of the first sample and A_{s1} and d_2 those of the second sample.

α_s and α_w are the attenuation coefficients of the samples and water respectively.

Attenuation Coefficient Calculation Using Through-transmission Technique

This technique is also a relative measurement method and uses water as the reference material. The set-up is exactly the same as Figure 17 and the attenuation coefficient, α_s can be derived from Equation 11.

$$\alpha_s = \alpha_w - \frac{1}{\Delta d} [\ln A_s - lnA_w - 2\ln(1 - R)] \quad (11)$$

where

A_i is the amplitude of the received ultrasound pulse with subscripts *w* and *s* to denote water and sample respectively.

Δd is the thickness of the sample.

R is the acoustical reflection coefficient at the water sample interface, calculated by Equation 12:

$$R = \left(\frac{Z2 - Z1}{Z2 + Z1}\right)^2 \quad (12)$$

where,

Z_1 and Z_2 are the acoustic impedances of water and the samples respectively.

The US beam propagates as a longitudinal wave from the surface of the transducer into the propagation medium and the beam exhibits two slightly varying beam patterns; slightly converging beam up to a distance, *N* (near field or Fresnel zone) and a diverging beam beyond that point (the far field or Fraunhofer zone) (Figure 20b).

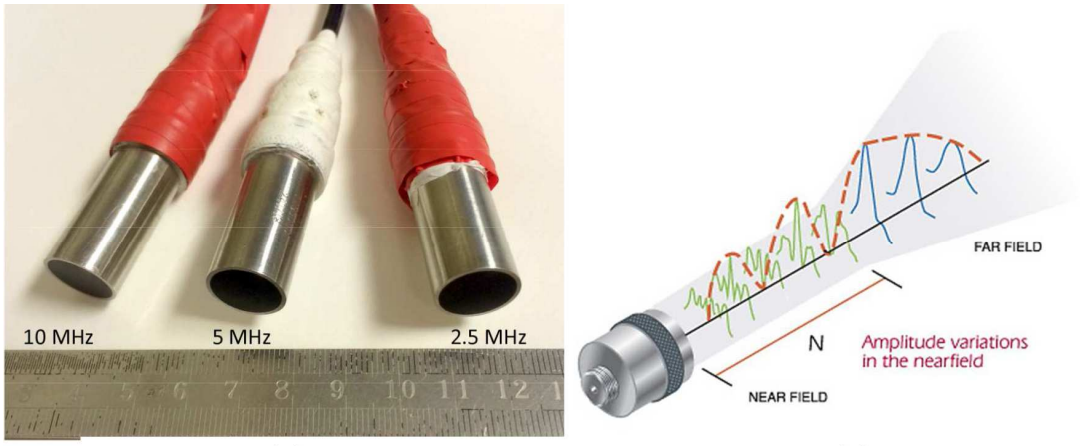

(a) (b)

Figure 20: (a) Transducers used for acoustical testing and (b) schematic representing the near field and far field in a non-focused transducer (Olympus 2015) .

N is dependent on the diameter and wavelength of the transducer and can be defined by Equation 13.

$$N = \frac{d^2}{4\lambda} \quad (13)$$

where,

d is the transducer diameter

λ is the wavelength.

Because of the pressure amplitude variations in the near field, the sample is placed beyond the near field during experiments. Near field distances for transducers were

determined to be approximately 6, 14 and 28 cm for the 2.25, 5 and 10 MHz transducers respectively. After positioning samples of varying thicknesses, the distance between the transducer and sample was adjusted to keep the water path the same thus eliminating changes of attenuation in water as an experimental factor. Five measurements were made for each sample-frequency combination, at room temperature (22°C).

The three pairs of unfocused, disc transducers, used for testing were from Sonatest Ltd, (Milton Keynes, UK), all of 0.5" diameter and with resonant frequencies of 2.25, 5.0 and 10.0 MHz (Figure 20a) The transducers were of medium damping and the part numbers were SLIH2-10, SLIH5-10 and SLIH10-10 for the 2.25, 5.0 and 10.0 MHz transducers respectively. The transducers were connected to the pulser-receiver (DPR300, JSR Ultrasonics) and the corresponding modes were selected (echo or through). Transducers were pulse driven and a pulse length of 15 was used for testing.

Six TMMs (Table 3) were tested to analyse their properties. Two samples were made of each TMM with different thicknesses. The through-transmission method was used for testing samples at 2.25 and 5 MHz. For 10 MHz transducer measurements, the pulse-echo method was used for testing the samples. This was to account for the larger near field length (28 cm) of the transducer and the restrictions this brings to the size of the testing tank.

3.3.4 Results

The acoustic characteristics of different TMMs are shown in Table 4. The longevity of the TMMs, given in Table 4 was calculated by regular checking for micro bacterial growth after their preparation date. These values were calculated by averaging the results from the five repeat measurements. The acoustical properties of these materials match well to the values in the literature. Small variations in the values are assumed to be because of variability in the ingredients used, during preparation, because of the limited availability of some materials in the original recipe (Appendix I). However, the materials meet the required standards in terms of acoustic velocity, impedance and attenuation coefficient, except for agar. The attenuation coefficient for agar was found to be 0.07 $dB.cm^{-1}MHz^{-1}$ (0.08 $dB.cm^{-1}MHz^{-1}$ in literature). The ease of preparation and similarities

in acoustic velocity, impedance and density to human tissue makes this still a material of choice for many applications.

Table 4: Acoustic properties of TMM prepared.

TMM	Density ($Kg.m^{-3}$)	Acoustic Velocity ($m.s^{-1}$)	Acoustic Impedance (MRayl)	Attenuation Coefficient ($dB.cm^{-1}$)			Longevity
				2.25MHz	5MHz	10MHz	
Evaporated Milk-Liquid	1028.8 ± 3.6	1532 ± 2	1.6 ± 0.01	1.29	3.25	5.63	Weeks
Evaporated Milk-Solid	1031.6 ± 5.2	1536 ± 4	1.6 ± 0.01	1.03	2.76	5.18	Weeks
PAA gel	1068.9 ± 1.3	1581 ± 3	1.7 ± 0.007	0.316	0.8	1.92	Weeks
HIFU gel	1004.1 ± 1.4	1536 ± 4	1.5 ± 0.01	0.38	1.2	2.2	Weeks
Grey	1062.5 ± 2.8	1538 ± 2	1.6 ± 0.002	0.98	1.98	5.2	Weeks
Agar	1043.3 ± 1.1	1505 ± 2	1.6 ± 0.005	0.13	0.35	0.8	Weeks

The approximately linear changes in the attenuation coefficient with increasing frequency are shown in Figure 21.

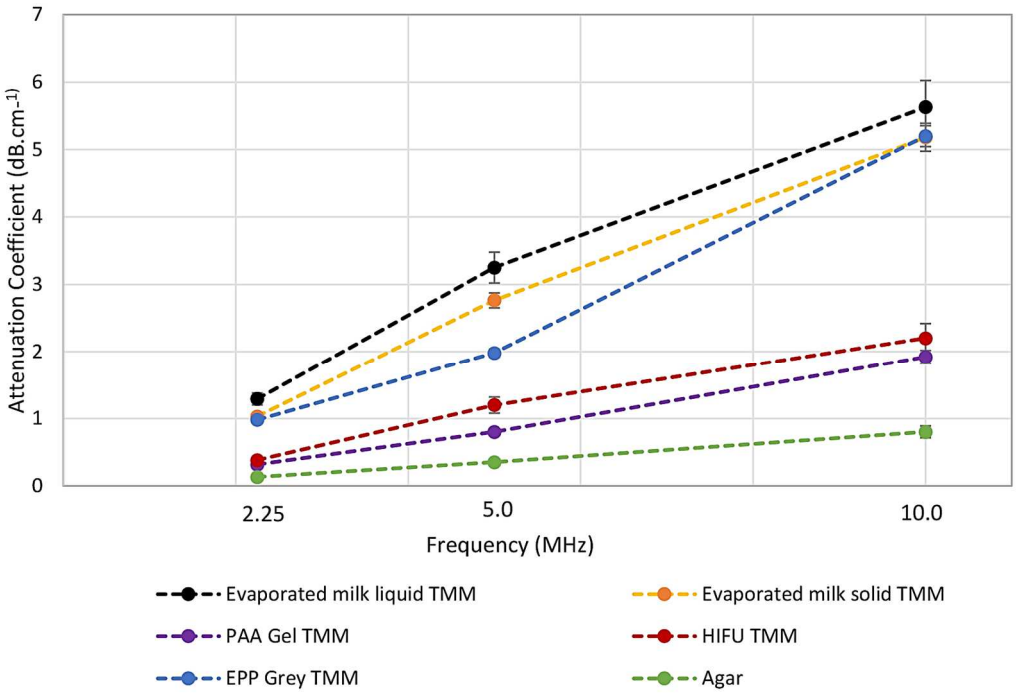

Figure 21: Changes in the attenuation coefficient with increasing frequency.

3.4 MECHANICAL CHARACTERISATION

The elastic properties of TMM are very significant when selecting phantoms for specific applications such as elastography imaging. Unlike acoustic properties, standards have not been defined for elastic modulus ranges for ultrasound TMM (Timothy J 1997). The work reported here calculates elastic modulus for laboratory-made TMM and compares the values with those obtained from an *in-vitro* chicken breast sample.

Young's modulus, *E*, briefly introduced in Chapter Two, is the ability of a material to withstand changes in length when a tensile or compressive force is applied i.e. the stress to strain ratio. It is also known as elastic modulus or tensile modulus. It is a measure of stiffness under isotropic conditions. Young's modulus, E can be calculated using Equation 14.

$$E = \frac{Stress}{Strain} = \frac{\sigma}{\varepsilon} = \frac{{}^{F}/_{A}}{{}^{\Delta L}/_{L}} \tag{14}$$

where,

σ, stress, is the force (*F*) applied per unit area (*A*) that results from an applied load and unit, with units of $N.m^{-2}$ or Pascal (Pa).

ε, strain, is the physical deformation response of a material to the stress and is usually defined as the ratio of change in length (ΔL) to original length (L). As strain is dimensionless, the units of *E* are same as of stress (Julian 2012).

A typical stress-strain curve for a machined material (e.g.: metals) can be seen in Figure 22. When the stress is increased initially, strain developed in the material is linear and this portion of the curve, where the Hooke's law is obeyed, is called the elastic region. After reaching the elastic limit, the application of more stress will make the material reach the plastic region, where deformation in the material is permanent, and further stress on the material will cause the material to reach its breaking point and break. Materials can be defined as ductile, brittle, elastic or plastic, based on the differences in the shape and limits of the stress-strain diagram.

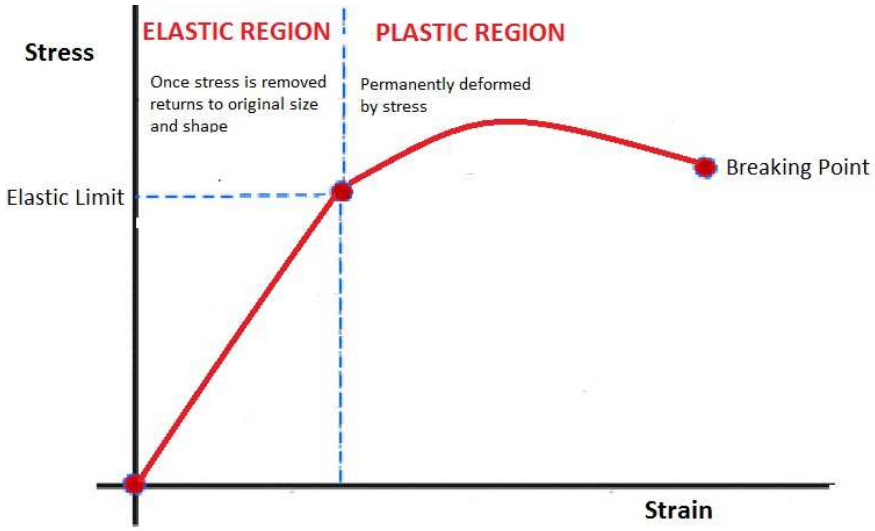

Figure 22: Typical stress-strain graph of an elastic material – adapted from (Serway and Vuille 2011).

When a material is compressed or elongated, the cross-sectional area changes by an amount depending on its Poisson's ratio. Machined materials experience only small deformations and hence the change in the cross-sectional area is negligible and may be taken as a constant. The stress in this case is called engineering stress or nominal stress, σ. However, for viscoelastic or plastic materials, there will be a significant change in the cross-sectional area on applying load and the calculation of stress should be based on the final cross-sectional area instead of the initial area. The stress calculated after accounting for the change in the cross-sectional area is true stress, σ_T. Likewise, the strain produced in the material can be nominal, ε, or true, ε_T, depending on the characteristics of the material. True stress and true strain can be calculated using Equations 15 and 16 respectively.

$$\sigma_T = \sigma(1 + \varepsilon) \tag{15}$$

$$\varepsilon_T = \ln(1 + \varepsilon) \tag{16}$$

where,

σ is the engineering/nominal stress

ε is the engineering/nominal strain

E can be measured from the slope of a stress-strain curve obtained during tensile tests and has been found to range between approximately 1 KPa and 1 MPa in soft tissue (Sarvazyan 1995).

3.4.1 Materials and methods

A cubical mould of dimension, 4 cm^3 was used to make samples of uniform size and shape. Three samples each of all the TMM's were prepared for testing. As mentioned earlier, to provide a comparison, store bought chicken breast samples were also tested. Three pieces of chicken breast were tested 3 times each at room temperature. The tissue samples were cut and shaped into approximate squares and the dimensions were noted in order to calculate areas at later stages of calculation. Unlike TMM samples, chicken breast samples are not isotropic and hence measurements were made in two directions on the samples, across the fibres and parallel to fibres.

The TMM samples, three each for each material were produced from the same batch and compression tests were carried out using a benchtop materials testing machine (Model-H5KS, Tinius Olsen Ltd, UK) with frame capacity up to 5 KN and speed range of 0.001 to 1000 $mm.min^{-1}$. Load cells ranging from 50 N (the lowest available load) to 5 KN were used to test the samples and the 50 N load cell was selected as all the other higher loads resulted in breaking the samples. The sample was placed between the metal plates as seen in Figure 23 and the compression tests were carried out on the with the selected load cell of 50 N and at speeds of 5 $mm.min^{-1}$ for a depth of 5 mm (Figure 23). These steps were repeated five times for all the three samples of each TMM making a total of 15 measurements.

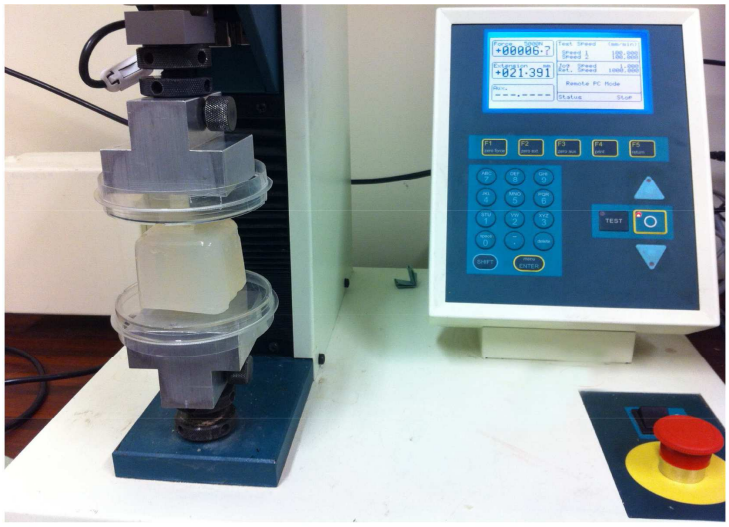

Figure 23: Compression tests on agar TMM

The results from the tests gave details of the force applied and the resulted extensions. The area of the sample was calculated from the dimension (16 cm^2) and the stress was calculated by dividing the force by area. The resulting strain was calculated by dividing the extension and the original depth (4 cm) of the sample. These calculated values of stress and strain were used to calculate the nominal stress and strain using the Equation 14.

True stress and strain values were calculated from these nominal stress and strain values using Equations 15 and 16. After plotting these values in the graph, the linear region of the curve was selected and the slope of the curve was assessed to find the young's modulus values. A detailed description of assessing tissue elasticity values is given in the literature (Madsen 2005, Pavan 2010, Nayar 2012).

3.4.2 Results

The true stress-strain curves of different TMM samples are shown in Figure 24. During the calculation of young's modulus, only the linear region of the curve was selected. It has to be noted that these curves look different to Figure 22 (i.e. they curve up rather than down) and this is because of the fact that it shows true stress & strain instead of nominal stress and strain in the former.

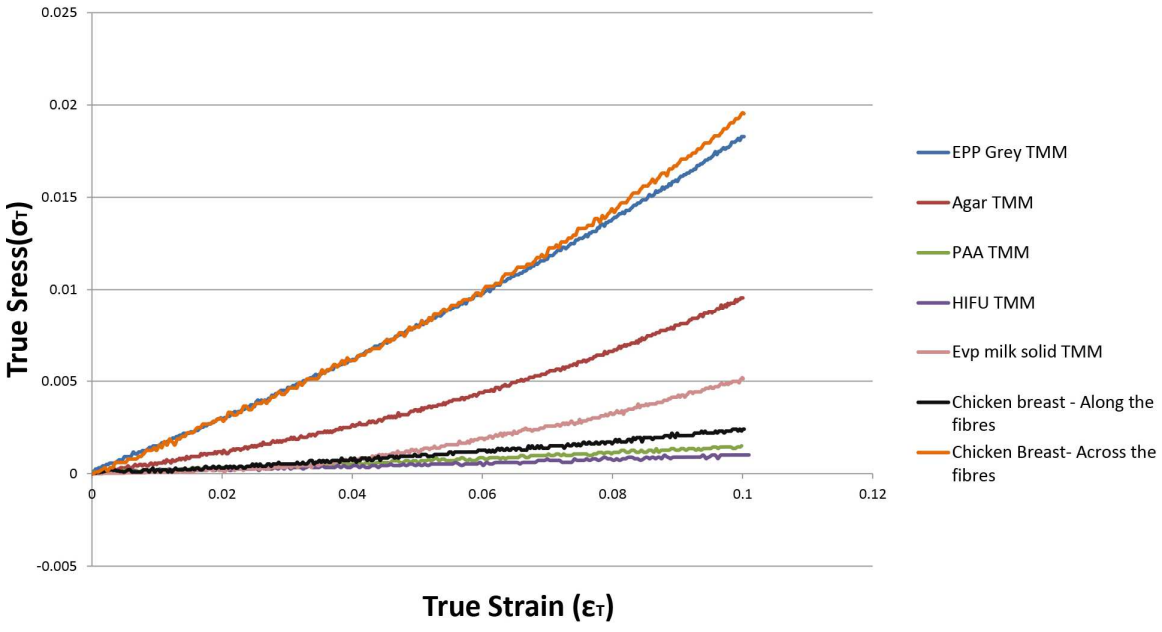

Figure 24: Stress-strain curves of different TMM samples.

While EPP grey TMM was showed to exhibit the most similar mechanical characteristics to a chicken breast sample across the fibres, the polyacrylamide gel-based TMM (PAA and HIFU TMM) exhibited higher amounts of strain for lower stress values. Chicken breast was selected for comparison because of its composition (pure muscle tissue). However, like mentioned before, because of its isotropic structure, measurements were made in two directions, across and along the fibres.

As seen from Figure 24, there is significant difference between these measurements made in two directions. When stiffness values of chicken breast sample, tested across the fibres showed resemblance to the EPP grey TMM stiffness, the stiffness values of chicken breast sample, tested along the fibres showed similarity to the stiffness values of PAA and HIFU TMM. Linear regions of the true stress- strain curves (Figure 24) were analysed and the young's modulus values were determined by calculating the slope of the elastic region of the curve. Three samples of each TMM was assessed and the average stiffness values are shown in Table 5. The tests were repeated five times for each sample to reduce the uncertainties in the measurements. The uncertainties shown in Table 5 shows the standard deviation in the young's modulus values between different measurements.

Table 5: Young's modulus values of TMM

Material	**Young's modulus , *E* (KPa)**
EPP Grey TMM	151.3 ± 3
Evaporated milk solid TMM	59.4± 3
Agar TMM	75.3 ± 4
PAA TMM	13.9 ± 1
HIFU gel TMM	9.9 ± 1
Chicken breast tissue	151.5 ± 4

3.5 CONCLUSIONS

This Chapter discussed the needs of different US test objects and a range of TMMs suitable for testing the widely used, B-mode US systems testing were prepared in the lab. The acoustic properties of these TMM were measured and compared with the values in the literature. All materials tested, except agar met the standards in terms of

acoustic velocity, acoustic impedance and attenuation coefficient. Elasticity measurements of these TMMs, defined by Young's modulus, were determined using compression testing.

These values of E were obtained using static loading. An interesting future work will be to determine the young's modulus values of these TMMs using other dynamic techniques such as using SWE. Since stiffness of the tissue is a material property, it is unlikely to show significant changes between static and dynamic measurements of E and for the purpose of the work presented in this thesis, this was out with the scope. Hence, the measurements made using static loading of different TMMs were compared with fresh chicken breast tissue, tested across and along the fibres, EPP grey, PAA and HIFU TMM showed the most similarities in terms of Young's modulus.

SECTION II

Soft-embalmed Cadavers

Although artificial phantoms for US testing have become increasingly sophisticated, they are still a poor substitute for human anatomy. The use of volunteers for *in-vivo* testing is possible, but inconvenient, because of the paper work involved. In addition, *in-vivo* tests does not allow repeated tests on identical anatomy and is inappropriate for invasive techniques such as intraoperative ultrasound and FUS. The use of fresh human cadavers is possible but carries expense and risk of infection and does not allow repeated tests over more than the very short term.

This section of the thesis explores the potential of cadavers, soft-embalmed using the Thiel technique, for medical ultrasound research and testing of new US systems. The section consists of four Chapters. Chapter Four begins with a literature review of TEC and reports the quantitative imaging of TEC using US SWE. The suitability of these cadaver models for interventional US research is explored further in Chapter Five. Chapter Six assesses the suitability of TEC breast tissue for therapeutic US research and Chapter Seven analyses Thiel-embalmed mice models for high frequency µUS imaging.

CHAPTER 4

Quantitative Analysis of Thiel-embalmed Human Cadavers Using Shear Wave Elastography System

4.1 INTRODUCTION

TEC are increasingly being used as simulators for medical training and research. These models can be considered as realistic, qualitative models for testing systems and for device development. This Chapter begins with a background section on human cadaver models. This is followed by a specific case study to assess the tissue stiffnesses of TEC using SWE.

4.2 BACKGROUND

Human bodies are used in most parts of the world as an educational tool for medical students. Anatomy is taught through body dissection and by demonstrating dissected specimens. The bodies used for these purposes are generously offered by the donors for the improvement of medical science and education. These bodies are usually referred to as 'silent teachers' (Eisma and Wilkinson 2014) as they help the students to learn what they cannot from books and other artificial models.

In addition to being an educational tool, the cadavers are also used as models for testing instruments and procedures at the pre-clinical stage of the development. As it is impractical and unethical to try any new approaches on patients, the benefits these cadaver provide towards medical research is exceptional. While other models such as phantoms or live animals are available, the human body remains the most appropriate model from an anatomical point of view.

4.2.1 Body Preservation Methods

Several techniques have been used for a long time for preserving the dead ranging from natural methods, such as mummification or freezing, to artificial methods, such as immersion or arterial injection (Brenner 2014).

4.2.1.1 Natural Methods

Freezing the body and desiccation by dry cold or dry heat is the only natural method of preserving the tissues known so far. FFC can be kept for an indefinite period in freezers with temperatures between -17 and -20°C. The bodies need to be moved to temperatures ranging from 3°C to 5°C for up to 2 weeks before they are defrosted and ready to use. This method retains the colours and flexibility of tissues as in the living

body making it an efficient model for laparoscopic skills training (Kang 2009, Sharma and Horgan 2012), airway management (Reid 2013), endoscopic surgery training (Krishnan 2004), percutaneous liver biopsy training (Bruining and Arora 2007) and other procedures. Despite being realistic and flexible, some of the main disadvantages of FFC include high risk of infections, need for full personal protective equipment, short period available before deterioration and possibility of inadequate thawing.

4.2.1.2 Artificial Methods

The main prerequisites for using human bodies for medical research is their efficient preservation and this is achieved by treating bodies with specific chemicals i.e.; embalming. The embalming fluid contains chemicals that include preservatives, germicides, buffers, wetting agents, anticoagulants, colorants and scenting agents. These chemicals are combined in different proportions to produce the fluid (Brenner 2014).

Formalin embalming is the most common artificial embalming method and was first reported in 1899 (Brenner 2014). This method uses high concentrations of formaldehyde for tissue preservation. The main advantages of this method are longevity, minimal infection risk and easier handling of solid organs. The bodies can be stored at room temperature and are typically used for dissection based anatomy education and research (Eisma and Wilkinson 2014). Although formaldehyde is a good tissue preservative, it is commonly associated with tissue hardening and rigidity. Besides these disadvantages, formaldehyde also has others such as rapid coagulation of blood, discolouration, constriction of capillaries, deterioration over time and an unpleasant smell (Mayer 2012).

Formalin also tends to cause moulding when the bodies are exposed to air for an extended periods of times (Bradbury and Hoshino 1978). Formaldehyde exposure has been shown to have several adverse and toxic effects on the embalmers and other users (Mori 2013, Abhijeet and Mukul 2014). It has also been classified as carcinogenic to humans (Hauptmann 2009, Lunn 2010). Thus, the exposure limits of formalin have recently been reduced which, in turn, increased the demand for an embalming method using less or no formalin (Eisma 2013). There is also a warning that formaldehyde may

be prohibited for embalming purposes by the Biocidal Products Directive 98/8/EC (European Parliament and Council, 1998).

Soft-embalming techniques are preservation methods making use of low levels of formaldehyde compared to formalin embalming. A range of soft-embalming methods is currently being used around the world. Brenner (2014) gives a comprehensive comparison of different embalming techniques used for human body preservation, including old and new techniques. The work reported in this thesis used cadavers embalmed using the Thiel protocol (Thiel 1992a). The specific details of other soft-embalming techniques are out of scope for this thesis and are not discussed further.

4.2.2 Thiel Embalming

Thiel embalming (aka Graz Embalming Protocol) is a soft-embalming method invented by Professor Walter Thiel in Austria over several years, leading to his first publication in 1992. (Thiel 1992a, Thiel 1992b, Thiel 2002). The Thiel method is still relatively unfamiliar and, therefore, little used. A survey conducted in 2011 (Benkhadra 2011) to assess its use worldwide could find its potential usage only in 5 countries (UK, Germany, Czech R, Switzerland and Austria). Unlike Thiel embalming, all other soft-embalming methods have a shorter life span (a few months) and require refrigeration for storage.

Thiel embalming has recently been attracting more attention as it requires no cooling and has long lasting preservation (years). TEC have a life-like appearance, preserved skin colour and excellent tissue flexibility (Figure 25). The Centre of Anatomy and Human Identification (CAHiD) at the University of Dundee was the first place in the UK to use Thiel soft-embalming and about 75 bodies are embalmed here every year (Eisma 13th February 2015).

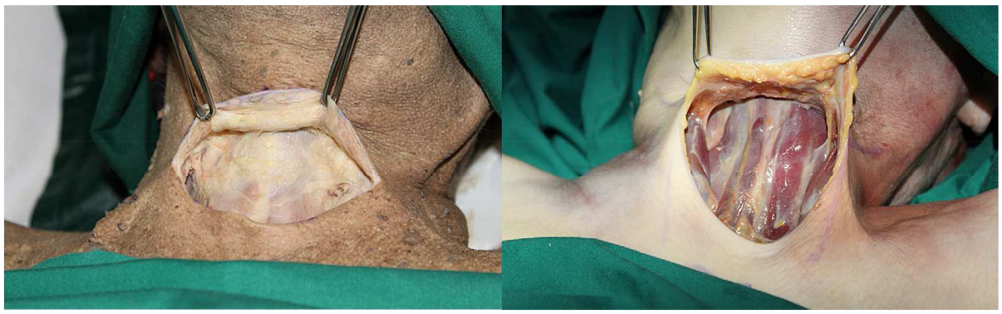

(a) (b)

Figure 25: Raising the subplatysmal flap in Formalin embalmed vs Thiel cadavers (Eisma 2011).

The embalming formula used is slightly different than the most recent documented version (Thiel 2002) in terms of the amount of water and formaldehyde solution, because of the lower concentration of formaldehyde used compared to the standard one (8.9% vs. 37.5% respectively). The embalming process has two main stages: perfusion and immersion. Perfusion is carried out shortly after arrival of bodies by injecting arterial and venous fluids simultaneously. Arterial fluid is normally injected through the femoral or brachial artery and venous fluid through the sagittal sinus or brachial vein (Figure 26). The constituents of all the embalming fluids used are noted in Table 6.

The bodies are then immersed in the tank fluid for 4-6 months before they are completely preserved. After this stage of preservation, the bodies can stay submerged or be stored in plastic bags, without the need for refrigeration. Thiel embalming has shown to be superior compared to other soft-embalming methods in terms of joint flexibility and fungicidal properties (Jaung 2011). Eisma and Wilkinson (2014) have compared TEC with FFC, FEC and other soft-embalming techniques as shown in Table 7.

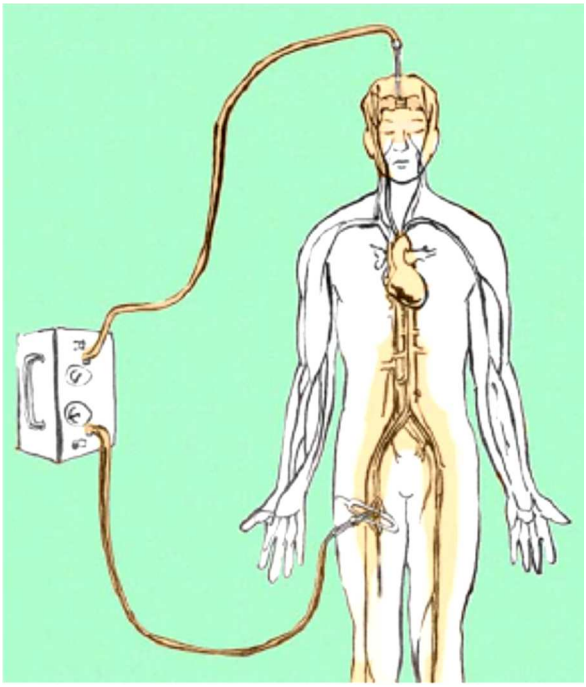

Figure 26-Perfusion stage in the Thiel embalming process(Eisma and Wilkinson 2014).

Table 6: Constituents of the Thiel embalming fluids used at CAHiD (Eisma 2013)

Constituents	Arterial Fluid	Venous Infusion	Tank Fluid	Moistening Fluid
Boric Acid	250g	80g	45kg	600g
Ammonium Nitrate	1680g	520g	150kg	-
Potassium Nitrate	420g	130g	75kg	-
Sodium Sulphate	700g	190g	105kg	1kg
Propylene Glycol	2.5L	780mL	150L	1L
Stock II *	500mL	190mL	30L	200mL
Formaldehyde Solution (8.9%)	2.1L	1.5L	125L	-
Morpholine	150mL	110mL	-	-
Alcohol	1L	1.1L	-	-
Hot Tap Water	6.8L	1.45L	1250L	20L
Total Volume (L)	13	5.5	1720	22

* Stock II is a mixture of 1kg chlorocresol in 10L of glycol and needs to be mixed in advance due to slow dissolution. Total volumes are approximate and based on an average size cadaver and the size of the tank in use.

The reason for the increased flexibility of TEC over FFC and FEC were investigated for the first time in 2011 (Benkhadra 2011). The group compared muscular fibre structures in FFC, FEC and TEC under optical microscopy at different magnifications to evaluate the changes in their ultrastructure.

Major modification of the integrity and alignment of the muscle fibres (suspected to be because of the corrosive effect of boric acid in the Thiel solution) were noticed in TEC when compared to the others. This is explained as the reason for exceptional suppleness of these cadavers. Figure 27 shows the microscopic images of human muscle tissue under 10x magnification (Benkhadra 2011). Muscle fibres in Thiel tissue shows a minced appearance, but remained aligned as seen in Figure 27a.

Table 7: Common embalming methods and their main characteristics(Eisma and Wilkinson 2014).

Preservation Method	Agents	Storage	Period of Use	Advantages	Disadvantages	Typical Use
Formalin	Formaldehyde with possible additions such as phenol & glycerine	Room Temperature	Years	Longevity, minimal infection risk, solid organs may be easier to handle	Stiff, discoloured, unnatural texture, poor tissue plane preservation, odour, low grade carcinogen, not suitable for inhalation or ventilation	Dissection based anatomy & research
Thiel	Glycol, various salts, boric acid,chlorocresol,formalehyde (low levels), alcohol	Room temperature after several months immersion		Flexible joints and tissues , realistic, minor tissue change, long lasting ability to ventilate, preservation of colour	Infrastructure required, time needed for embalming process, not all tissues life like	Both short and long lasting applications in teaching & research
Other soft embalming	Various (e.g.: glycerine, alcohol, formaldehyde etc.	Fridge	Months	Somewhat flexible, some colour preservation	Shorter lifespan, storage in fridge	short term applications in teaching & research
Fresh Frozen		Freezer	Days	Flexible, realistic, minimal tissue change	Infection risk, need for full personal protective equipment, time needed for thawing, deterioration throughout usage period, mounting of body parts when not using full cadaver	Short surgical training courses, short-term research

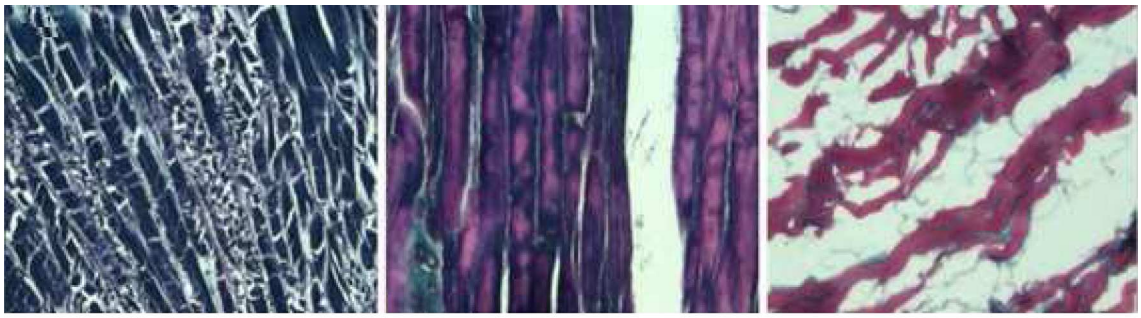

(a) (b) (c)

Figure 27: Masson's trichrome staining of human muscle tissue observed at 10x magnification. (a) Thiel, (b) formalin and (c) unfixed (Benkhadra 2011)

4.2.3 Applications of Thiel Embalming

Although Thiel embalming was first invented in the 1990's, the technique remained relatively unknown until recent years. A comprehensive analysis of its use over the last two decades is presented here. There have been approximately 70 publications till the present date (1992-2014) and the detailed chart in Figure 28 suggests their increased use over the last few years. The search to obtain this data looked for Medical Subject Heading (MESH) terms such as 'embalming' and 'embalming methods' in either the abstracts or the full text of the journal publications. The papers were further analysed to confirm the use of TEC to filter out publications just mentioning their availability in the background.

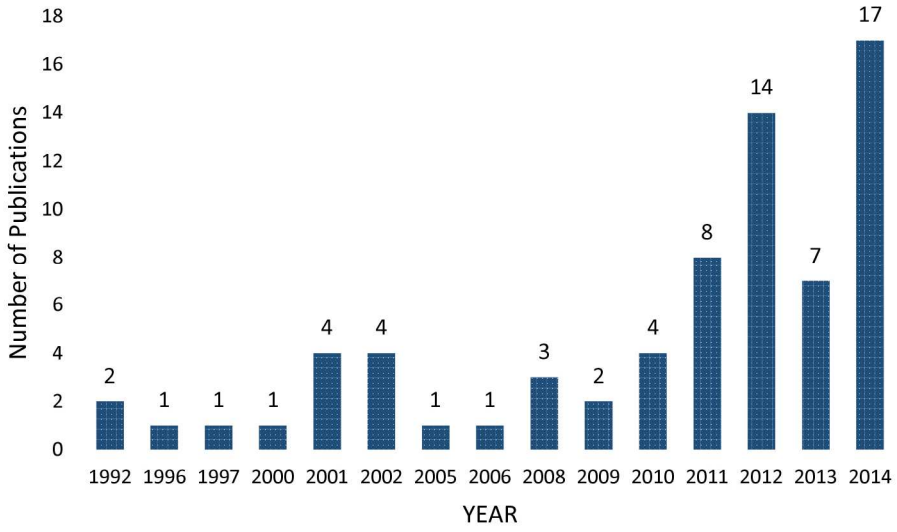

Figure 28: Thiel Publication numbers after 1992.

The applications of TEC are substantial and can be classified further under two main areas: teaching and training, research and development. The applications in the field of medical research and development is discussed further.

4.2.3.1 Research and Development

TEC has proved to be widely useful in medical research as excellent human models aiding the development and testing of techniques and systems. Various studies on knee joint prostheses and their effects used TEC as models and have reported its benefits over FFC and cadavers embalmed using other techniques (Kainz 2012, Wurm 2013). Antireflux surgery and suspected nerve damage were investigated using Thiel models in 2001 by a

urology group in Germany (Leissner 2001). The suitability of TEC for research and education in oral-maxillo-facial surgery was investigated and TEC were reported as an optimal basis for research and training (Peuker 2001).

One of the other major areas that are utilising TEC are plastic surgery research (Hassan 2014, Odobescu 2014). TEC have also been identified as good tissue models for optical nerve measurements (Steinborn 2011), orthopaedic research (Betz 2013), hearing research (Stieger 2012, Guignard 2013), rhinology research (Havel 2014) and MRgFUS research (Eljamel 2014, Gueorguieva 2014, Karakitsios 2014).

The increased flexibility and tactile needle feedback makes TEC suitable for UGRA research (Guo 2012, Munirama 2014). TEC have also been used at CAHiD to analyse the effect of contrast agent injections on an US image. Figure 29 shows the visibility of needles just before injecting the contrast agents. The series of images extracted from the contrast agent injection videos in Figure 30(a-f) shows the spreading of contrast agents imposing acoustic shadows in the images of biceps muscles.

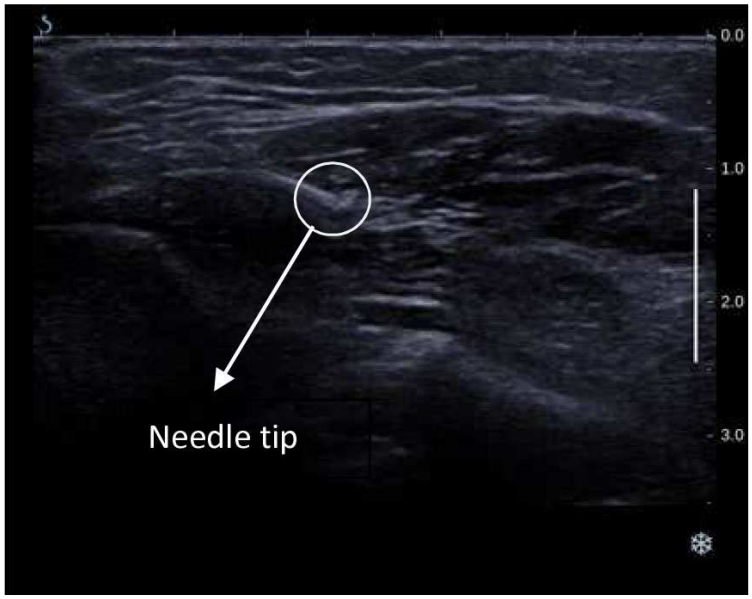

Figure 29: Visibility of needles in TEC

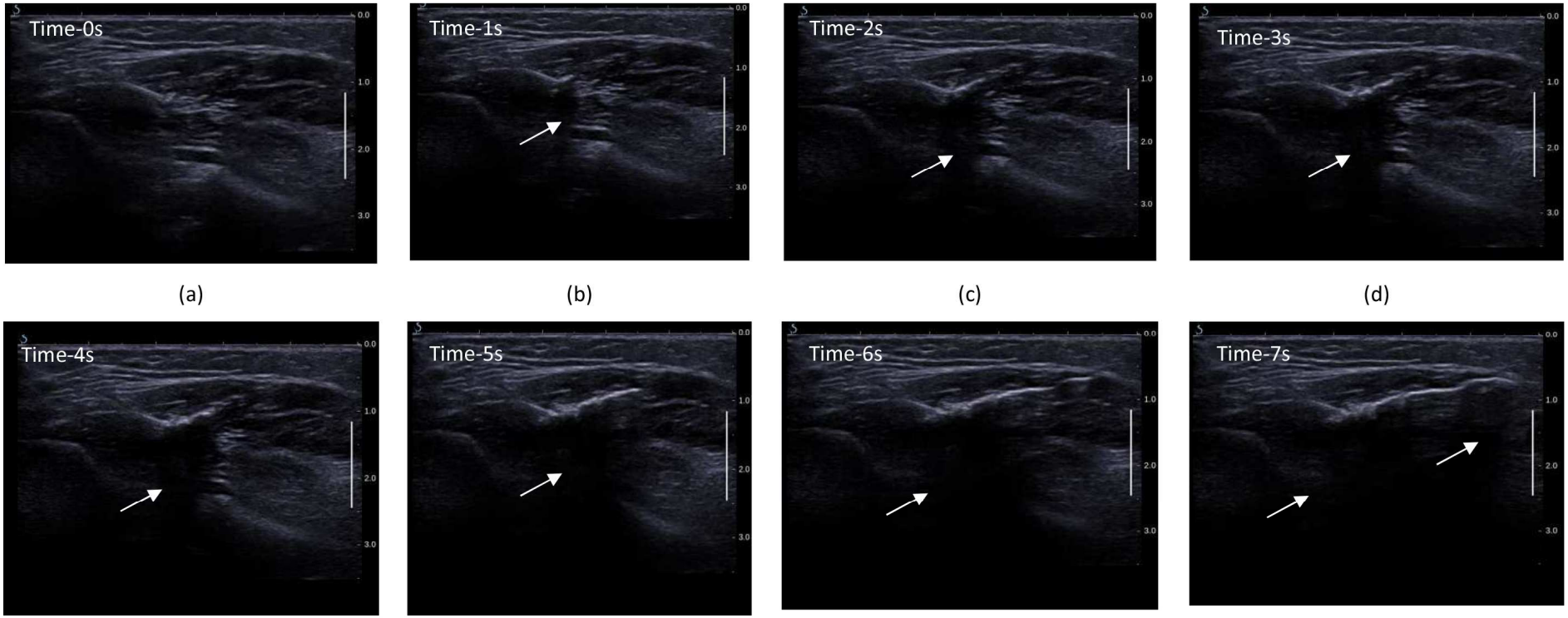

Figure 30(a-f): Image series showing contrast agent injections in TEC biceps muscle and the resulted acoustic shadowing in the images indicated with arrow markings.

4.2.4 Pros and Cons of Thiel-embalming Method

TEC is an efficient simulation of life model with well-preserved organs and tissues pertaining to colour, consistency, flexibility and plasticity (Pattanshetti and Pattanshetti 2010). The wide range of applications for TEC in medical research and training have been elaborated earlier in this Chapter.

Some of the main advantages of TEC are

- Lungs can be ventilated.
- Articular joints remain flexible.
- Low toxicity.
- Almost no coagulation of blood in large vessels.
- Effective bacterial disinfection preventing the development of moulds.
- Unlike FEC and FFC, TEC can be imaged using US systems making them a new resource for US research.

Even though Thiel embalming improves upon several other preservation techniques because of its unique abilities, limitations have also been reported. Thiel embalming provides relatively poor preservation of the brain and sometimes very soft texture of organs such as the uterus. Extremities that do not perfuse very well (hand and feet in some cadavers, occasionally more extensive distal parts of limbs) sometimes initially turn somewhat dark and wrinkly, but this gradually recovers and has not posed any problems (Eisma 2013).

A number of studies have demonstrated biomechanical changes to the musculo-skeletal structures (Unger 2010, Benkhadra 2011, Fessel 2011, Wilke 2011) making them less suitable for biomechanical research. Thiel embalming requires specific facilities and has higher costs than the conventional methods. The limited availability of specific chemicals worldwide and low number of trained personnel also make Thiel embalming relatively less utilised.

4.3 MATERIALS AND METHODOLOGY

Only limited research has been conducted so far to assess the tissue characteristics of TEC to enhance their use for diverse applications. Most studies assessing TEC are qualitative, comparing distinct cadaver models and do not specifically contrast these with live patients (Benkhadra 2009, Eisma 2011, Hassan 2014). Hence, there is a need to quantitatively validate the tissue properties of this model against living subjects. The principal objective of this study is to measure the tissue elasticity of TEC and validate the results with a known human cohort.

Using quantitative shear SWE superimposed on B-mode US, two independent raters undertook 10 repeated measurements of Young's modulus within the thyroid, parotid and submandibular glands, and gastrocnemius and masseter muscles and supraspinatus tendon of eight TEC. The elastic property (Young's modulus) values of these tissues were compared with values reported for living individuals (Arda 2011). The work presented in this Chapter has been accepted for external publication (Joy 2015). Correlation between the tissue elasticity values and various factors such as age of the cadaver at death, DoE and gender were statistically analysed using IBM SPSS (version 20.0, SPSS) software.

4.3.1 Study Sample

After obtaining permission from the TEC ethics group, eight TEC were selected randomly for this study (4 males, 4 females; mean age: 81.75 ± 11.20 years, range: 63-97 years). These cadavers varied slightly in terms of their final preservation stage: six of the bodies were immersed in a tank of embalming fluid for the last stage of preservation and two of them were preserved in a plastic bag of embalming fluid due to lack of space in the tank at the time of their embalming.

Six tissues specifically selected for scanning were the thyroid, parotid and submandibular glands, gastrocnemius and masseter muscles and supraspinatus tendon. These tissues were particularly selected because their stiffnesses in human beings had been reported in the literature. The anatomy of these tissues (VirtualMedicalCentre 2014) and the region scanned in the study (Ultrasoundpaedia 2014) are shown in Table 8.

Table 8: Anatomy and scanning regions for the tissues under study (Ultrasoundpaedia 2014, VirtualMedicalCentre 2014)

Thyroid	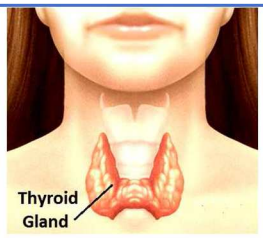	
Submandibular Gland	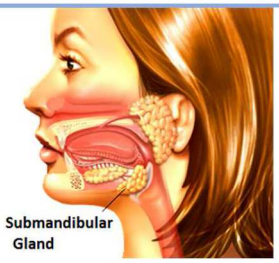	
Parotid Gland	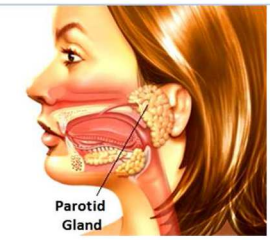	
Supraspinatus Tendon	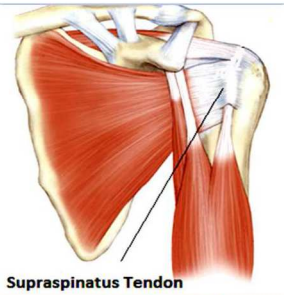	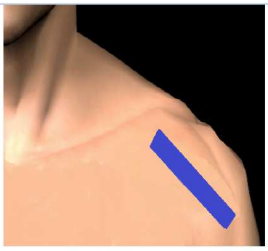
Gastrocnemius Muscle	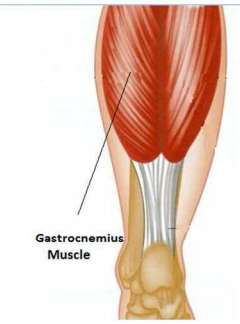	
Masseter Muscle	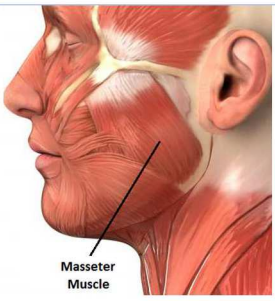	

The data collected included ten measurements each of all the six tissues from the eight cadavers, giving a total of 60 measurements for each subject, apart from two, as one of the subjects lacked a thyroid gland and another had dessicated gastrocnemius muscle, making the total number of measurements 460 ([6 tissues * 8 subjects * 10 measurements] – [2 subjects *10 measurements]). Table 9 shows the details about the study sample for all the eight subjects. They are classified according to their gender, age, days of embalming (DoE) and preservation type. Tissues with successful elasticity measurements recorded are marked with a tick ('✓') symbol and those that could not be measured with a cross ('✗') symbol.

Table 9: Study sample details

Gender	Age	Bag/ Tank	DoE	Parotid	Masseter	Sub Mandibular	Thyroid	Supraspinatus	Gastrocnemius
Male	75	Tank	142	✓	✓	✓	✓	✓	✗
Male	83	Bag	124	✓	✓	✓	✓	✓	✓
Male	86	Tank	103	✓	✓	✓	✓	✓	✓
Male	63	Tank	64	✓	✓	✓	✓	✓	✓
Female	97	Tank	69	✓	✓	✓	✓	✓	✓
Female	94	Tank	68	✓	✓	✓	✓	✓	✓
Female	83	Bag	221	✓	✓	✓	✓	✓	✓
Female	73	Tank	81	✓	✓	✓	✗	✓	✓

4.3.2 Scanning

Scanning was undertaken in CAHiD, University of Dundee, under the supervision of the Anatomy Officer acting under the auspices of the Anatomy Act (Scotland) 2006. The US imaging and the stiffness analysis were performed using SWE superimposed on B-mode US (Supersonic Imagine, Aix-en-Provence, France). Two independent raters undertook 10 repeated measurements (5 each) of Young's modulus of six sites - thyroid, parotid and submandibular glands, gastrocnemius and masseter muscles, and supraspinatus tendon.

All tissues were scanned with the cadavers in supine position (Figure 31) except for gastrocnemius muscle scanning where the cadavers were positioned in prone position. The scanning was carried out using a linear array transducer (R3.2 Supersonic Imagine) of bandwidth, 4 to 15 MHz. Higher frequencies were selected for imaging superficial structures and the deeper tissues were imaged using lower frequencies. To ensure

sterility, the probe was covered with a long sterile sheath. Images were stored in the JPEG format on a secure computer.

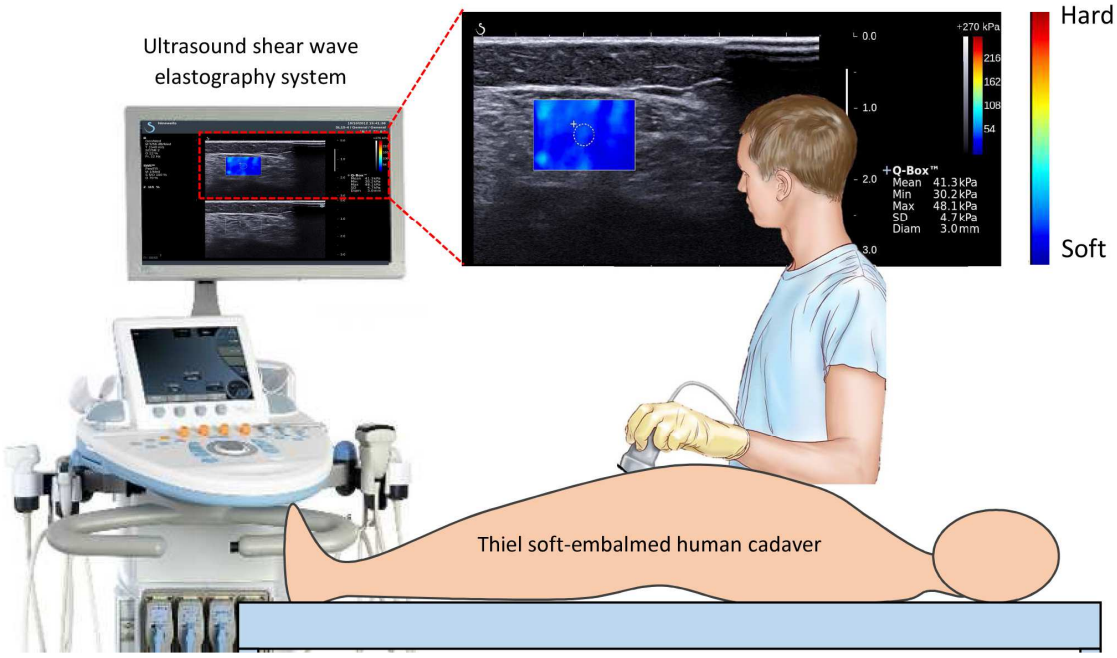

Figure 31: Illustration of operator scanning cadaver in supine position using SWE system.

4.3.3 Statistical Analysis

The study used linear mixed models (LMMs) to analyse the correlation of factors such as age, gender, DoE, tissue type and embalming type with the tissue elasticity values. These particular statistical regression models were selected because of their ability to incorporate both fixed and random effects into the analysis and also account for repeated measurements. Because of their advantage in dealing with missing values, which, in the present case, are sets of measurements for two tissues in two different subjects, mixed effects models were preferred over more traditional approaches such as repeated measures ANOVA. A LMM is a statistical regression model including both fixed and random effects. Fixed effects are factors in the model that represent observed quantities in terms of explanatory variables and random effects are treated as if they arise from random causes.

The general LMM in matrix form can be represented as

$$y = X\beta + Zu + \epsilon \tag{17}$$

In Equation 17,

y is the known vector of observations (elasticity).

X is the fixed effects design matrix in the model (Age, Gender, DoE, Tissue type).

Z is the random effects design matrix in the model (Cadaver, Embalming type).

β is the unknown vector of fixed effects.

u is the unknown vector of random effects.

ϵ is the unknown vector of random errors.

The term mixed model (Equation 17) refers to the use of both fixed, random and repeated effects in the same analysis. Fixed effects have levels that are of primary interest and would be used again if the experiment was repeated. Random effects have levels that are not of primary interest, but rather are thought of as a random selection from a much larger set of levels. The fixed effect assumes that individual specific parameters are correlated with the dependent variables, i.e. elasticity in this case. The random parameters that are uncorrelated with the independent variables are treated as random effects (Dodge 2006). The age, gender, tissue type and DoE are fixed effects whereas embalming type and cadavers are random effects on the elasticity.

Analysis of the data was performed with IBM SPSS (version 20.0, SPSS) software. Descriptive statistics were used to summarise the characteristics of the study group, including means and standard deviations of all continuous variables. Statistical significance was defined as probability, $p < 0.05$.

4.4 RESULTS AND DISCUSSION

SWE images of tissues under study showed good qualitative similarity to and tissue comparison with the humans. Figure 32 shows US B-mode images of the gastrocnemius muscle, supraspinatus tendon and parotid gland obtained from the TEC and the corresponding B-mode images from humans *in-vivo (Ultrasoundpaedia 2014)* . Since the main aim of the work presented in this Chapter was to assess the properties of TEC and since the in-vivo volunteer B-mode images were readily available in the literature, volunteer scans were not conducted in-house. One of the other main reason for not conducting in-house volunteer imaging was the relatively time consuming ethical approval process when considering its need for the present work.

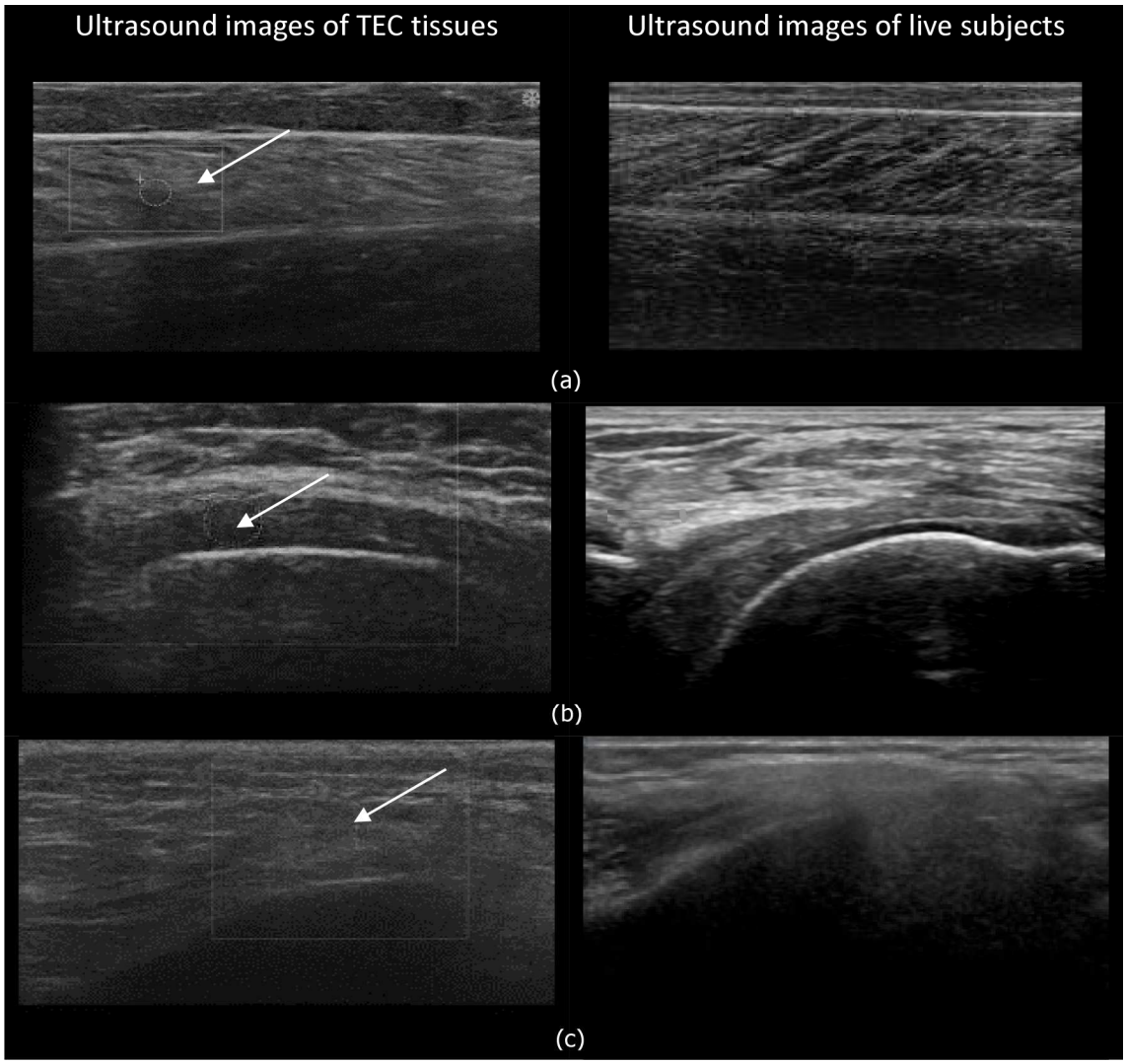

Figure 32: Comparison of TEC tissue US B-mode images (left) to the library reference images from subjects in-vivo (right) of (a) gastrocnemius muscle (b), supraspinatus tendon (c) and parotid gland.

The US B-mode and the corresponding SWE images of the different tissues under study are shown in Figure 33(a-f). The SWE system permits the user to select a ROI in the image and this displays the elastography colour map ranging from blue to red, blue being the softest tissue and red the stiffest in the ROI. The stiffness measurements could be made anywhere in the ROI and stored. The stiffness data of the selected ROI contains the minimum, maximum and mean values of tissue elasticity indicated in units of kPa.

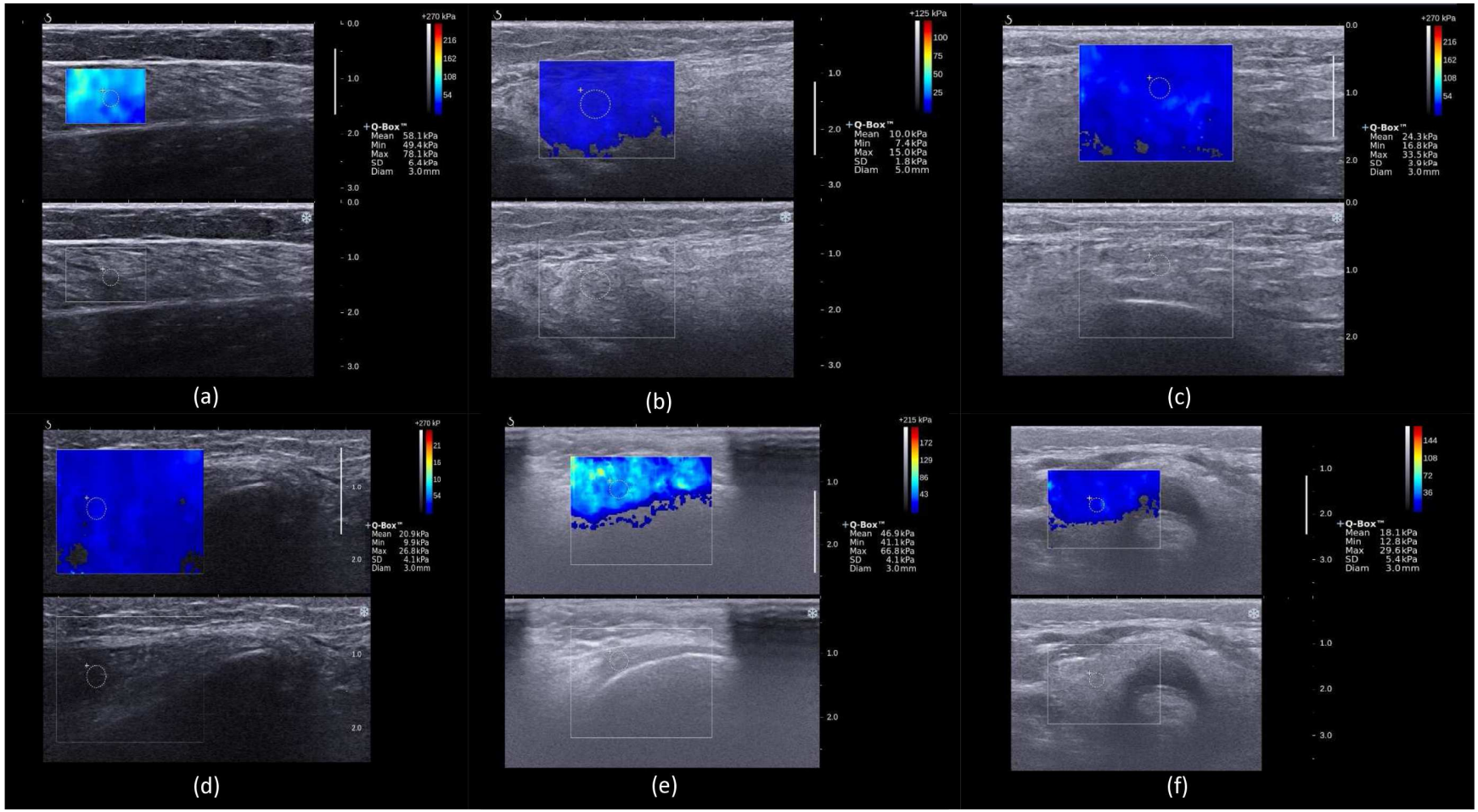

Figure 33:(a-f) - The B-mode and the corresponding SWE images of gastrocnemius muscle (a), submandibular gland (b), masseter muscle (c), parotid gland (d), supraspinatus tendon (e) and thyroid gland (f).

4.4.1 Factors Affecting Tissue Elasticity

4.4.1.1 Embalming Type (Tank vs. Bag)

The elasticity values were found to be significantly different between cadavers embalmed in tanks (sample size: 6) with those in bags (sample size: 2). From observation, while the bodies in tanks remained flexible and soft, those in the bags were significantly more rigid, dried out and stiffer. This is assumed to be because of the lesser amounts of immersing fluid for the subjects in the bags (Eisma 12th October 2012). The data sets from different tissue sites acquired from cadavers embalmed in tank and bag were statistically assessed and the differences were found to be statistically significant in all the tissue sites (p=0.00). The tissue stiffness values for bag-embalmed cadavers were found to be higher compared to those in tanks, as shown in Figure 34.

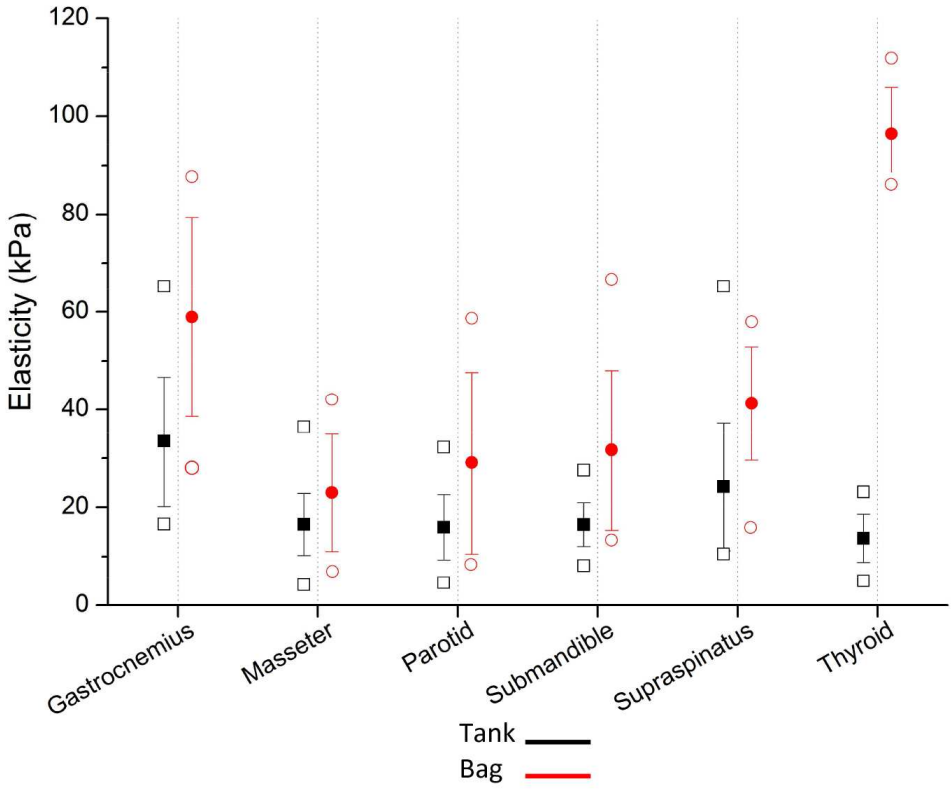

Figure 34:Tissue elasticity measurements for subjects in Tank vs. Bag (Filled squares and circles represent the mean measurements, unfilled squares and circles denotes the maximum and minimum recorded values and the small colour coded 'hyphens' showing the standard deviation).

This finding is very useful as it suggests one way to achieve proper selection of a cadaver for a specific application. While a subjects embalmed in a bag is less useful for research

related to tissue properties, it will find many uses for studies needing slightly stiffer subjects such as biomechanical studies and surgical training.

4.4.1.2 Gender

The stiffness values from the eight cadavers (4 males; 4 females) is shown in Figure 35. The figure suggests generally some changes in the tissue stiffness according to gender. However, mixed model analysis found this difference to be statistically insignificant ($p > 0.05$).

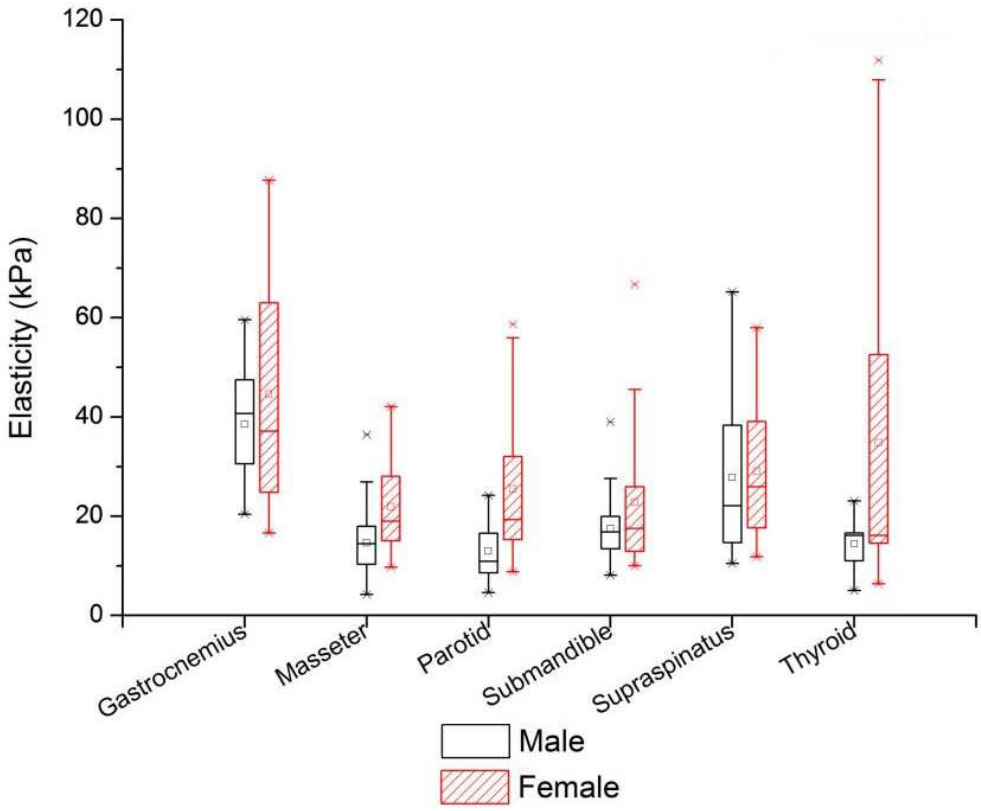

Figure 35: Tissue elasticity values of male vs. female TEC.

The data within the rectangular box represents the 25 and 75 percentiles. The end of the whiskers (the extended black and red solid lines from the box to the 'hyphen') are the upper inner and lower inner fence values, calculated as below

Upper Inner Fence = 75th Percentile + (1.5 * Interquartile Range)

Lower Inner Fence = 25th Percentile - (1.5 * Interquartile Range)

The unfilled small square box inside the rectangle is the mean and the solid line across and inside the box is the median of the elasticity values. This particular plot showing the

interquartile range was specifically selected for this figure to give the readers an idea of the spread of the data sets.

4.4.2 Elasticity Measurements

Least Squares Means of Young's modulus data calculated for mean tank immersion time (88.7 days) and mean age (81.3 years) are shown in Table 10. Data is presented as mean (95%CI). The calculation excluded the data sets from the two subjects embalmed in bags for efficient comparison of results with healthy volunteers. The results are shown for different tissues, gender and all ten repeats.

Table 10: Least Squares Means of Young's modulus data for mean tank immersion time (88.7 days) and mean age (81.3 years).

	Covariates	Elasticity/Young's modulus (KPa)
Tissue	Gastrocnemius Muscle	31.5 (95%CI: 13.2 to 75.2)
	Masseter Muscle	15.0 (95%CI: 6.3 to 35.5)
	Parotid Gland	14.3 (95%CI: 6.0 to 34.1)
	Submandibular Gland	15.5 (95%CI: 6.5 to 37.0)
	Supraspinatus Tendon	20.9 (95%CI: 8.8 to 49.4)
	Thyroid Gland	14.4 (95%CI: 6.1 to 34.5)
Gender	Male	14.0 (95%CI: 4.2 to 47.5)
	Female	22.4 (95%CI: 6.7 to 75.9)
Repeats	1	19.3 (95%CI: 8.2 to 45.6)
	2	17.8 (95%CI: 7.5 to 42.1)
	3	17.3 (95%CI: 7.3 to 40.9)
	4	17.3 (95%CI: 7.3 to 40.4)
	5	17.8 (95%CI: 7.5 to 42.1)
	6	16.9 (95%CI: 7.2 to 40.0)
	7	17.5 (95%CI: 7.4 to 41.3)
	8	17.3 (95%CI: 7.4 to 40.9)
	9	18.9 (95%CI: 8.0 to 44.7)
	10	18.0 (95%CI: 7.6 to 42.5)

Because of the significant differences in tissue stiffness of the two TEC embalmed in bags, those data sets were excluded from comparison with human *in-vivo*. Thus stiffness data from the six cadavers were compared with the data from the human volunteers (Figure 36). The figure shows the differences in tissue stiffness values for the gastrocnemius muscle tissue between TEC and human volunteers *in-vivo.*

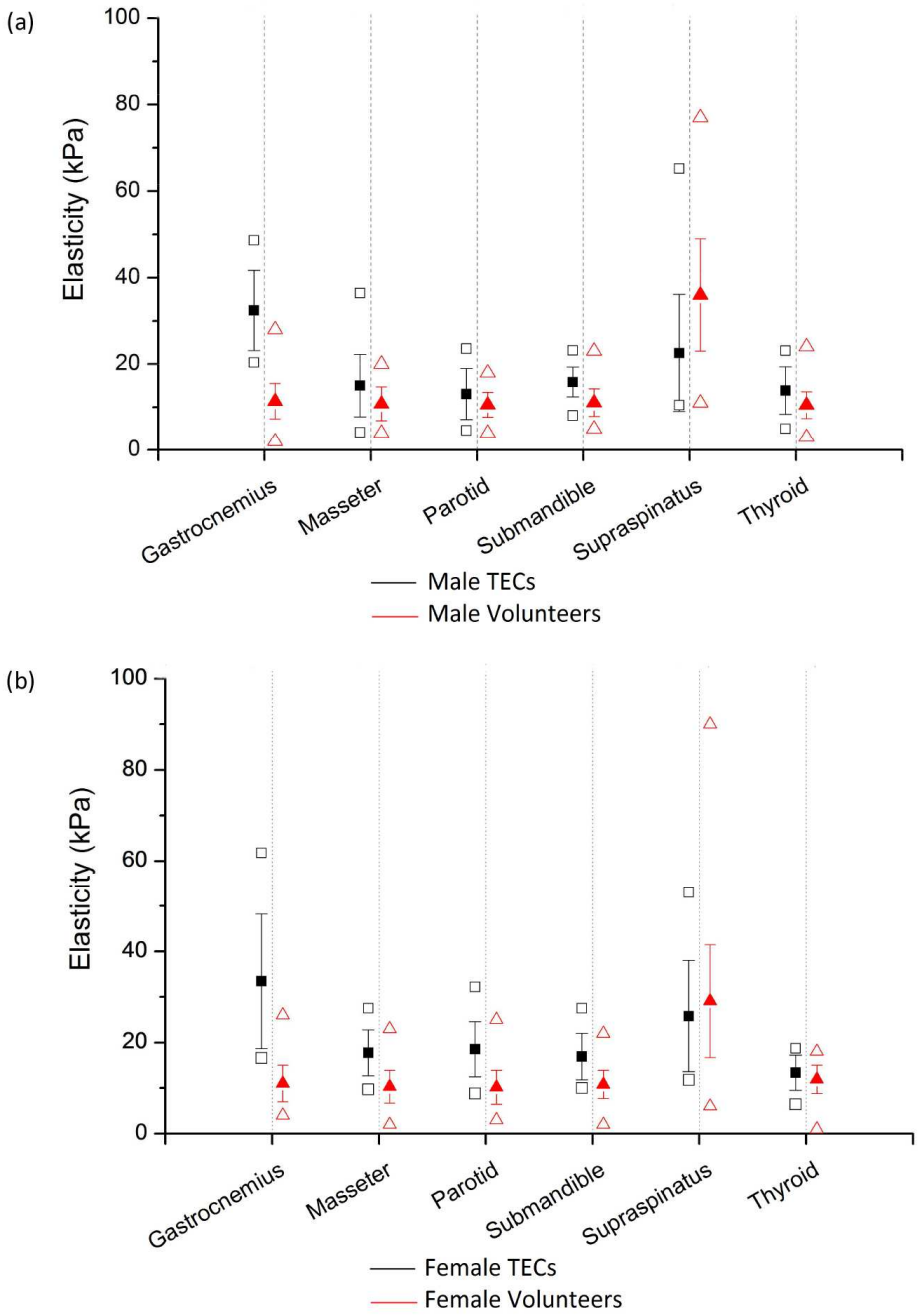

Figure 36: Tissue stiffness values of TEC compared with data from human in-vivo (Arda 2011)(a) male and (b) female. Filled squares and triangles represent the mean measurements, unfilled squares and triangles denotes the maximum and minimum recorded values and the small colour coded 'hyphens' showing the standard deviation.

4.4.3 Statistical Analysis

Apart from finding the differences in the tissue elasticity in TEC, the secondary objectives of this study included regression analysis of Young's modulus against covariates such as gender, age at death and number of DoE. An individual comparison hypothesis test of Young's modulus for mean tank immersion time (88.7 days) and mean age (81.3 years) showed differences, $p < 0.01$, between gastrocnemius and all other tissues, and differences, $p < 0.01$, between Supraspinatus and Masseter, Parotid, Sub-mandible and thyroid tissue. DoE is found to affect the elasticity of the tissues in TEC with significance level $p \simeq 0.00$ (<0.05). Inter-observer errors were found to be non-significant with $p = 1.0$. The analysis did not find a significant correlation between age and gender to the tissue elasticity values ($p=0.436$ and 0.46 respectively); this result coincides with the findings in the literature (Arda 2011).

4.5 DISCUSSION

The increased stiffness for the gastrocnemius tissue in both the male and the female cadavers (Figure 36) might be explained by the difference in the scanning position for the cadavers and the volunteers. In the reference volunteer study, the gastrocnemius muscle stiffness was recorded with the volunteers in a prone position with their foot hanging over the edge of the examination bed in a relaxed position (Arda 2011).

Because of the difficultly in positioning the cadaver in a way to hang their legs over the scanning table, the scanning of gastrocnemius muscle was performed after positioning the cadaver in just the prone position. The statistical analyses also show various interesting findings about the relationship between the various other parameters previously noted and the stiffness of the TEC. The mixed model analysis did not identify a significant correlation between the age of the cadaver at death and the tissue stiffness.

In the volunteer study, statistical analysis found no significant correlation between the tissue elasticity and age of volunteers, in agreement with the present study. The statistical analysis showed a positive correlation between DoE and the tissue elasticity, indicating that the tissue tends to become stiffer as the number of days after embalming increases. TEC tend to appear stiffer and drier when they are left outside the embalming tank fluid for many days. The cadavers embalmed earlier have found more previous use

for training and other work than most recently embalmed bodies causing them to be away from immersion tank for longer periods, making it drier and stiffer (Eisma 12th October 2012). The 20-25L fluid pumped into the cadaver at the start of embalming procedure gradually leaks out and this loss of fluid is faster when the body is out of the tank.

4.6 CONCLUSION

This Chapter indicates that SWE is a useful tool to assess Thiel cadaver tissue/organ stiffness. In other words, TEC model, because of the extend of similarity of tissue stiffness to *in-vivo* humans, can be used as a qualitative human model in testing SWE system. Quantitative assessment of six different tissues from eight cadavers was performed and it was determined that TEC are good models for US studies, with changes in the tissue stiffness documented with reference to the measurements from the six different tissues. This is relevant as it allows to assess the degree to which cadavers are similar to patients and hence assists in judging if cadavers are suitable for particular procedures and in selecting the most appropriate one. TEC are physically very similar to living people, but there are changes over time.

Significant correlation ($p=0.01$) was found between cadaver values and the *in-vivo* elasticity values for same tissues in the literature, demonstrating the life-like characteristics of TEC. SWE was found to provide valuable information on the properties of the cadavers in general, and to be a promising tool to assess an individual cadaver's suitability for certain procedures. The study also looked at the relationship with gender, age of the cadaver at death, and the number of DoE. The results indicate that DoE has strong positive correlation with the elasticity values of the tissues. No significant correlation was found between the age of the cadavers at death and the gender to the tissue elasticity. To conclude, the soft tissue elasticity of TEC has been successfully validated against human tissue *in-vivo*. The results indicate great similarity of TEC models with human *in-vivo,* suggesting their suitability as a tissue model for testing new systems in the US field.

CHAPTER 5

Thiel-embalmed Human Cadavers for Ultrasound Guided Regional Anaesthesia

5.1 INTRODUCTION

TEC, introduced in Chapter Four are assessed in this Chapter for use as tissue simulators in UGRA, interventional US research. Two case studies are reported in this Chapter. The first study intended to explore the possibilities of using a SWE US system in imaging nerves during regional anaesthesia and the second aimed to assess the needle visibility during UGRA, both using TEC models. Both these studies were designed with the help of Anaesthetic department at NHS Tayside, Dundee. Joyce Joy conducted the studies under the supervision of Dr. Shilpa Munirama and Dr. Graeme McLeod. Dr. Roos Eisma, the anatomy officer at CAHiD, University of Dundee supplied the TEC model for these studies. These studies are used to illustrate the range of uses and benefits the TEC model offers for interventional US research and has also been subjected to external publications (Munirama 2013, Munirama 2015). The Chapter starts with a brief background, followed by two main sections each devoted to an individual case study.

5.2 BACKGROUND

The importance of needle visibility during UGRA was discussed in Chapter Two. What is equally important is the clear differentiation of nerve from the surrounding tissue so as to avoid accidental punctures of the nerve. As seen in Chapter Four, SWE is a useful tool in determining the tissue stiffness and has been widely used for diagnosis and research applications. The first case study assessed the intraneural and extraneural stiffnesses of interscalene, median and sciatic nerve in the TEC model to explore the possibilities of using SWE as the image guidance tool for regional anaesthesia.

An anatomical model similar to human was needed and it was important for anaesthesiologists to receive a similar tactile feedback. The TEC model fulfils these requirements as it is readily available in Dundee, if not elsewhere, and ethical approval for such use was easy to obtain. The SWE system used in the study is the same as described in Chapter Four. It gives quantitative measurements of tissue stiffness in terms of Young's modulus in KPa.

In addition to the ability to identify the nerve from the extraneural tissue using SWE, good visibility of the needle tip and shaft is also critical during UGRA in order to prevent nerve damage (Hocking and Mitchell 2012). Anaesthesiologists prefer IP insertion in most cases as it allows visualisation of most of the needle length though the OP approach is sometimes used for particular cases such as the insertion of perineural catheters (Fredrickson and Danesh-Clough 2013). Ideally, regional block needles should be visible when introduced both IP and OP to the US probe, regardless of angle, depth and needle size (Maecken 2007). So far only a few studies have used TEC models for UGRA research (McLeod 2010, Guo 2012).

The primary objective of the second case study is thus to assess the appearance of anaesthetic needles in the TEC models, in particular assessing the visibility of echogenic Tuohy needles compared to standard non-echogenic Tuohy and echogenic single injection needles. Tuohy needles belong to the group of needles used for epidural anaesthetic blocks for labour pain relief. Chapter Two introduced the issues of needle visibility and IP and OP techniques of needle insertion. Even though epidural blocks have a high success rate, complications have also been reported (Pan 2004). Of many reasons why epidural blocks fail, reduced needle visibility resulting in a dural puncture is reported as a primary cause (Katherine and Scott 2008).

It has been observed that standard non-echogenic needles have increased visibility when inserted at shallow angles IP (Guo 2012); another important parameter influencing the visibility is needle size. Visibility increases in direct proportion to needle size (Schafhalter-Zoppoth 2004). Echogenic needles (Hebard and Hocking 2011), characterised by multiple reflectors on their surface (Figure 37), are associated with better needle visibility.

The study hypothesised that the interaction of needle insertion angle and plane will have an effect on needle visibility of echogenic needles similar to the standard non-echogenic needles, thus affecting the block performance. The secondary objective of this needle study was therefore to compare the properties of an echogenic Tuohy needle, an echogenic single shot needle and a non-echogenic Tuohy needle when inserted at 30°, 45°, 60° and 75° angles, both IP and OP to the US beam in the TEC model. Lateral and bevel views of the

needles are shown in Figure 37. The relation between the needle insertion angle and the needle tip and shaft visibilities were also assessed.

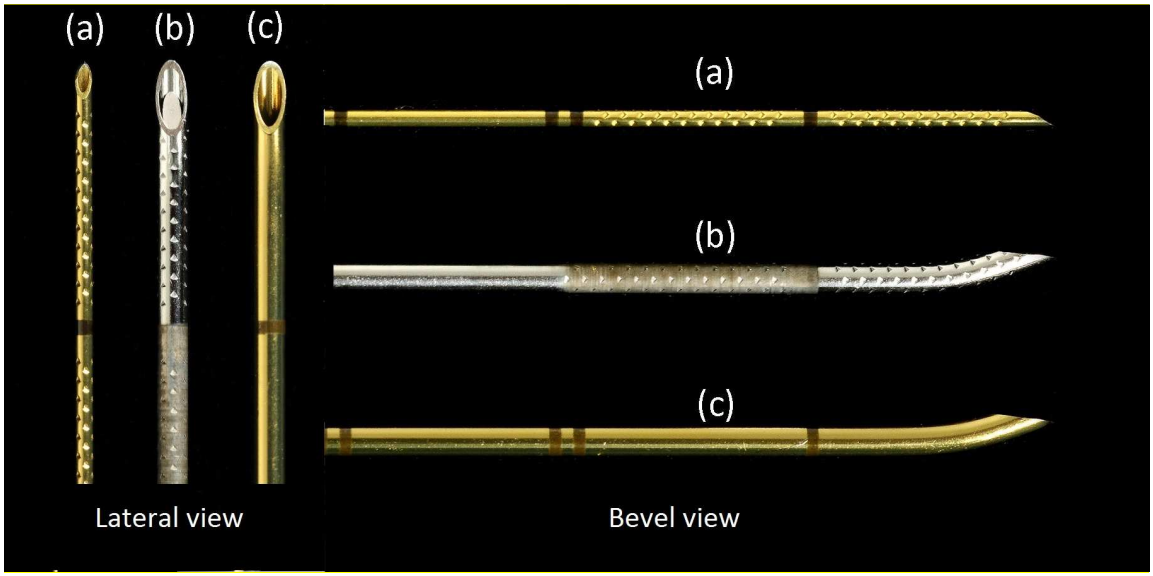

Figure 37: Three needles (Pajunk, Newcastle, UK) assessed during the trial (a) echogenic single injection block needle, (b) echogenic Tuohy needle and (c) standard non-echogenic Tuohy needle; adapted from (Munirama 2015).

5.3 NERVE STIFFNESS ANALYSIS USING ON TEC MODEL

5.3.1 Scanning

TEC scanning was undertaken at CAHiD, University of Dundee, under the supervision of the Anatomy Officer acting under the auspices of the Anatomy Act (Scotland) 2006. An ethical approval from the University of Dundee TEC committee was obtained prior to the study. Young's modulus values of the interscalene, median and sciatic nerves were assessed using the Supersonic Aixploxer SWE US system (Supersonic Imagine, Aixploxer, France). To protect the probe, a long sterile sheath was used. A linear array, 4 - 15 MHz transducer was used to scan the interscalene and median nerves and a curvilinear array, 1 - 6 MHz (3 MHz) transducer for imaging the sciatic nerve. For the interscalene and median nerve scanning, the cadaver was positioned in the supine position, whereas for the sciatic nerve scanning, a prone position was used. Each nerve scan was repeated 10 times and the average stiffness

values in kPa were calculated. Intraneural and extraneural stiffness of the nerves were measured.

.

5.3.2 Results of Nerve Stiffness

The B-mode and corresponding SWE images of the interscalene, median and sciatic nerve in the TEC model are shown in Figure 47, 48 and 49 respectively.

A ROI was selected in the B-mode image corresponding to the nerve and surrounding tissues. The SWE US system displayed stiffness values of the ROI as mean, min, max and standard deviation on the right side on the US image. The ROI selected for this study had 3 mm diameter.

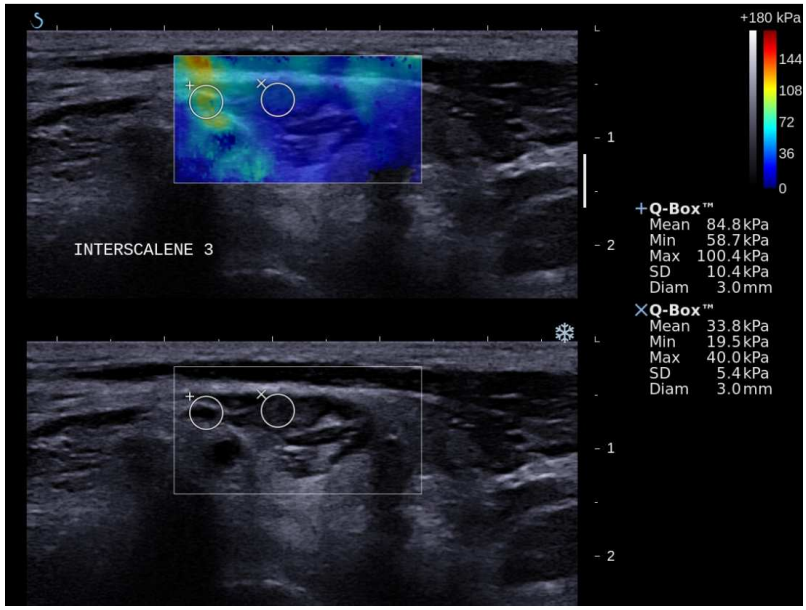

Figure 38: US B-mode and corresponding SWE image of the interscalene nerve.

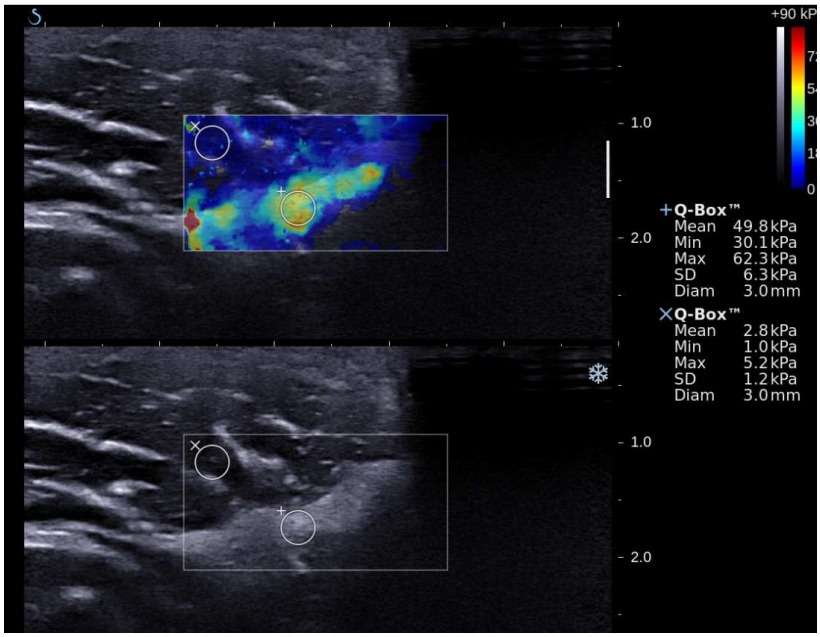

Figure 39: US B-mode and corresponding SWE image of the median nerve.

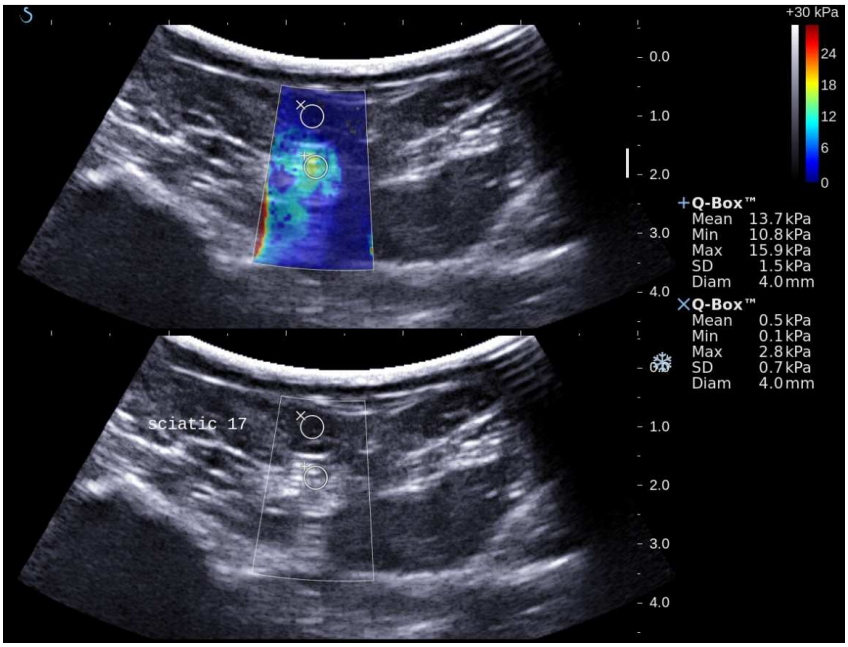

Figure 40: US B-mode and corresponding SWE image of the sciatic nerve.

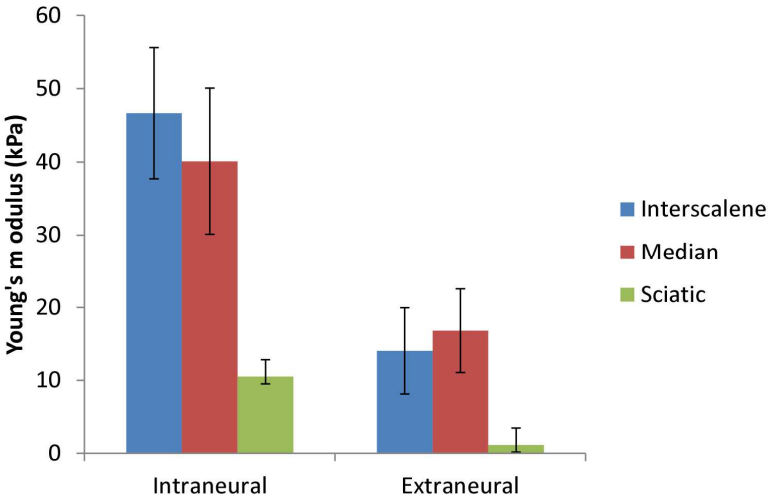

Figure 41: Intraneural and extraneural Young's modulus values of interscalene, median and sciatic nerve.

The results were analysed statistically using the two-sample t-test. The two-sample t-test is applied to compare whether the average difference between the intraneural and extraneural tissue stiffness values are really significant or if it is due instead to random chance. The significance was defined as $p < 0.05$. The results demonstrated that a significant difference exists between the intraneural and extraneural stiffness values in all the three nerves imaged (Figure 41) with $p = 0.00$. The error bars in the figure indicates the standard deviation o the mean stiffness values for all nerves. This finding forms the platform to enable anaesthetists confidently to use SWE system for UGRA. This would not only increase the success rates of the nerve blocks, but also reduce nerve damage and further complications.

5.4 VISIBILITY OF ECHOGENIC TUOHY NEEDLES IN THE US IMAGE

The primary objective of the second case study was to assess the suitability of TEC models in examining needle visibilities. The secondary objective was to analyse the influence of insertion IP and OP to the ultrasound beam and at 30^{o}, 45^{o}, 60^{o} and 75^{o} angles of insertion. The needles under study (Figure 37) were inserted into the deltoid muscle, approximately 3 cm over the biceps. The needle angle was calculated with respect to the US beam.

After obtaining ethical approval from the University of Dundee TEC committee, the study was undertaken at CAHiD, University of Dundee, under the supervision of the Anatomy

Officer acting under the auspices of the Anatomy Act (Scotland) 2006, with a single TEC. US imaging was performed using an 8.5 MHz linear array US probe (Zonare, Mountain View, CA). Covering the US transducer with a long sterile sheath throughout scanning ensured protection of the probe. Video files of needle insertions were initially saved to the scanner hard disk and subsequently transferred to another computer.

Two independent raters used a 5-point Likert score for needle shaft visibility (1 = very poor to 5 = very good). The tip visibility was assessed using a binary outcome (0 = not visible, 1 = visible) as clinical decisions about needle guidance in UGRA are made according to the presence or absence of the needle tip in the image. An engineered, angled, plastic block (Figure 42) was used to guide the needles at particular angles to the TEC. Insertions were made in such a way that all needle bevels directly face the ultrasound beam. No fluid was injected at any time during the trial and the needles were air-filled during insertions. All needles were of 80 mm length. Needle insertion at each angle was repeated 6 times per needle for both IP and OP making a total of 144 insertions (3 needles x 4 angles x 2 planes x 6 repeats).

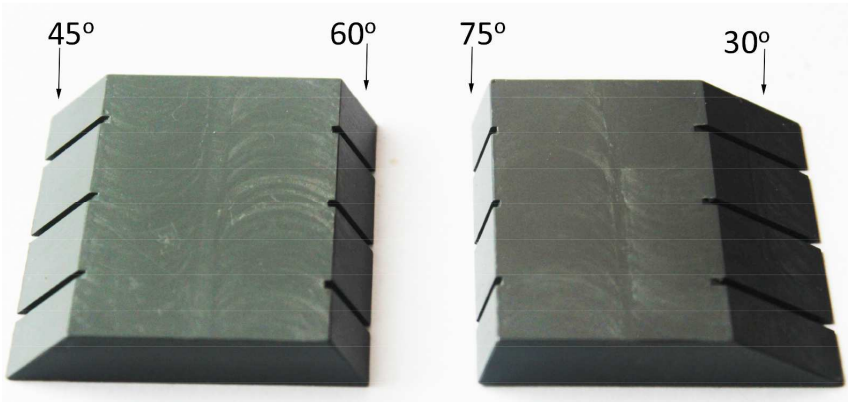

Figure 42: Angled plastic, engineered block used to guide needles at four different angles.

5.4.1 Results

The visibility scores of different needles were recorded and the scores from observers were averaged. US images of TEC models captured during needle insertion, IP at angles 30°, 45° and 60° are shown in Figure 43a, Figure 43b and Figure 43c respectively. The echogenic needles showed higher visibility compared to the non-echogenic needles and the difference

in their shaft and tip visibility scores were demonstrated to be statistically significant. In order to increase the visibility of needles when inserted at deeper angles, a curvilinear probe was used for imaging. Figure 43c shows a curvilinear image, and so the needle angle with respect to the US beam will change at different depths. For the purpose of this study, it was assumed that the differences this would bring to the needle visibility over different depths is negligible and was assumed to have no significant effect on the overall results.

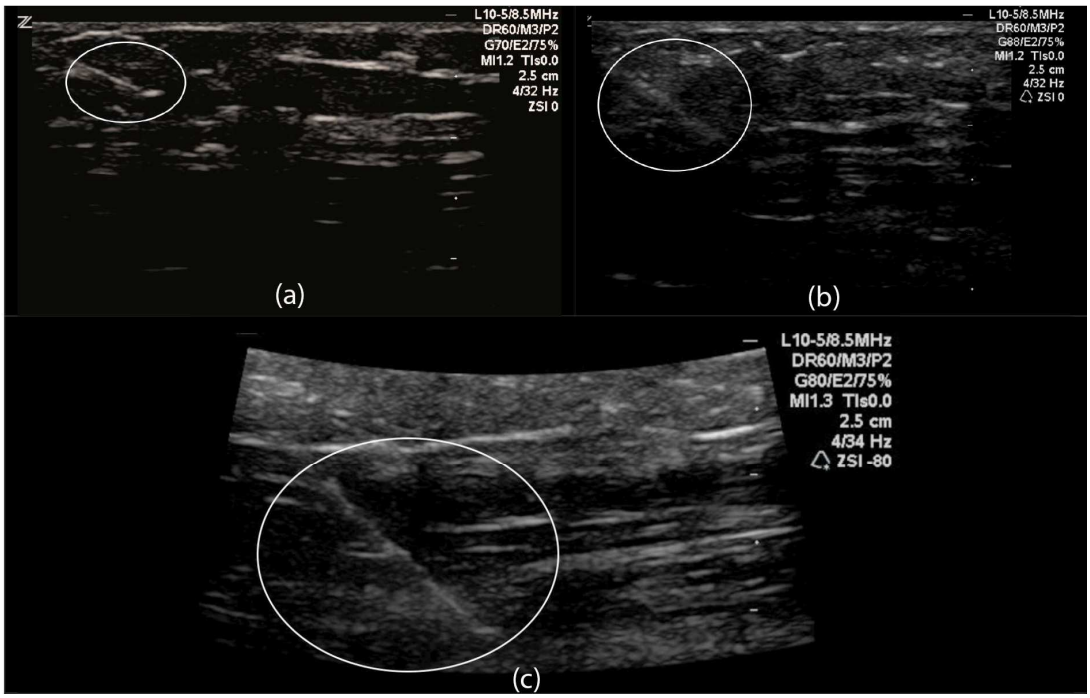

Figure 43: US image captured during the insertion of echogenic Tuohy needle IP at (a) 30°, (b) 45° and (c) 60° to the US beam

The relationships between needle insertion angle and insertion plane with the overall needle visibility were found with respect to the proportions of visible tips and needle shaft visibility scores as shown in Figure 44 and Figure 45 respectively. Figure 44a shows the proportion of visible needle tips (y-axis) against the insertion angle (x-axis) and Figure 44b shows the interaction between the proportion of visible needle tips (y-axis) and insertion planes (x-axis).

Similarly, the interaction of proportion of visible needle shafts to the insertion angle and insertion plane are shown in Figure 45a and Figure 45b respectively. In general, an

improvement in needle tip and shaft visibility were noticed with insertions at smaller angles IP and with larger angles OP. Both echogenic needles showed improved visibility than the standard Tuohy needle when inserted IP and OP to the US transducer. However, in one in four cases, the tips of the echogenic needles were not visible (Munirama 2015).

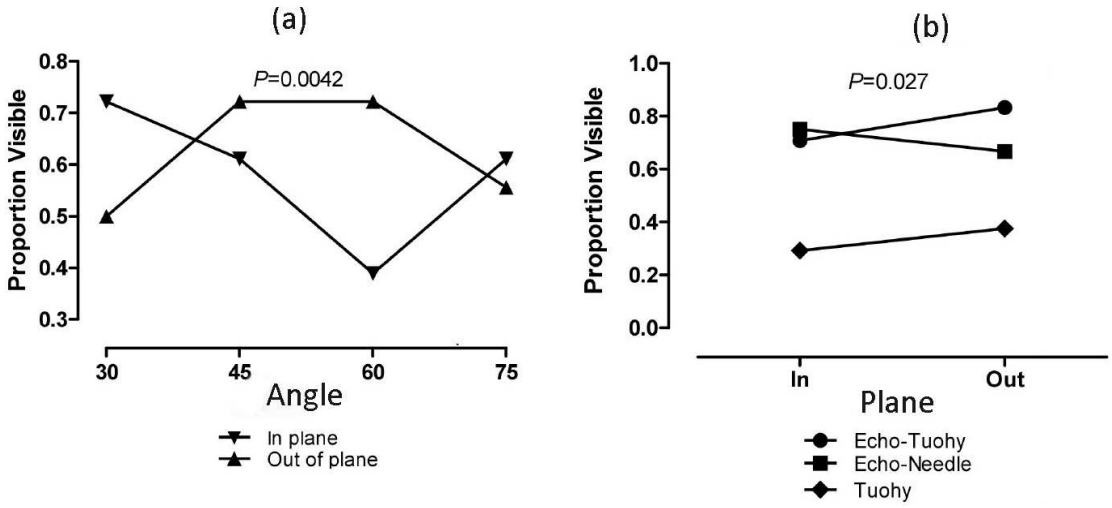

Figure 44: (a) Needle tip: Angle-plane and (b) needle-plane interactions (Munirama 2015).

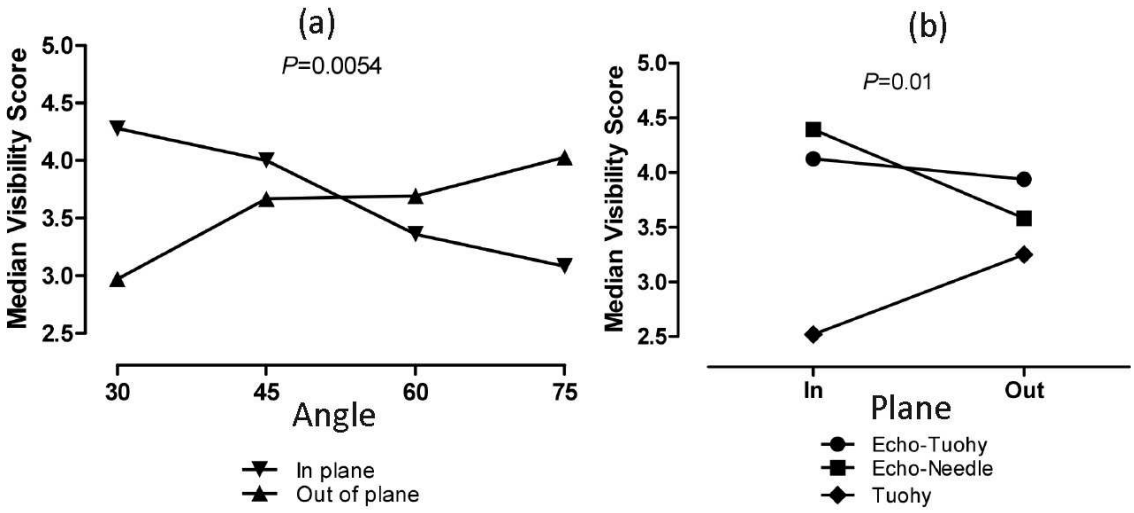

Figure 45: Visibility of needle shafts; angle-plane and needle-plane interactions (Munirama 2015).

Contributions: Joyce J – Conducted the study and assessed the data sets, Munirama S & McLeod- Supervised & helped conducting the study, Roos E – Provided the TEC model for the study, Malachy C – Supervised the statistical analysis.

5.5 DISCUSSION

The SWE nerve imaging study assessed the relative stiffness of the nerve and the extraneural tissue to see if the new SWE technique could be an easier tool to identify nerves. The absolute stiffness values of the nerves and the surrounding structures did not have much importance and so a volunteer study was not necessary to drive necessary conclusions. This study assumed that the intraneural and extraneural tissues were embalmed to the same level and that the any change in stiffness over time would also be uniform in and out of the nerve tissues. However, in the future it will be interesting to conduct a volunteer study to scan the nerve stiffness for a more efficient comparison.

The needle study proved that the echogenic needles have enhanced visibility and this can be explained by their unique design as shown in Figure 37. The circumferentially positioned reflectors on the surfaces of the echogenic needles reflect the US beam back to the transducer unlike the standard non-echogenic needles which reflect the beam widely as seen in Figure 56. Echogenic needles also have a 10 mm gap between the reflector regions (Figure 37), which acts as a scale when seen in the US image. This helps anaesthesiologists to keep track of the needle depth, thus preventing accidental injections.

These two studies demonstrated the use of TEC models for UGRA research. Other tissue models such as small animals and US TMMs are significantly different from humans and could mislead the hypothesis. The US B-mode image in Figure 56 shows a standard non-echogenic needle inserted at 30°, IP to an EPP grey TMM. The image shows clearly the needle shaft and tip in the TMM and the visibility observed with the same needle in TEC model is very different that that seen in Figure 43a. Thus studies in non-anatomical or anatomically different models could produce a false sense of confidence.

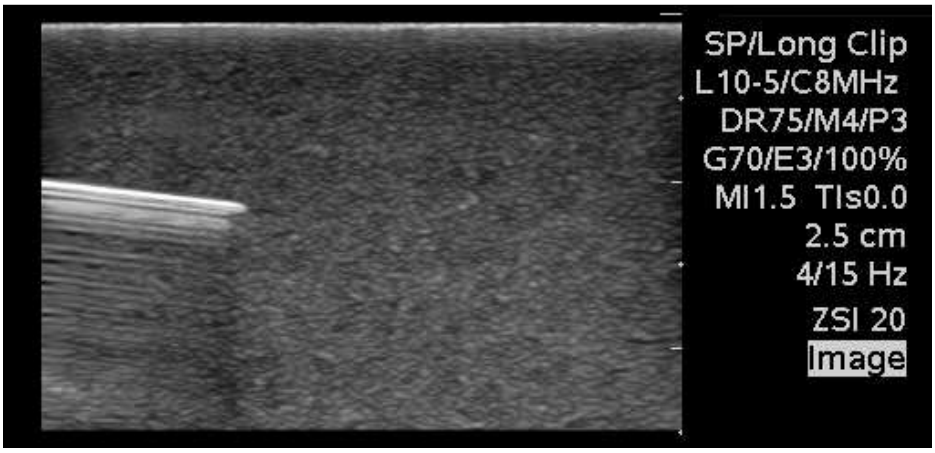

Figure 46: Standard non-echogenic needle inserted IP to EPP grey TMM.

5.6 CONCLUSIONS

This Chapter aimed to explore the uses of TEC models for interventional US, UGRA research. Two case studies explored in this Chapter are good examples to demonstrate the benefits of TEC as tissue simulators for UGRA research. The TEC has proved to be an excellent model for these studies because of their anatomical similarity and tissue feedback compared to live human volunteers.

The reported case studies tried to address needle and nerve visibility concerns in UGRA using TEC models. The nerve imaging study using the SWE US system has demonstrated significant differences between the intraneural and extraneural stiffness in the TEC model. The study thus suggests the use of SWE imaging for needle guidance, thereby increasing the confidence of the anaesthesiologist and reducing complications caused because of nerve damage, hence improving the procedure standards.

The newly introduced echogenic needles were compared against non-echogenic needles in the second study and the interaction between needle shaft and tip visibilities with the insertion angle and plane were statistically assessed. The study demonstrated that the echogenic Tuohy and single injection needles have better shaft and needle visibilities than the standard Tuohy needle in the TEC model. The study concluded that, echogenic needles, irrespective of size, enhanced needle shaft and tip visibilities compared to standard non-echogenic Tuohy needles in the TEC model. However, in one in four cases, the tips of the

textured needles were still not visible. Similar to standard non-echogenic needles, the interaction between needle insertion plane and angle had an effect on the visibility of the echogenic needles.

The work reported denotes the successful use of TEC models for interventional US research. Technical, discrete studies like needle insertion cannot be conducted on human volunteers for ethical reasons. The TEC model was found to be extremely beneficial for these studies. In contrast to homogeneous US phantoms, TEC provided a characteristic US image, anatomically similar to living humans.

CHAPTER 6

Thiel-embalmed Human Breast Tissue for Therapeutic Ultrasound

6.1 INTRODUCTION

This Chapter considers the suitability of TEC breast tissue as a model for therapeutic US breast cancer research. Chapter Two introduced HIFU and MRgFUS as specific methods for non-invasive surgery. The technique has widely been used for treating uterine fibroids and prostate cancer (Wu 2007). However, because of the proximity of lesions to the ribs or overlying skin in the case breast cancer, HIFU can cause painful overheating or skin burns, respectively. An additional technical problem in the application of FUS to breast lesions is the frequent presence of large amounts of fat surrounding the tissue to be treated, which can hinder MRI monitoring of the local tissue temperature and thus interfere with assessment of the adequacy of the procedure.

Recent developments in FUS have introduced novel US transducers specially designed for use with breast lesions (Payne 2012, Payne 2013). These systems surround the breast and allow application of FUS radially, thus improving the range of breast lesions that can be safely treated with reduced risk of side effects. However, to support the evaluation of such transducers applied to patients in clinical trials, there is a need to establish the efficacy and the accuracy of temperature monitoring of FUS with MRI, particularly in the fatty breast. This requires an appropriate anatomical model that imposes similar physical constraints to the normal or cancerous breast and responds to FUS in the same way. The work described in this Chapter explored the use of TEC breast tissue for this purpose. The main objectives of the study are as follows:

a. To design and develop an MRI compatible HIFU chamber for conducting US sonications under MR guidance.

b. To determine the differences between TEC breast tissue and fresh *ex-vivo* human breast tissue sonications in terms of focal temperatures.

c. To assess differences in temperature measurements between the use of a temperature probe and the MRI proton resonance frequency shift (PRFS) method.

6.2 BACKGROUND

6.2.1 Breast Cancer & Breast Cancer Therapy

Breast cancer is the commonest cancer in women in the UK, accounting for 30% of all new cancers in women, with an estimated 49,900 new cases in 2011, i.e. more than 130 every day (Cancer-Research-UK 2011). The lifetime risk of developing breast cancer is 1 in 8 for women in the UK. The Independent Breast Screening Review in the UK mentions growing public and scientific concern about over-diagnosis and over-treatment of certain screen-detected cancers (IBSR 2012). Nearly 20% of all cancers diagnosed through the screening programme will not cause harm during the woman's lifetime. However, it is currently impossible to prospectively identify cancers requiring no treatment and hence there is an urgent unmet clinical need to develop minimally invasive breast- specific treatment for small low risk tumours.

The breast mainly consists of milk-producing glands surrounded by layers of connective tissue and fat. The glands consist of lobules that branch out and are connected to the nipple by small epithelial-lined channels called lactiferous ducts. The lobules are supported by the surrounding fatty tissue, which is composed of fat or adipose tissue, connective tissue, and ligaments. The lobules and ducts are together referred to as fibroglandular tissue. Breast cancer originates in the fibroglandular tissue and, depending on where it develops, there are two main types: ductal carcinoma and lobular carcinoma.

Several therapy options are available for breast cancer treatment and are specifically selected depending on the stage of the disease. The treatments include breast-conserving surgery, mastectomy, radiation therapy, chemotherapy and endocrine therapy. During the later stages of breast cancer, surgical treatments like breast-conserving surgery and mastectomy may be preceded by chemotherapy (so-called neoadjuvant chemotherapy) to increase the likelihood of breast-conserving surgery. The local recurrence rate is also reduced by post radiation therapy and endocrine treatment post-surgery. However, complications and side effects of these treatment methods have been reported (Angelique and Newman 2007).

As described in Chapter Two, over the last two decades MRgFUS has become a widely accepted non-invasive tumour ablation therapy. MRI has proved to be an efficient option for planning and monitoring the treatment during tissue ablation because of its ability to permit thermal mapping, unlike other imaging modalities (Karakitsios 2014). The most significant benefit is its ability to produce real-time temperature maps during interventions. MRgFUS is used worldwide to treat liver, brain, bone, uterine fibroids and prostate cancers and it is currently used in a few countries for treating breast cancer including China, Japan, Germany and the USA (Wu 2007, Li and Wu 2013). Figure 47 shows an MRgFUS system used for treating breast cancer.

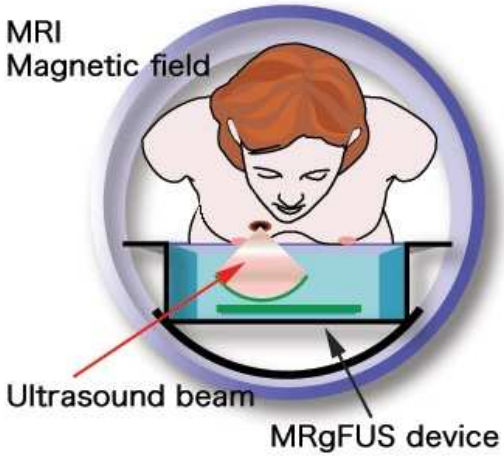

Figure 47: MRgFUS system used for breast cancer (Namba 2014).

6.2.2 PRF Thermometry and Errors with Fatty Tissue

MR thermometry based on the PRFS was introduced in 1966 (Hindman 1966) and relates to the temperature sensitivity of the PRF. When a molecule is exposed to a magnetic field, the resonance frequency of its nucleus, ω is related to the magnetic field as shown in Equation 18.

$$\omega = B_0 * \gamma(1 - s) \tag{18}$$

where

B_o is the magnetic field strength.

γ is the gyromagnetic ratio.

s is the shielding constant and depends on the chemical environment (Ishihara 1995).

On heating up water molecules, a shift in ω results due to the rupture, stretching or bending of the hydrogen bonds. PRF based thermometry calculates the temperature distribution by measuring this PRFS (Karakitsios 2014) using Equation 19.

$$\Delta T = T - T_{ref} = \frac{\phi(T) - \phi(T_{ref})}{\alpha\gamma T_E \mathrm{B}_0} \tag{19}$$

where

$\phi(T)$ is the measured phase.

$\phi(T_{ref})$ is the phase from the reference image.

α is the PRF change coefficient.

γ is the gyromagnetic ratio.

T_E is the echo time.

B_o is the magnetic field strength.

Molecules such as lipids or N-acetyl-aspartate in the brain have constant, temperature-independent PRFS which are used as reference peaks to measure the PRF shift of water molecules with increasing temperature (Rieke and Butts Pauly 2008). PRF thermometry has proved to be a reliable and accurate tool for real-time temperature mapping (Poorter 1995, Bruno 2000). PRF thermometry, combined with MRgFUS procedures, has been reported to be accurate in predicting thermal coagulation in both *ex-vivo* and *in-vivo* animal experiments and in human studies (Graham 1999, Quesson 2010).

While the PRFS method is an effective temperature measurement technique in tissues such as muscle which are mostly water, there can be significant errors in regions containing even small amounts of adipose tissue or fat (Hindman 1966). This is because of the reduced

hydrogen bonds in fat, making its phase variation with temperature negligible. Many biological tissues are composed of both water and fat (Poorter 1995), so there will be some phase change due to temperature.

Because of this, it is still possible to calculate a phase sensitivity value using the phase changes observed, but with errors in the measurements. In addition to the temperature measurement errors in fat, notwithstanding recent developments of ring transducers, many transducers used in ablating tissue in the MRgFUS systems are not specifically designed for treating tumours in superficial organs like the breast, resulting in complications such as skin burns and overheating of rib cage (Furusawa 2007), as noted previously.

6.3 MATERIALS AND METHODS

Novel FUS systems are now being developed specifically for treating breast tumours. Payne et al (2013) report development of such a breast specific MRgFUS system, with the study using a goat udder model for testing, though the group has reported this as not ideal as a model for human breast. Because of the similarities of TEC to healthy tissue, as seen with tissue stiffness analysis in Chapter Four and from the needle guidance study in Chapter Five, TEC human breast tissue was analysed for its feasibility to be a more suitable model than *in-vivo* animal breast tissue for human breast FUS research and transducer testing.

Anatomical similarity and the presence of surrounding fat matches healthy human breast tissue. This part of the thesis describes the sonication of TEC human breast samples under MRI guidance and monitoring of the temperature during this process using two methods: an external MRI compatible temperature probe and MRI PRF based thermometry. The sonications are compared with the results from sonicating fresh human breast samples obtained from prophylactic mastectomy. The study consisted of three main sessions and the materials and methods used in each stage are reported in the following sub-sections.

6.3.1 Laboratory Based Sonications in a MRI Compatible HIFU Chamber of Fresh Animal and Embalmed TEC Breast Tissue.

An MRI compatible HIFU chamber was designed with Solidworks computer-aided design software (Figure 48a) and fabricated (Figure 48b) in the lab using a 3D printer. The material used to make the chamber was acryonitrile butadine styrene [ABS] plastic. All parts used in the chamber were plastic and glass to ensure the MRI compatibility. The step by step procedure in developing the chamber are given in Appendix II. A tissue holder was also designed and built as shown in Figure 48c.

The sides of the tissue holder were made with US transparent Mylar film of 0.075 mm thickness (PSG Group Ltd, London, UK). After building the chamber and the tissue holder, they were taken to the MRI room, near the magnet to ensure their MR compatibility. It was found that they were safe to be used in the MRI. An MRI compatible HIFU bowl transducer (1.09 MHz, 69 mm focal length), developed during another doctoral project (Qiu 2014) was used in the chamber for delivering US energy. The efficiency of the transducer was tested using an impedance analyser (Model number: 4396B, Agilent) and was found to be 72%.

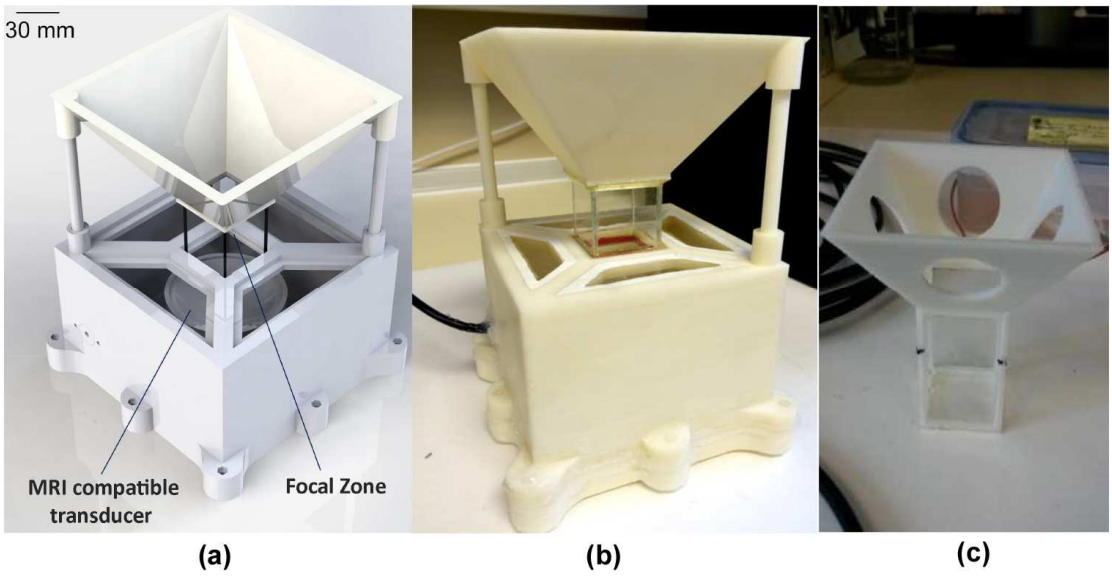

Figure 48: MRI compatible HIFU chamber (a) designed and (b) developed. (c) Tissue holder

The field mapping of the US transducer (1.09 MHz) in the chamber was done using a needle hydrophone with active area, 1 mm (1.0 mm probe, Precision Acoustics Ltd, UK). The experimental set-up and acoustic pressure map are shown in Figure 60a and b respectively.

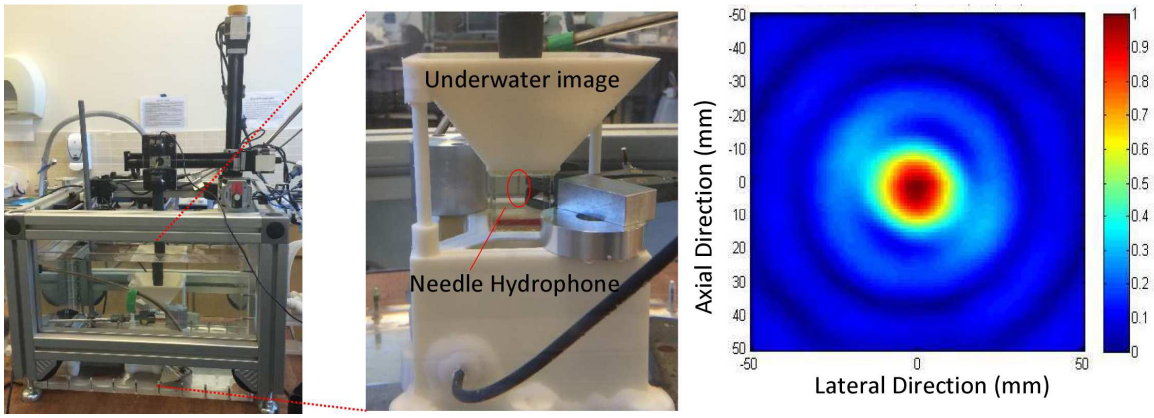

Figure 49: (a) Measuring the pressure in the focal region of the FUS chamber with a needle hydrophone, (b) Pressure map in and around the US focus.

The chamber was tested first using fresh chicken breast *ex-vivo* and the experimental set-up is shown in Figure 61. The power amplifier used for the experiment was an ENI 3100LA radio frequency power amplifier and it provides up to 100 W of linear power with low harmonic and intermodulation distortion. The device has an operational frequency range of 250 KHz to 150 MHz and a nominal gain of 55 dB ± 1.5 dB.

The temperature probe was inserted to the sample and was positioned at the focal zone using distance calculations. The tissue holder was designed in such a way that the focus of the chamber is 2 cm deep from the midpoint of the tissue holder surface. Markings were made in the temperature probe to match these distances and the probe was carefully inserted into the sample. Extra care was taken during the insertion to prevent any bending of the sensor as this might result in a slanting position of the tip of the sensor resulting in erroneous measurements. Once the temperature probe is inserted to the focal zone, a fast US scan was conducted to ensure its location.

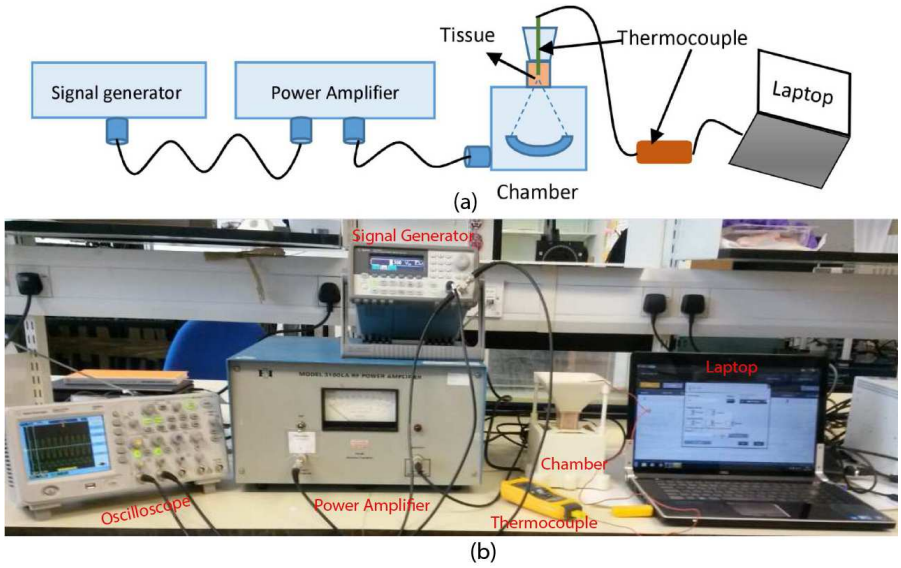

Figure 50: Lab-based HIFU experimental set-up (a) schematic and (b) image.

6.3.2 MRI Guided Sonications of *Ex-vivo* Tissue Using the Chamber

After successful testing of the chamber in the lab, the experiments were conducted using animal and human *ex-vivo* samples under MRI guidance. MRI was used to image the chamber and the sample to ensure correct placement of the temperature probe tip. The TEC breast sample used for the experiments were provided by CAHiD at University of Dundee. US and a mammography unit were used to image the whole embalmed cadaveric breast after dissection from the cadaver before samples were excised from it for experimentations. Figure 51a and Figure 51b show the images obtained from the US and mammography imaging respectively. Afterwards, a rectangular block of breast tissue, measuring 4 cm ˣ 6 cm was carefully dissected from the high Body Mass Index (BMI) and predominantly fatty whole breast sample without damaging the skin.

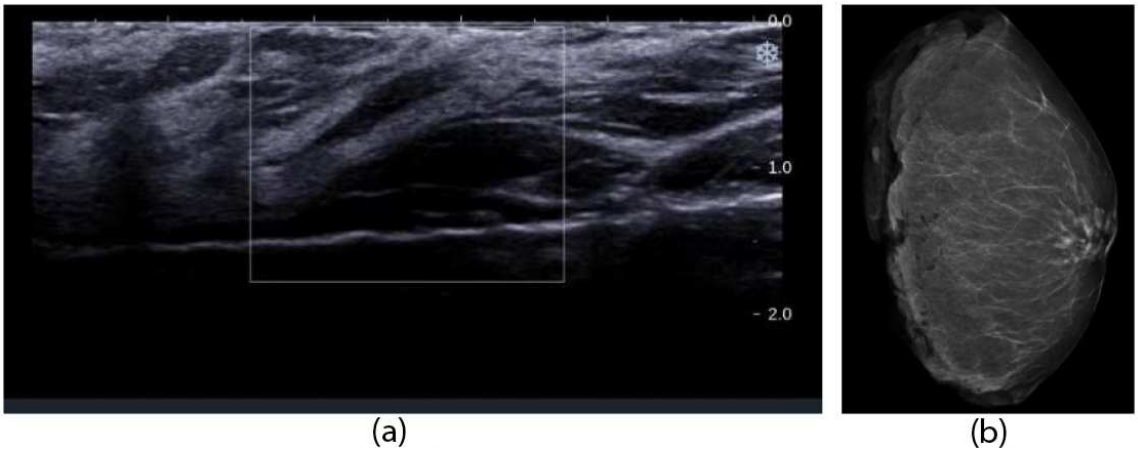

Figure 51: a) US image of the whole soft-embalmed human breast. b) X-Ray image of the predominantly fatty whole soft-embalmed human breast.

To explore the effects of embalming on the production of visible lesions during FUS, other *ex-vivo* tissues, including fresh chicken breast and porcine belly, were also embalmed, with the embalming process shown in Figure 52, in this case with chicken breast samples. Chicken breast was chosen to represent muscle and porcine belly as a better proxy for breast as it has both muscle and fat layers.

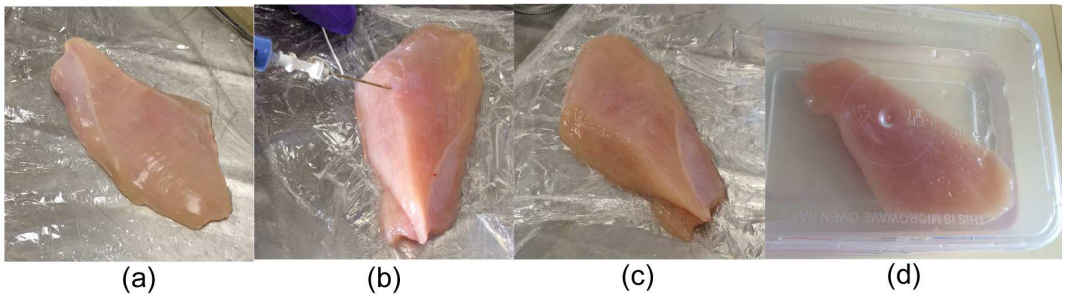

Figure 52: Chicken breast tissue embalming process. (a) Tissue before embalming, (b) Injecting embalming fluids, (c) Tissue after injection, (d) Tissue immersed in TEC tank fluid after injection of embalming fluids. (Weights of sample before and after embalming were 68 g and 82 g respectively).

The chamber was placed in a 1.5 T MRI (GE Medical systems, USA) as shown in Figure 53. The coil used for imaging is an 8-channel interventional coil consisting of two 24 cm square paddles (DuoFLEX Coil Suite, GE Medical Systems, USA). Reference temperature data were collected using an MRI compatible temperature probe (Model : FOTEMP1, Optocon Optical

Sensors and Systems, Germany). Before experiments were conducted, temperature probe was calibrated using the 'one point calibration' method noted in the FOTEMP1 user manual (Optocon 2010) to ensure that the temperatures displayed were the real temperatures.

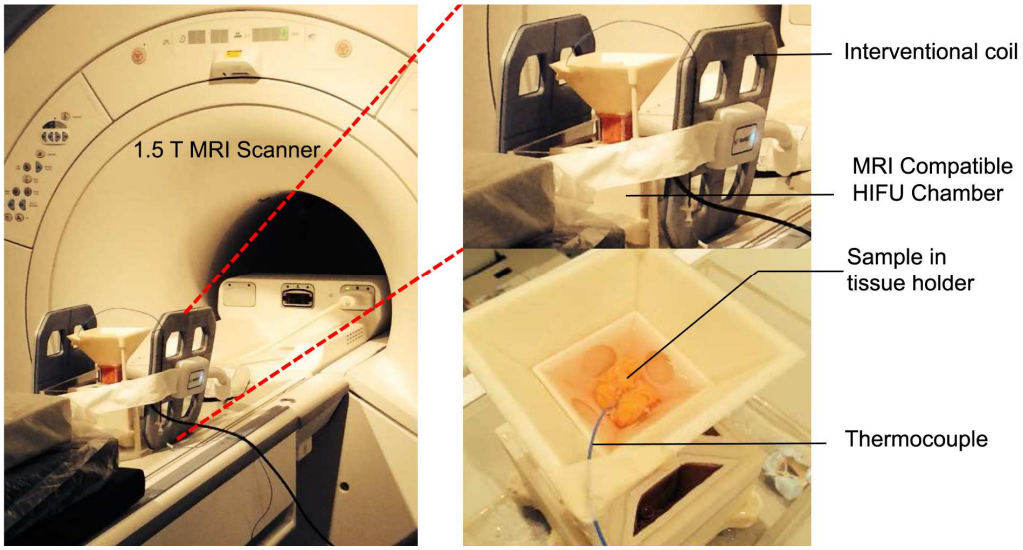

Figure 53: Set-up showing the chamber in the MRI scanner before sonication

6.3.3 MRI Guided Sonication Using Exablate

The MRI guided sonication results using the 1.09 MHz transducer (Qiu 2014) built into the chamber and the temperature probe-measured temperature data were compared with sonications performed with the commercial Insightec Exablate system and the temperature readings with those acquired using MRI thermometry. The set-up schematic and images are shown in Figure 54. The tissue holder containing the sample and degassed water was carefully placed on top of a gel pad (Insightec Ltd, Israel) ensuring no air bubbles were trapped between the layers. The gel pad was placed in a cylindrical container with a Mylar layer as the bottom surface, making it US transparent (Figure 54a). The container with the tissue holder and sample was then placed on the Exablate Mylar platform (Figure 54b) and degassed water was used for coupling between the Mylar layers.

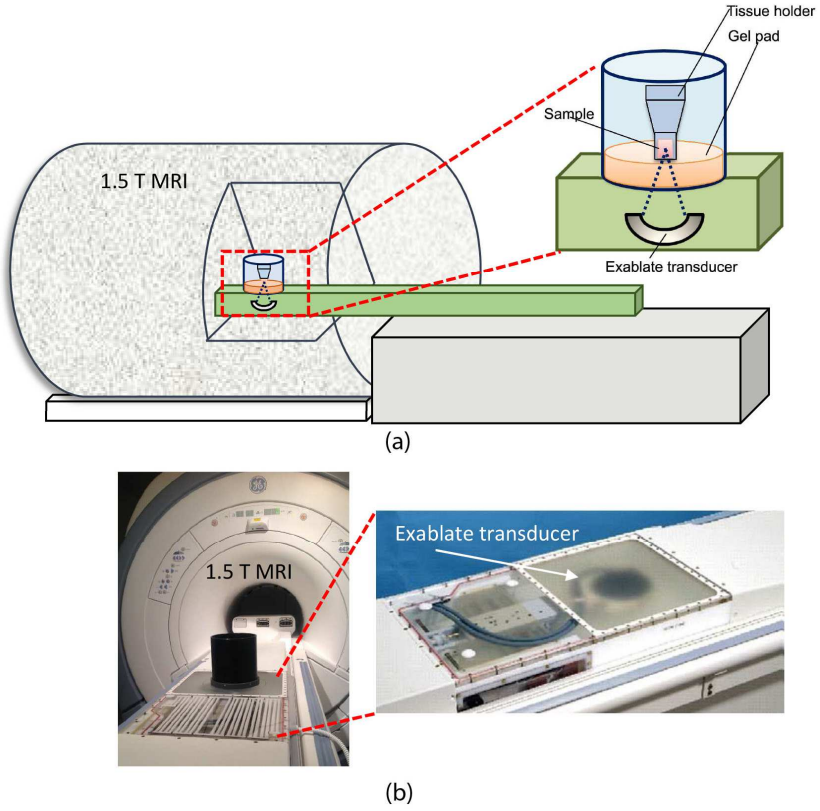

Figure 54: (a) Schematic representing the set-up during Exablate sonications and (b) Picture of the set – up with closer view of the US array and positioning system mounted in the MRI scanner table of the first commercial MRgFUS system (Exablate 2000, Insightec, Haifa, Israel).

6.3.4 Histology

Apart from checking for visible lesions after sonicating the samples, the samples were also analysed for any histological changes post-sonication, with the tissues fixed and embedded in wax using the paraffin technique (Histology-guide 2015). Fixing the tissues used 4% formaldehyde solution. This process hardens the tissue, making the slicing of the sample easier. It also kills any bacteria, inactivates enzymes and enhances staining. Fixed samples undergo dehydration and clearing processes where the water content in the sample is replaced by xylene. The fixed samples are then sliced into thin sections, as seen in Figure 55, and embedded in paraffin wax.

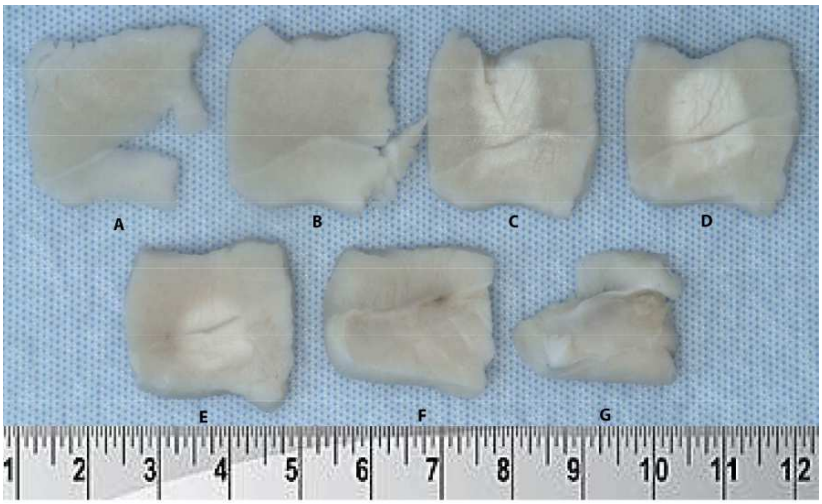

Figure 55: Formalin fixed section of previously fresh sonicated chicken breast samples.

Thin sections of the paraffin-embedded sample were obtained using a microtome, then stained using haematoxylin & eosin (H & E) (Histology-guide 2015) for microscopic examination, as shown in Figure 56. H & E staining is the most commonly used staining and is used to give contrast to the whole cells. The specific purpose of this staining is hence to make cells visible for human eye by adding contrast.

Figure 56: H&E stained slices of sonicated fresh chicken breast samples.

6.4 RESULTS

This results section is divided into three main parts. The first sub-section presents the results from the lab-based testing of the MRI compatible chamber. The results from TEC

breast sonications in the chamber under MRI guidance are given in the second sub-section. The third sub-section presents the results from sonications using the commercial Exablate MRgFUS therapy delivery system (Figure 54).

6.4.1 Testing the Chamber

The initial testing of the chamber was conducted by sonicating fresh chicken breast and porcine belly samples. Fresh *ex-vivo* samples were brought to room temperature and sonications were carried out at output acoustic power of 40 W, 50 W and 60 W for durations of 60 s. The output power values were Power values were specifically selected to ensure sufficient temperature rises to produce clearly visible lesions. Temperature readings acquired using the temperature probe were logged every second and saved to the computer, providing the graph shown in

Figure 57a. Each sonication was repeated three times to analyse repeatability.

Figure 57b shows temperature readings from repeated sonications at 50 W.

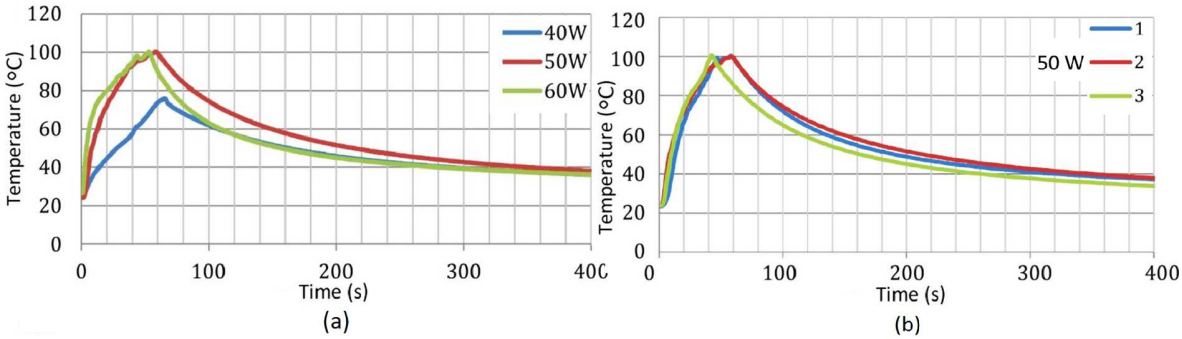

Figure 57: (a) Sonication temperatures at 40 W, 50 W and 60 W power in fresh ex-vivo chicken breast sample and (b) temperatures for repeated sonications at 50 W power in chicken breast samples for 60 s (Sonication start time – 0 s and stopping time – 60 s).

Sonications produced visible lesions in both the chicken breast and porcine belly *ex-vivo* samples and the size of the lesions increased with power, as expected. Figure 58 shows lesions formed in fresh chicken breast samples during sonications.

Figure 58: Ex-vivo fresh chicken breast lesions as a result of sonications at (a) 40 W, (b) 50 W and (c) 60 W for 60 s.

6.4.2 MRI Guided Sonications of *Ex-vivo* Samples in the Chamber

After successful testing of the chamber, experiments were conducted using TEC breast tissue and fresh *ex-vivo* human breast tissue under the guidance of MRI (Figure 54). MRI guidance was used to ensure the correct position of the temperature probe tip before starting the sonications. MRI axial and coronal images of the chamber with samples in the tissue holder are shown in Figure 59. The figures show the position of the temperature probe tip in both the axial and coronal planes.

Figure 59: (a) Axial and (b) coronal images of the chamber with the sample in the tissue holder. Crosses mark the position of the temperature probe.

TEC breast samples were sonicated under 40 W, 50 W and 60 W powers for a duration of 60 s. The TEC breast sample before and after sonication is shown in Figure 60. No visible lesion was seen in the sonicated TEC breast sample upon dissection. The sonicated breast tissue, which was largely fatty, as shown by mammography and US of the specimen in Figure 51, was examined histopathologically, confirming the absence of any discrete lesion. However, a layer of melted fat was formed on top of the water after sonication (Figure 60c). The temperature rise during sonications are shown in Figure 61.

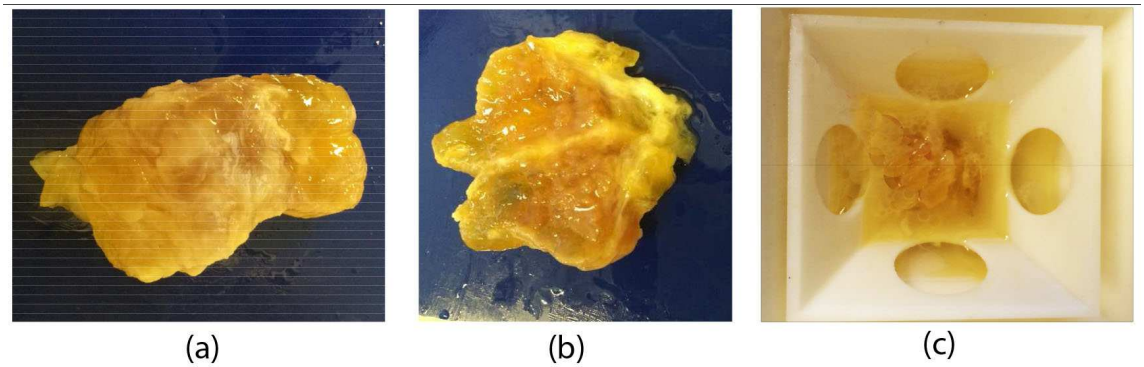

Figure 60: TEC breast sample (a) before and (b) dissected sample after sonication. (c) The layer of melted fat floating in the water post-sonication.

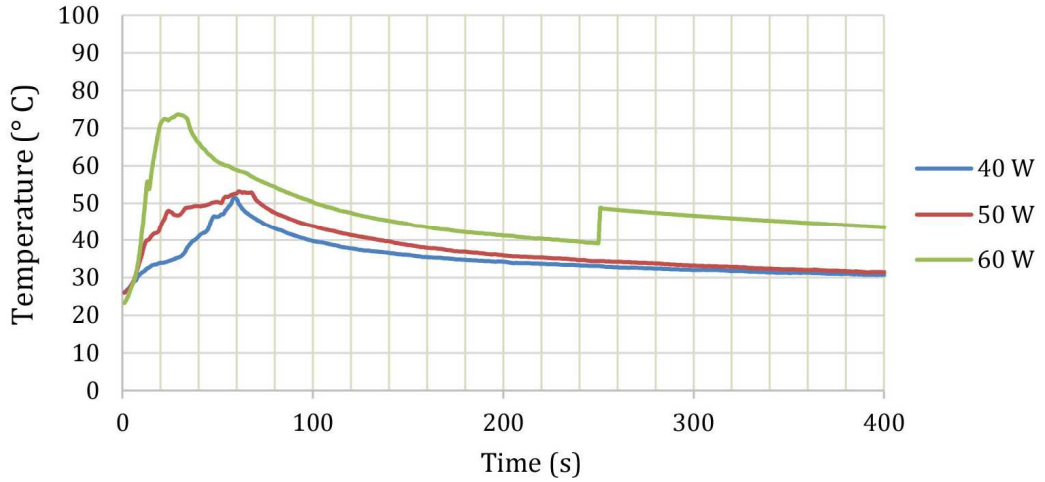

Figure 61: Thiel human breast sonication temperature graphs at different power. (Sonication start time – 0 s and sonication stop time – 60 s).

Fluctuations in the temperature readings were observed during the higher power sonication process and, unlike the fresh chicken samples in Figure 68, the temperature started to decrease before sonication was stopped at higher power. Further rises at later stages of recording after stopping the sonications (as seen at 250 s for the 60 W sonication in Figure 61) were also noticed at higher powers. This may be explained by the fact that the TEC breast tissue samples utilised were primarily made of adipose tissue and heating the tissue resulted in the fat melting in the focal region of the FUS field, causing the temperature probe tip to change its position. This effect was significant at higher powers because of the increased melting of fat. The melted fat was visible and floated on top of the tissue after sonications. However, similar to the fresh chicken breast tissue, the temperatures increased with power.

After receiving ethical approval from Tayside Tissue Bank, fresh human breast *ex-vivo* samples were collected from prophylactic mastectomy (Figure 62a). The tissue was imaged using mammography prior to doing experiments to ensure that the dissected sample was not pathologically significant. Any pathologically significant samples had to be returned to the tissue bank without using them for research purposes. The sonications were carried out under MRI guidance at a power of 50 W for a duration of 60 s to compare the results with the TEC breast sonications. Because of the restrictions in obtaining multiple samples from surgery and the rarity of prophylactic mastectomy surgeries, it was not possible to conduct repeated sonications with fresh human *ex-vivo* samples.

The temperature map during sonication is shown in Figure 62b. Similar to the observations in the TEC breast sample sonications, the temperature graph during fresh *ex-vivo* breast sample sonications also showed fluctuations. Even though the duration of sonication was set to be 60 s to match the Thiel breast sample experiments, a temperature rise up to 132°C was recorded within 10 s of starting the sonication. Hence, the sonication was stopped after 10 s and the temperatures started to drop soon after, until 40 s after the stop time, when a further rise was noticed from 88 to 96 °C. Again, this may be because of temperature probe tip displacement due to the melting of adipose tissue.

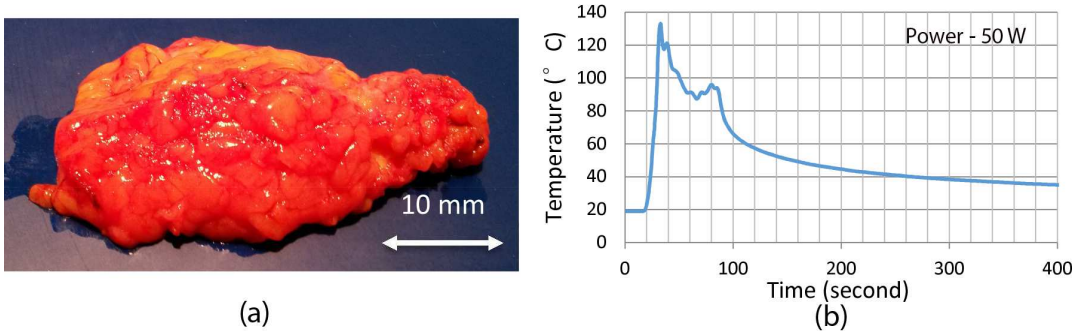

Figure 62: (a) Fresh human breast ex-vivo specimen collected after mastectomy and (b) temperature map during sonications (Power - 50 W).

The sonicated sample was immediately transferred to 4% formaldehyde solution before sending it for histology analysis. As it was important to keep the sample whole for the histology analysis, the sonicated sample was not dissected to inspect for the presence of any lesion visually. However, slices of the sample made during the histology analysis showed visible differences between sonicated and non-sonicated regions as shown in Figure 63.

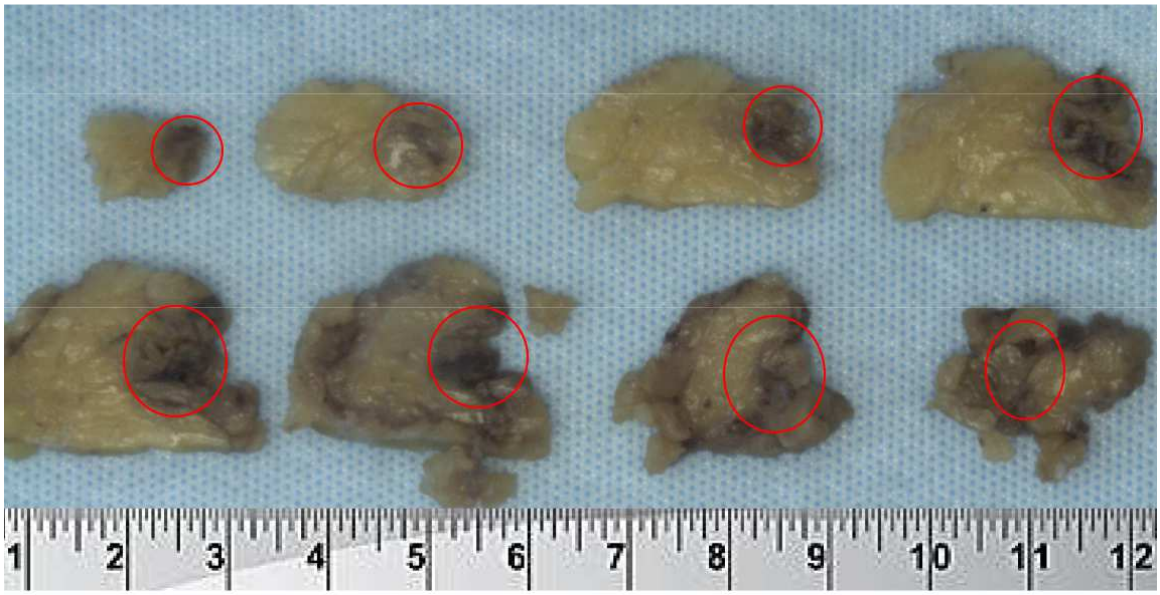

Figure 63: Slices of formalin fixed (previously fresh) human breast ex-vivo samples and clearly visible sonicated regions in the slices. Sonicated regions are marked in red circles.

It was observed that the temperature rise in the TEC tissue was lower and slow when compared to fresh *ex-vivo* human breast tissue sonicated at the same power, as shown by

comparison of Figure 61 and Figure 62. This was further investigated by calculating the US attenuation coefficient of TEC breast sample using Equation 10 and the set-up shown in Figure 16c in Chapter Three. The US attenuation coefficient of TEC breast sample was measured to be 0.0063 ± 0.0001 $dB.cm^{-1}.MHz^{-1}$. This is at the low end of the range of US attenuation coefficients of *in-vivo* human breast tissue in the literature, 0.075 ± 0.0001 $dB.cm^{-1}.MHz^{-1}$ (Culjat 2010), also given in

Table 1.

The significant decrease in the US attenuation between the TEC breast tissue and *in-vivo* human breast tissue may be because of the higher water content in the former. Theoretically, this should decrease the US absorption in the TEC sample, thus preventing higher temperature rises as measured in the fresh *ex-vivo* human breast tissue. The lack of visible lesions may be explained by the fact that, the thermal ablation of tissue with HIFU causes denaturation of proteins, one of the many effects of soft-embalming is also the same (Holzle 2012). To investigate further, the experiments were repeated with soft-embalmed chicken breast tissue to test the hypothesis that no visible HIFU lesions form because proteins are already denatured in soft-embalmed tissue.

6.4.3 Sonicating Soft-Embalmed Chicken Breast Tissue

Soft-embalming of fresh *ex-vivo* chicken breast followed the same procedure as for the embalming, shown in Figure 63. The embalmed chicken breast tissue before and after sonications and the temperature graphs for sonication at different power levels in the Thiel-embalmed chicken breast sample are shown in Figure 64.

As with the TEC breast tissue sonications, these experiments did not result in any visible lesions in the sonicated region. However, the temperature rise was substantially higher at higher power levels than that of TEC breast tissue. This may be because of the decreased or no fat content in the *ex-vivo* chicken breast samples when compared to the TEC breast tissue.

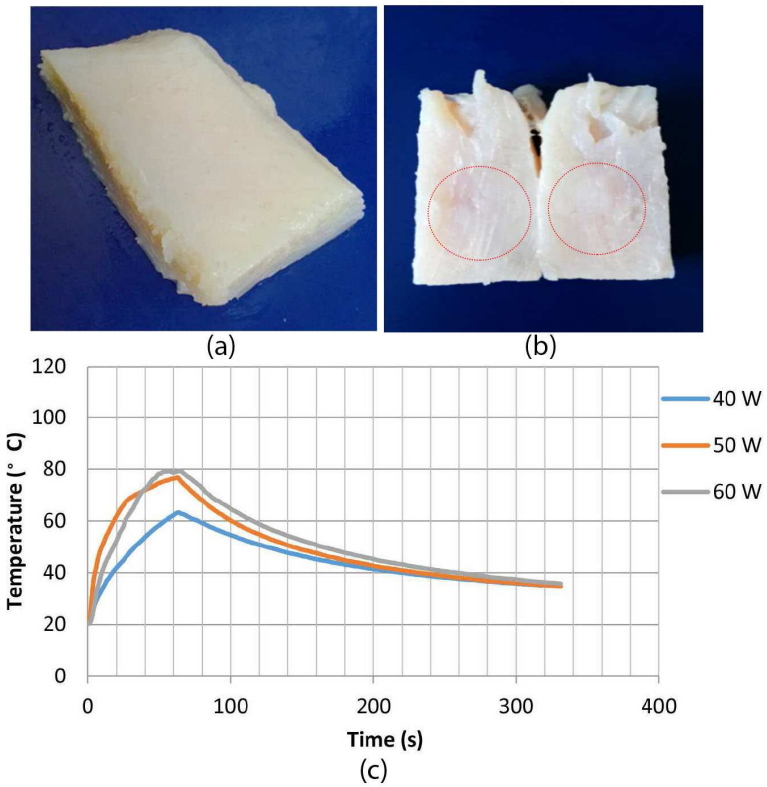

Figure 64: Soft-embalmed chicken breast tissue (a) before and (b) after sonications. (c) Graph showing the temperatures during sonications at different powers. (Sonication start time – 0 s and sonication stop time – 60 s). Sonicated region marked in red circles shows no visible lesions.

6.4.4 Sonications Using MRI Guided FUS Exablate System

The initial sonication in the chamber under MRI guidance for positioning the temperature probe acquired temperature measurements in the sonicated region for both embalmed and fresh *ex-vivo* samples, as shown in previous sections. However, one of the aims of this work was to determine possible errors in MRI thermometry while sonicating adipose tissue. Having collected temperature measurements using an external temperature probe, it was important to conduct the same experiments in a clinical setting and measure the temperature reading using MRI PRFS thermometry. A control experiment was initially conducted by using degassed water in the tissue holder and comparing the temperature data measured using the thermocouple and the MR PRF thermometry. The control

experiments indicated errors less than 0.45 ± 0.13% between the two readings when repeated 3 times.

The schematic of the experimental set-up is shown in Figure 54. The resultant of MR image of the TEC human breast sample is shown in Figure 65. The sample is in the tissue holder used for the chamber experiments and is placed over a gel bed and coupled to the Exablate transducer using a cylindrical container with an US transparent Mylar base. The tissue holder containing the sample was filled with degassed water.

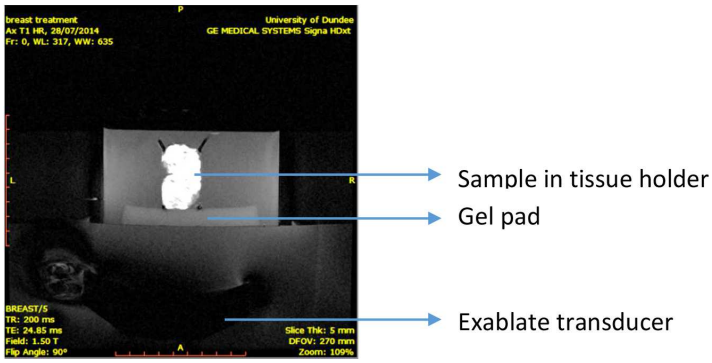

Figure 65: Sample arranged in the tissue holder in the Exablate system.

A screen shot of the Exablate treatment planning window is shown in Figure 66, with the area of sonication pre-selected to be in the centre of the tissue. The sonications were conducted at 40, 50 and 60 W for durations of 60 s to match the experiments with the TEC breast tissue in the bespoke chamber. Temperature graphs of the sonications can be seen at the bottom-right corner of Figure 82: the green line represents the average temperature over the nine pixels surrounding and including the selected pixel, and the red line is the temperature at the selected pixel.Sonication at each power was repeated twice using different samples dissected from the same TEC breast. Tissue was brought to room temperature (25°C) before sonication to ensure uniform heating for different samples and, after each sonication, the degassed water used for acoustic coupling was replaced and a different tissue sample was placed in the tissue holder. Table 11 shows the average temperatures recorded using both the MRI PRFS method and the temperature probe. Each measurement shown is an average of two repeated measurements.

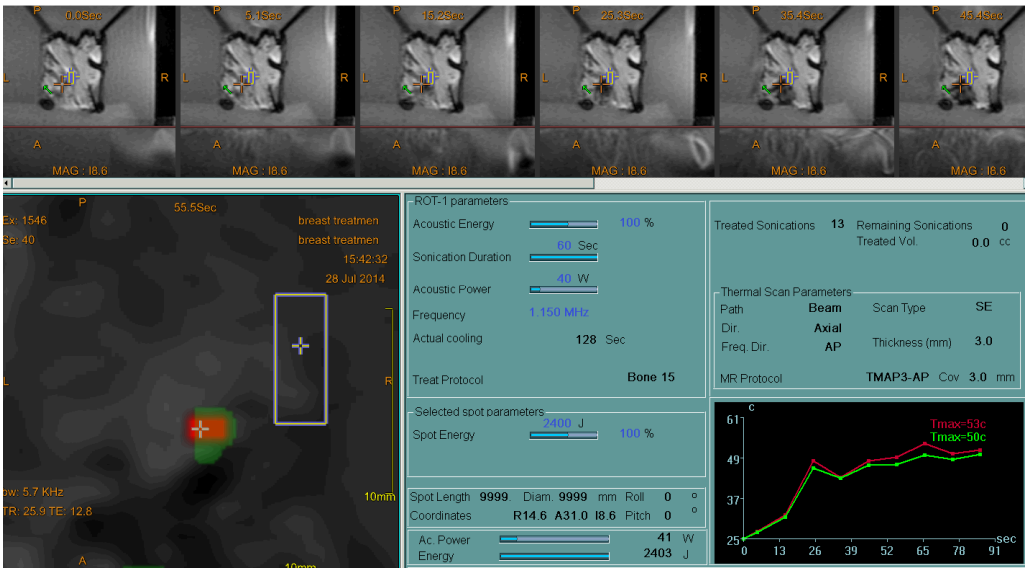

Figure 66: Exablate treatment planning window with measured temperatures shown bottom-right.

Table 11: Temperature readings measured using temperature probe and MRI PRFS method.

Power	MRI PRFS Method (°C)	Thermocouple (°C)	Difference %
40 W	51.5 ± 1.5	50.2 ± 1	2.5 %
50 W	54.5 ± 2.5	56.6 ± 3.4	3.76 %
60 W	66 ± 1	71.9 ± 1.7	8.59 %

Table 11 shows differences which increased significantly with increased power. This might be because of the errors in PRFS thermometry with the adipose tissue. This was further investigated by sonicating fresh *ex-vivo* chicken breast and porcine pure fat samples using Exablate and using both the MRI PRFS method and temperature probe to measure the temperature differences at a power of 50 W for a duration of 60 s. The results showed differences between the temperature data measured using the both methods in porcine fat samples (Percentage error – 19.5%) and the data acquired using the both methods in fresh chicken breast samples agreed with each other (Percentage error – 1.8%)(Figure 67). This

confirms that the errors in thermometry in measuring temperatures in fat is the primary reason for the differences observed in Table 11.

The higher differences in temperature data in Table 11 can also be considered due to the thermocouple tip changing location due to more fat liquefactions at higher powers. However, it is most likely a measure of MR PRF thermometry errors due to heterogeneous heating of adipose tissue. Even if the thermocouple moves due to fat liquefaction, if it is showing high temperatures which the MR cannot detect, then it is clearly shows the errors in PRF thermometry whilst measuring temperatures in fatty tissue. Heterogeneous heating (marked in red circle) can also observed that during the sonication of porcine fat samples, as shown by the screen shot of Exablate treatment map in Figure 68. Figure 68 concludes the key results from this chapter.

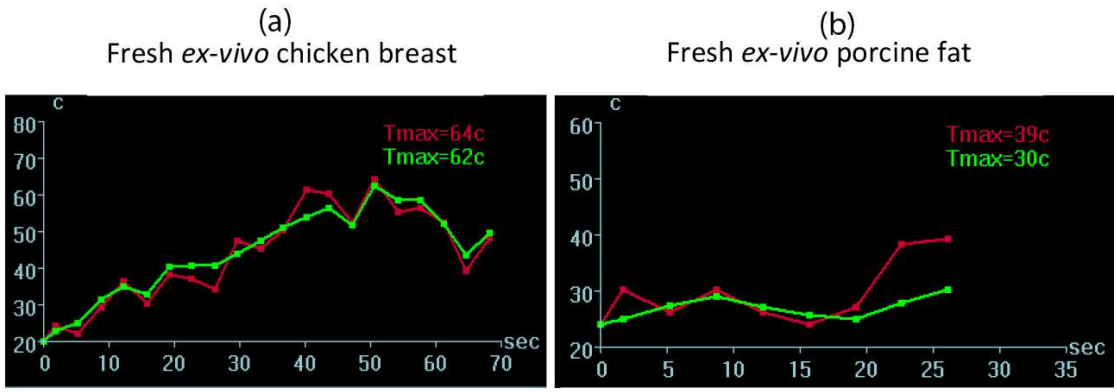

Figure 67: Temperatures measured using MR PRFS method thermometry during sonication of fresh ex-vivo (a) chicken breast (pure muscle) and (b) porcine pure fat samples.

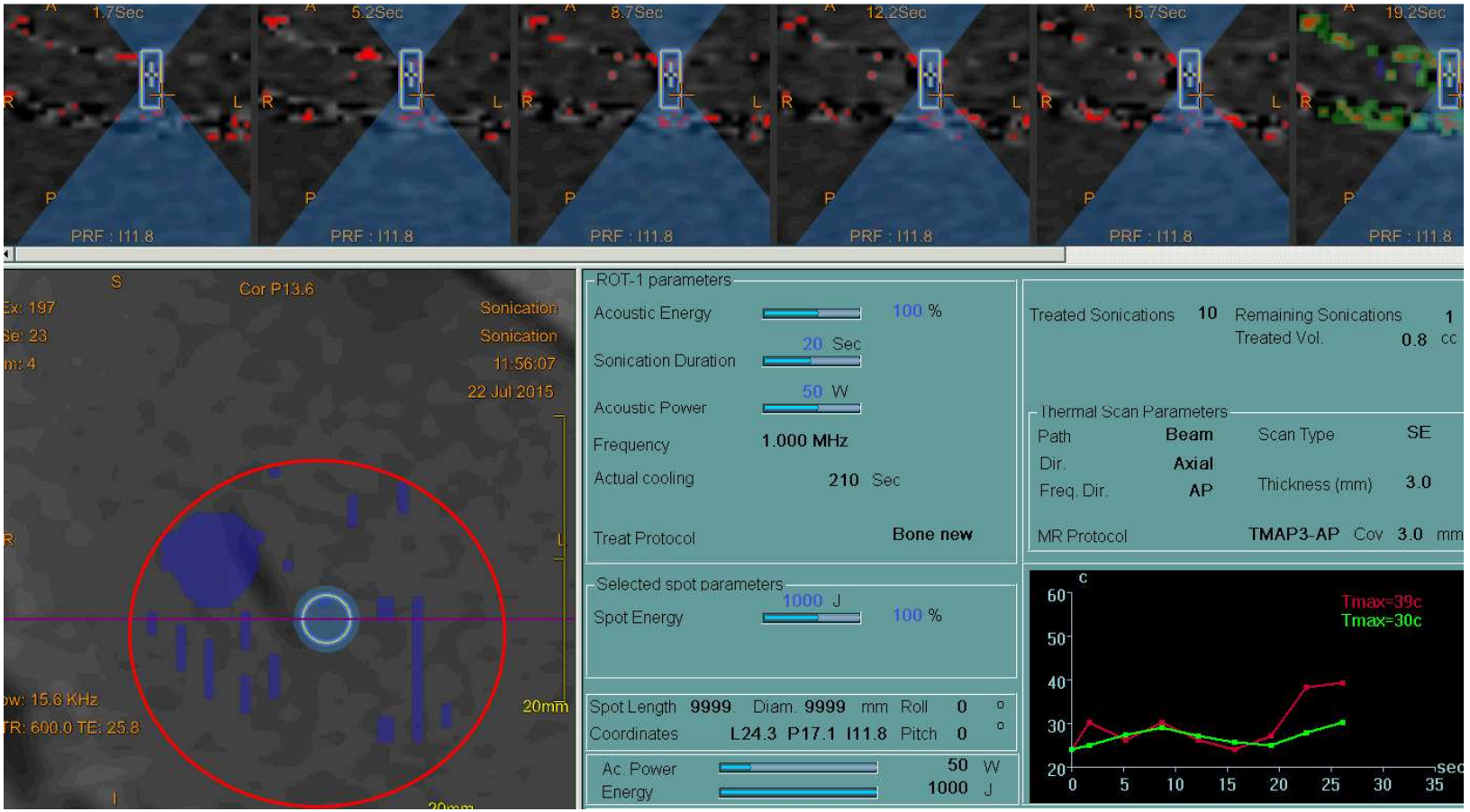

Figure 68: Exablate screen shot obtained after the sonication of porcine fat samples.

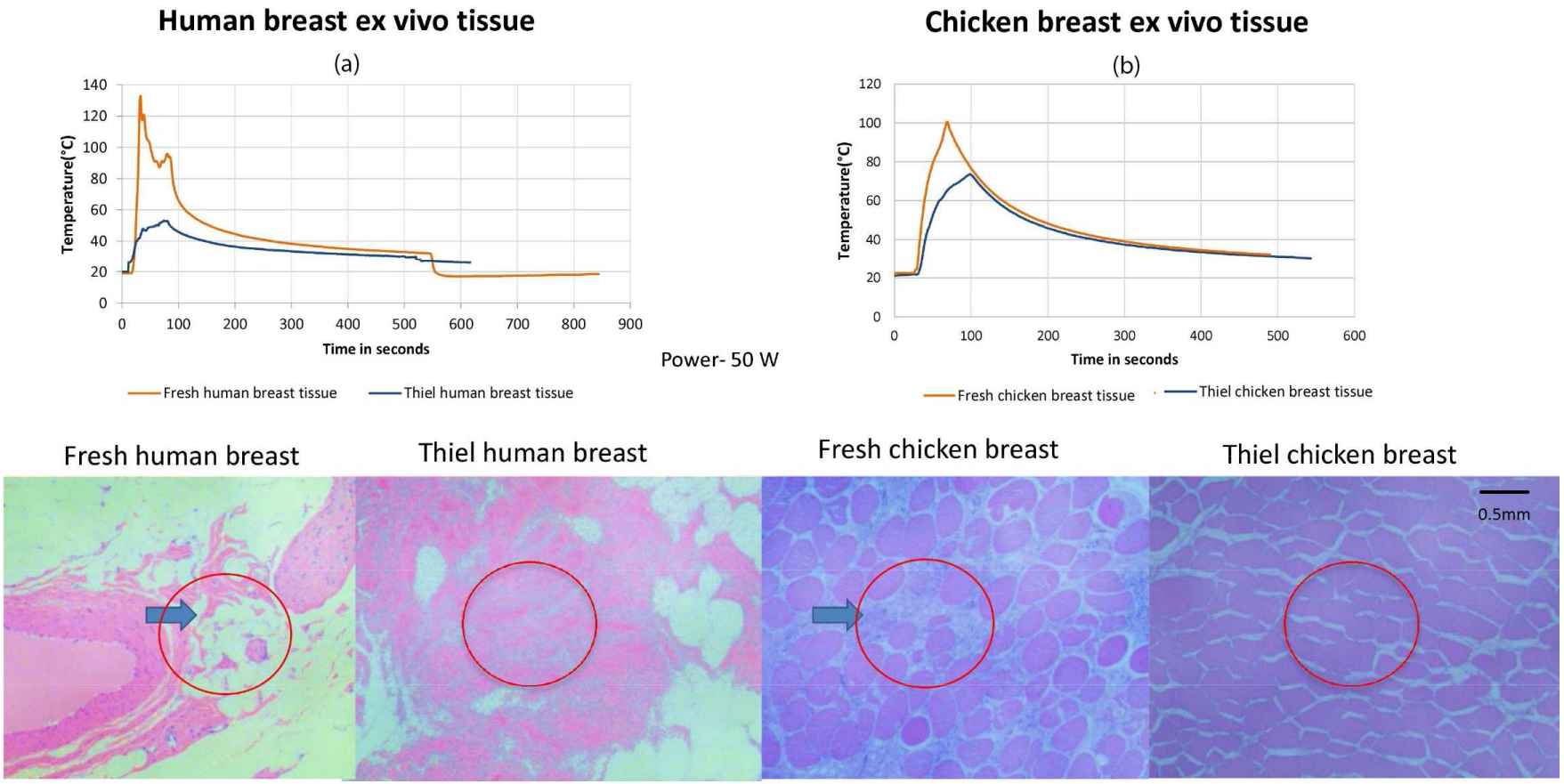

Figure 69: Differences in temperature rise between fresh and embalmed ex-vivo samples of (a) human breast tissue and (b) chicken breast tissue. The red circles denotes some breakage of bonds in the region of sonication.

Figure 69 shows the corresponding temperature differences, measured using temperature probes and histological images of human breast *ex-vivo* and chicken breast *ex-vivo* samples in both fresh and embalmed tissues. It has to be noted that chicken 'breast' tissue does not bear any resemblance to human breast tissue as is composed of pure muscle tissue (protein) with very little fat.

Figure 69 is not intended to compare chicken breast sonications with TEC human breast sonications, but the effects of sonications in TEC is compared with that of fresh human fatty breast tissue. Sonication effects on muscles is given by showing the fresh and embalmed chicken breast samples. The histological images clearly show the sonicated regions in fresh human and chicken breast sonications. The red circled region shows the breakage of bonds within the sonicated region. However, there no significant changes were seen between the sonicated and non-sonicated regions in soft-embalmed human and chicken breast samples. TEC breast tissue behaved differently from fresh *ex-vivo* human breast tissue in terms of its lower attenuation coefficient resulting in lower peak temperatures and the sample also failed to produce any visible lesion.

6.5 DISCUSSIONS AND CONCLUSIONS

This Chapter aimed to assess the suitability of TEC breast tissue as a model for therapeutic breast HIFU pre-clinical research. As previously stated in the introduction of this Chapter, the main objectives of the study were to design and develop and MRI compatible HIFU chamber and to determine the differences between TEC breast tissue and fresh *ex-vivo* human breast tissue. The study also aimed to assess the differences in temperature measurements between the use of a temperature probe and MRI PRFS method. An MRI compatible chamber was designed and developed for the HIFU studies.

Unlike with fresh *ex-vivo* animal breast samples, the sonications of TEC breast tissue failed to produce any visible lesions. Denaturation of the tissues is one among the many effects of the Thiel embalming salt solution and this is the most likely reason that no visible lesions were produced during heating, as heating also denatures the tissue. Even though the Thiel salt solution denatures the tissue, this effect is caused due to the presence of chemicals in

the embalming solution and is different from the denaturation caused by the heating during FUS. The absence of lesion while sonicating embalmed samples were later confirmed by sonicating embalmed chicken breast samples. The sonicated sample was histopathologically analysed to confirm this finding, as shown in Figure 69.

While comparing the TEC breast sonications with sonication of fresh *ex-vivo* human breast tissue, it was observed that, at the same power, the heating of TEC tissue was much lower. This was further investigated by measuring the attenuation coefficient of TEC breast tissue, which, at 0.0063 $dB.cm^{-1}.MHz^{-1}$, is lower than the attenuation coefficient of *in-vivo* human breast tissue, 0.075 $dB.cm^{-1}.MHz^{-1}$. To understand further, the attenuation coefficient of fresh *ex-vivo* human breast tissue has to be calculated as the work presented here compares TEC breast tissue with *ex-vivo* human breast mastectomy specimens.

As explained earlier, this has not been possible due to the rarity of prophylactic mastectomies. It has thus been assumed that there is no significant changes in the US attenuation coefficient in fresh *ex-vivo* human breast tissue as the experiments were conducted within two hours of surgery. The low figure for TEC breast tissue may be caused by the presence of large amounts of water-based embalming fluid, making the values of attenuation coefficient close to that of water (0.002 $dB.cm^{-1}.MHz^{-1}$). Since, Thiel tissue is denatured, the consequent reduction in microstructure may relate to the lower levels of attenuation.

As mentioned in the background section of this Chapter, MRI PRFS methods of measuring temperatures shows errors in fatty tissue. In order to use this method in pre-clinical trials, it was important to consider the differences in the readings between the MRI PRFS method and real-time temperature probe measurements.

Experiments were repeated with the Exablate commercial system using the same power and sonication duration. It was observed that there are differences between the peak temperatures at the same power and the percentage difference increased at higher powers. Because of the reduced hydrogen bonds in fat, the phase variation with temperature is negligible and at higher powers, melting of more fat makes these phase changes almost

absent, resulting in higher percentage errors. Temperature comparison experiments were repeated using fresh *ex-vivo* chicken breast samples and the measured temperature using both methods showed good agreement.

To summarise,

1. Sonicating TEC fatty breast specimen did not produce a visible lesion and is unlikely to be a good model for *in-vivo* human breast tissue for pre-clinical trials.

2. The pre-existing denaturation in the embalmed tissues, made it not possible to see lesions even during the histology examinations.

3. Issues with the MR thermometry in measuring fatty tissues was investigated using a predominantly fatty TEC breast tissue, deliberately selected to model the most difficult situation during breast HIFU clinical trials.

The MRI PRFS temperature measurement method showed differences from the temperature probe readings and this suggests the need for more accurate (probably invasive) means of temperature measurements such as using temperature probes during pre-clinical trials for breast cancer research. Though clinically MRgFUS is likely in sonicating breast cancer, the problems might arise in measuring temperatures in the margin of tumour, especially in fatty tissue as seen by the errors in the temperature measurement of *ex-vivo* fatty embalmed human breast and fresh *ex-vivo* porcine fat samples. Search for an ideal model for *in-vivo* human breast tissue is continuing.

CHAPTER 7

Thiel mice for Microultrasound

7.1 INTRODUCTION & MOTIVATION

This Chapter is dedicated to demonstrating the possibilities of using Thiel-embalmed mice as an easily accessible US model for high frequency systems testing. As seen in the earlier Chapters, the TEC model derives benefits from being anatomically the same as humans and the case studies presented in Chapters Five and Six have demonstrated some of the ways in which the TEC model may be considered for US research. However, one of the main drawbacks of a TEC model compared to artificial US phantoms is its reduced accessibility. Only a few places globally have Thiel embalming facilities and that limits its use. Even at research institutes that have TEC models, sometimes it is useful to have an anatomical model that is cost effective, easier to handle and readily accessible.

Live small animal models are the most commonly used *in-vivo* models for clinical research. However, for development of imaging applications such as in µUS, where an anatomical model is highly preferable for testing, a live model is not a necessity. Literature shows the use of fresh dead or frozen mice during the initial stages of research (Fu 2013). However, fresh or frozen dead mice carry an infection risk and are not reusable as their tissue properties change over time. Thiel mice, introduced in this Chapter suit applications where a small, *ex-vivo* anatomical model is needed. In addition to being readily available, reusable and easier to handle due to their small size, they are cheaper to access and no ethical approval is needed for their use. They may also contribute towards reducing the number of live mice used for medical research, assisting the goal of the three R's, replacement, reduction and refinement, in animal testing. One of the primary advantages of having a Thiel mice model is its reusability. The same mice can be re-used and this will allow comparing the development of systems over time.

This Chapter presents the embalming techniques for preserving mice. The embalmed mice organs are imaged using high frequency US imaging systems and compared with live mice images. Later in the Chapter, two case studies demonstrate the use of Thiel mice as tissue models in high resolution imaging systems development.

7.2 THIEL EMBALMING OF MICE

Thiel embalming of human cadavers is an established method in the literature (Thiel 1992a, Thiel 1992b, Thiel 2002). The work discussed in this Chapter optimises the Thiel embalming technique for embalming small animal models such as mice. Embalmed mice are also tested using high frequency US, MRI and OCE imaging systems, thus assessing their use for testing μUS systems.

7.2.1 Embalming Protocols

Thiel embalming of mice has not been done before and there is no information available on any changes in concentrations of chemicals used for enabling the correct preservation for imaging purposes. Because of their smaller size, concentrations of fluids needed for successful embalming may differ from use in humans and hence, with the help of the CAHiD Anatomy Officer, six different protocols (Table 12) were developed and used on one mouse each, with a total of six mice embalmed. Embalming Fluid 1, the arterial fluid, is normally infused into the femoral artery and embalming fluid 2, the venous fluid, is normally injected into the superior sagittal sinus with the intent that it reaches the internal organs faster.

The expectation is that muscle compartments receive mostly arterial fluid while internal organs receive a mix of both. Literature suggests that venous fluid can be added to the arterial fluid up to a ratio of 1:1 (beyond which the muscles become too stiff in humans)(Thiel 1992a). After injecting arterial and venal fluids, the mice were immersed in the Thiel tank fluid. The constituents of the arterial, venous and tank fluids used for the Thiel embalming are given in Chapter Four, Table 6.

The proportion of arterial and venous fluids for different protocols are shown in Table 12. The immersion fluid used in all the six embalming protocols are the same, the Thiel tank fluid. Generally, a 60 kg body needs about 15 - 20 L of arterial and venous fluid combined. For immersion, the amount of tank fluid is calculated as approximately four times the body weight. The actual process of mouse embalming was kept the same as for the human but with lesser amounts of fluids and a shorter embalming period.

Table 12: Thiel mice embalming protocols

Number	Embalming fluid 1 (A) - Arterial Fluid Embalming Fluid 2 (V) - Venous Fluid	Immersion fluid
SET 1	Arterial fluid – Torso compartments Arterial fluid – Muscles	Thiel tank fluid
SET 2	Arterial + Venous fluid (2:1) – Torso compartments Arterial fluid– Muscles	Thiel tank fluid
SET 3	Arterial +Venous fluid (1:1) – Torso compartments Arterial fluid–muscles compartments	Thiel tank fluid
SET 4*	Arterial +Venous fluid (1:2) - Torso compartments Arterial fluid – Muscles	Thiel tank fluid
SET 5	Venous fluid - Torso compartments Arterial fluid - Muscles	Thiel tank fluid
SET 6	Arterial fluid - Torso compartments Venous fluid - Muscles	Thiel Tank fluid

** This is the same protocol used for embalming human cadavers using the Thiel method*

7.2.2 Sample Preparation

Six wild type mice (3 males, 3 females; Age – 189 ± 67 days; Weight: 22g ± 6 g) were embalmed within 30 minutes after death using the protocols defined in Table 12. The mice before and after embalming are shown in Figure 70a and Figure 70b respectively. As the

skin of mice is delicate compared to human skin, the hair on the mice was kept intact while embalming as there were chances that the skin would break if it came in direct contact with the fluid.

Figure 70: (a) Six wild type mice before injection the embalming fluids, (b) Male (Set V) and female (Set I) mice immersed in the tank fluid after injecting the embalming fluids.

The time period suggested in the literature for human cadaver preservation is four months (Thiel 1992a, Thiel 1992b, Thiel 2002, Wolff 2008). Because of the significant weight difference between human and mice, only few weeks of immersion was considered necessary for the mouse model. However, to ensure proper embalming, the embalmed mice (Figure 71) were first scanned four months after the embalming date. About three weeks after the immersion date, the hair fell off the mice leaving nude skin afterwards. A mouse embalmed using the Set IV protocol, four months after its embalming date, is shown in Figure 71. After four months, all six mice appeared the same. However, some changes to the appearance of the skin were noticed after 2.5 years of the embalming date (Figure 78).

Figure 71: Embalmed mouse after 4 months of immersion (Set IV)

7.3 IMAGING SOFT-EMBALMED THIEL MICE

7.3.1 Imaging the mice with the Visual Sonics VEVO 770

US imaging of all six mice was carried out using the facilities of Edinburgh Pre-clinical Imaging, College of Medicine and Veterinary Medicine, University of Edinburgh, after 4 months of embalming. No differences in anatomical detail or definition of organs were observed between US images obtained from different mice, suggesting similar embalming in all the six different protocols.

The visual appearance of the six mice did not show any changes between each other after four months of embalming. The B-mode images shown in Figure 72 are from a mouse embalmed using the Set IV protocol, as this is the same protocol used in Thiel human embalming. The US images of heart, kidney and liver obtained from Thiel mice (Set IV) acquired using the 35 MHz linear transducer (Vevo 800, Visualsonics, Toronto) are shown in Figure 72. Images acquired from live mice are also shown for comparison. Differences in the contrast between the two sets of images can be noticed. The higher contrast in the Thiel mice images is assumed to be because of the injected Thiel embalming fluids.

After 4 months of embalming, the Thiel mice, embalmed using different protocols, did not show any differences in organ preservation in the µUS images, as shown in Figure 72. The mice were kept immersed in the Thiel tank fluid for another 8 months and skin elasticity measurements were made using a shear wave optical coherence elastography (SW-OCE) system, developed in the US lab, University of Dundee. This case study, discussed further below, not only estimates the shear modulus of the Thiel mouse skin but also demonstrates the use of small anatomical tissue models for testing high resolution imaging systems.

7.3.2 Shear Modulus of Thiel Mice Skin Using SW-OCE System.

The shear modulus, *G*, of Thiel mouse skin was measured using the SW-OCE system. SW-OCE is a novel transient elastography method which produces high resolution quantitative elasticity maps as shown from a series of phantom studies (Song 2013a; Song 2013b; Nguyen 2014).

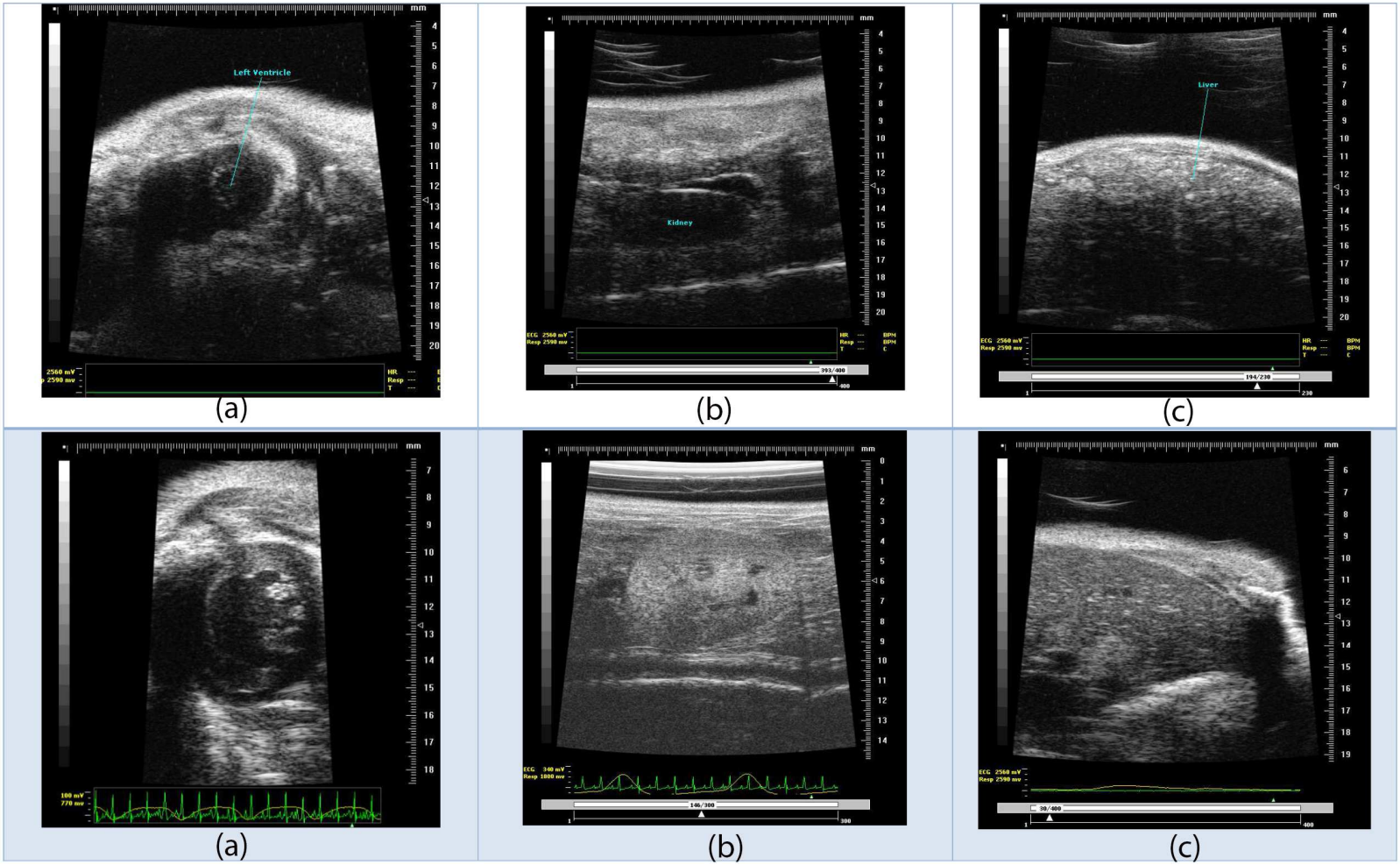

Figure 72: High frequency US B-mode images acquired from Thiel mice embalmed using Set IV protocol (top) and corresponding in-vivo B-mode images (bottom) of (a) heart, (b) kidney and (c) liver (Live mice images: Courtesy - Carmel Moran).

SW-OCE uses a piezoelectric actuator to produce mechanical vibrations in the tissue and the propagated shear waves are tracked in space and time using a phase sensitive Optical Coherence Tomography (OCT) (PhS-OCT) system at an equivalent frame rate of 47 kHz. The lateral pixel size is approximately 25 µm, allowing reconstruction of the local shear modulus (tissue stiffness) with high spatial resolution. The shear wave velocity is calculated from recorded wave data and the shear modulus is estimated using Equation 3.The detailed set-up and description of the system are given in the literature (Song 2013a; Song 2013b; Nguyen 2014) and are not explained further.

7.3.2.1 Experimental Set-up

The SW-OCE system used for calculating the shear modulus of the Thiel mice (imaged after 12 months of embalming) and fresh mouse skin was developed in the US lab at University of Dundee. Skin towards the lower end of the spine, was selected for study. This particular area was selected due to the ease of positioning the mice for experiments and the area was easy to mark in different mice. A black ink was applied to the surface to increase the absorption coefficient of light. The experiments were repeated with *ex-vivo* fresh wild type dead mice (one male and one female both aged six months at death), imaged within 30 minutes of death. The deceased mice were carried to the facility soon after death, with transportation time 20 minutes. Hair removal cream was applied for 10 minutes and the hair was wiped off using cotton (Figure 73). Thus, the SW-OCE studies were conducted 30 minutes after death as shown in Figure 73

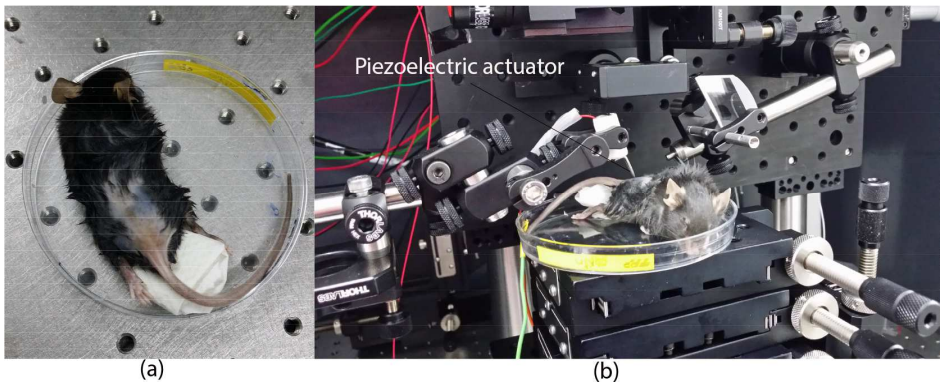

Figure 73: (a) Deceased fresh wild type mice after removing the hair near the end of the spine and (b) SW-OCE imaging set-up.

A comparison of the tissue stiffnesses in terms of their shear moduli is presented further.

7.3.2.2 Results

Figure 74 shows the structures of the skin of Thiel mice and fresh dead mice superimposed with colour map demonstrating the shear modulus obtained using the SW-OCE system.

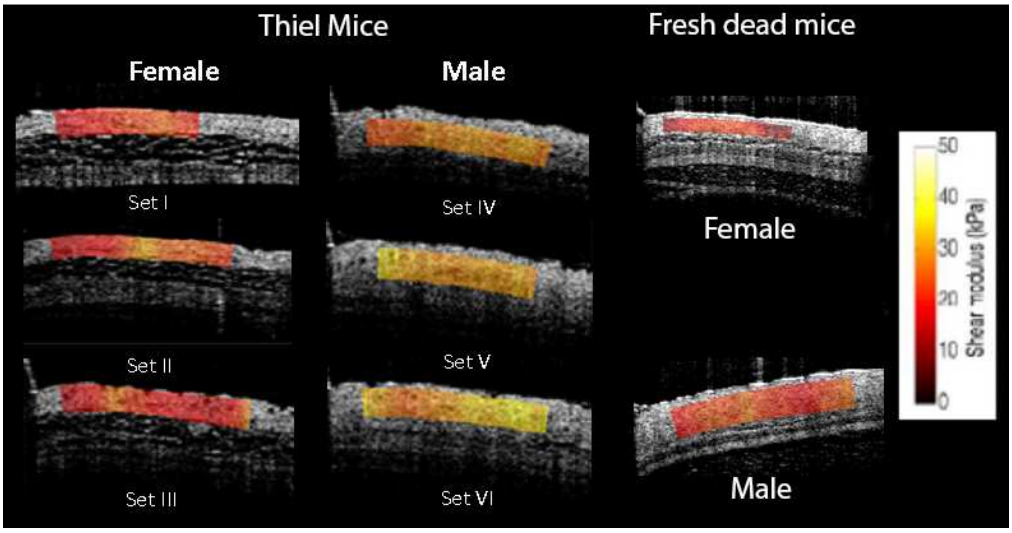

Figure 74: Shear modulus maps in of the skin of fresh dead and Thiel mice in KPa.

The SW-OCE images show distinguishable difference in skin structure: the dermis layer thickness in female mice is significantly lower than male mice in both the fresh (Song 2015) and Thiel. The mean value of the shear modulus of a central region of the elastogram (0.16 mm deep * 1.5 mm long) is calculated and displayed in Figure 75, together with the standard deviation. Elasticity values in Thiel mice are compared with the values from fresh dead mouse skin for both males and females.

Significant differences were noticed between the skin stiffness for male and female mice both fresh and Thiel. However, there were no significant differences in skin stiffnesses between mice of the same sex embalmed using different protocols. In fresh mice, both sexes show averaged shear modulus values < 12 KPa, about three times lower than the Thiel mice. The trend of lower shear modulus in female than male skin remains the same in both the fresh and Thiel mice, as depicted in Figure 75.

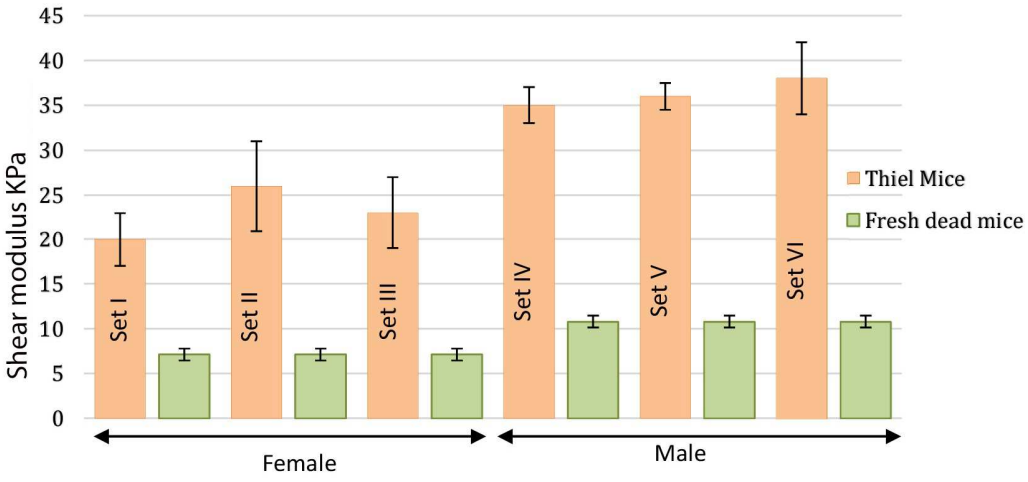

Figure 75: Shear moduli of Thiel mice compared with fresh dead mice for both sexes.

The results indicate that the different embalming protocols did not have a significant effect on the skin stiffness in the Thiel-embalmed mice. The same Thiel tank fluid was used in immersing mice in all protocols and this may be the reason for the similarity in skin stiffness values. Similar to the SWE study of TEC in Chapter 4, Thiel cadaveric tissue is stiffer than the fresh *ex-vivo* tissue and there are differences in the skin stiffness values between both sexes.

7.3.3 Microultrasound Scanning

Since mice are an important target for μUS imaging, the development of μUS systems may benefit from an anatomically accurate, easily accessible Thiel mouse model. A μUS step scanner, developed in the US lab, Ninewells Hospital, Dundee was used to image Thiel mice with a 45 MHz transducer of 4.75 mm focal length in a study that aimed to look at the differences in the high frequency images of the six mice 2.5 years after first embalming. It also showed the possibility of using Thiel mice as an anatomical model during the testing and developing of the high frequency imaging system.

7.3.3.1 Experimental Set-up

The μUS scanning set-up is shown in Figure 76. 2 ml of degassed, 10% phosphate buffer solution (PBS) was introduced to the stomach and colon orally in order to remove air

pockets. The mouse cadaver was adhered to an acoustic absorber sheet using pins and was immersed in the degassed 10% PBS solution as seen in Figure 76.

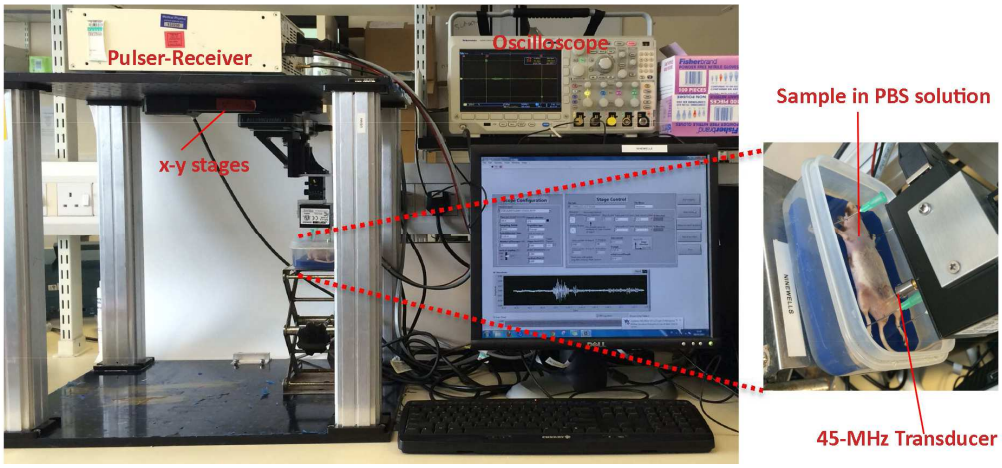

Figure 76: µUS scanning set-up

The scanning plane was selected to be at a distance of 15 mm towards the head from the urethral opening, across the colon and the pelvic symphysis as shown in Figure 77. This plane was specifically selected as it was easy to locate in different mice irrespective of their size.

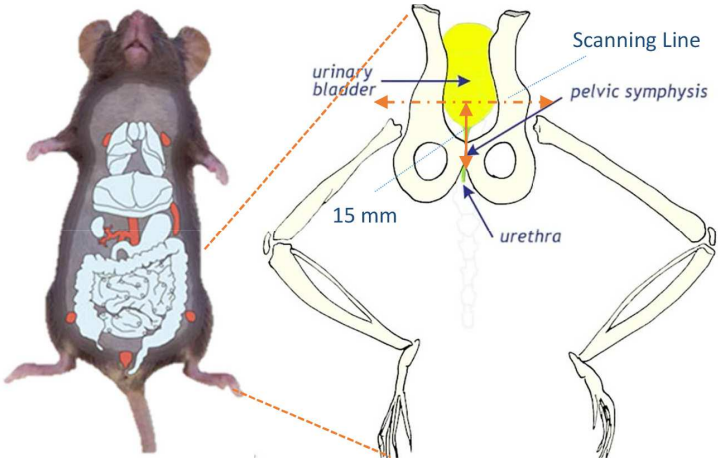

Figure 77: Mouse anatomy schematic and the scanning line (Unisciel 2013).

Visual images of the mice are shown in Figure 78. It can be seen that there are noticeable changes in the appearance of the skin in all the different mice. Mice embalmed using sets IV, V and VI protocols appeared to be preserved better way than those with sets I, II and III.

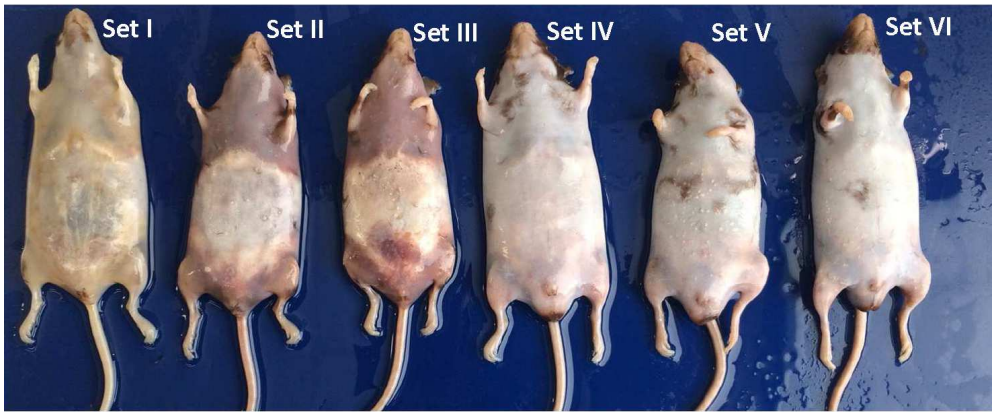

Figure 78: All mice from I to VI imaged 2.5 years after embalming date.

7.3.3.2 Results

The μUS images of the six different mice are shown in Figure 79 along the scanning plane marked in Figure 77.The μUS images of the colon and pelvic symphysis shows differences in the US propagation in mice embalmed using different protocols. Sets II and IV images show clearer images at increasing depth. Sets V and VI images appear grainy due to the presence of hair follicles in the PBS immersion solution. During the imaging, repeated changing of the PBS solution was used to decrease the presence of these follicles but this could not reduce the grainy appearance to any large extent.

The embalming from Set IV to Set VI has to be viewed as forming a scale of decreased embalming effects, where Set IV appears very well embalmed (visibly and in the US image) and Set VI appears not completely embalmed with some hair follicles still intact on the skin. Similarly, Set III to Set I can be seen as on a scale of increased embalming effects, where Set III is over-embalmed, with tissue nearing deterioration, and Set I well embalmed, with some tissues in the abdominal region more embalmed than needed. So far, from the visible appearance and the μUS images, the Set IV mouse, embalmed using the same protocol as for humans, appears to be the best preserved. However, the preservation of the internal organs need to be assessed before reaching any conclusions.

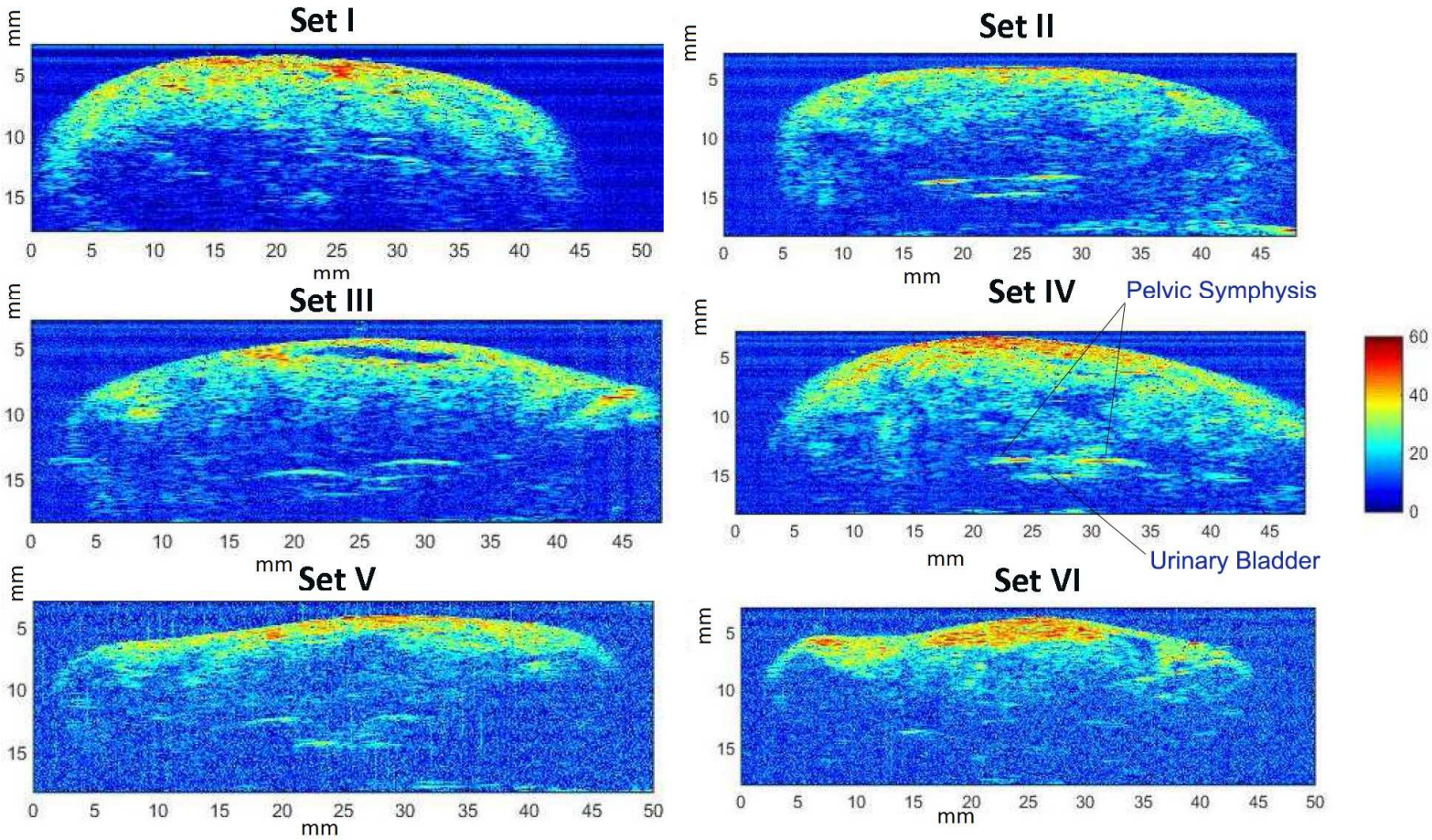

Figure 79: Mid-abdomen μUS images of six mice embalmed using different protocols.

7.3.4 MRI Imaging of Thiel Mice

In order to image the organs in Thiel mice embalmed using different protocols, they were imaged using 1.5 T MRI. The MRI images were acquired using a Signa HDx (GE Healthcare, USA) 1.5 T MRI scanner using a Fast Spoiled Gradient Echo (FSGE) MRI sequence with echo time (TE) 14.1 ms and repetition time (TR) 315 ms. This particular sequence is selected for imaging due to its ability in generating high quality images for smaller structures such as mice kidneys (Tang 2014). In clinical scenarios, FSGE is used for imaging small lesions, micro bleeds etc. Slices showing the kidneys of different mice were selected and compared to observe the changes in organ preservation. A fresh dead mouse was also imaged within 30 minutes of death for comparison.

Figure 80 shows a close view of kidneys in mouse embalmed with Set IV. The MRI coronal images of the kidneys in Figure 81 shows that they are preserved differently in mice embalmed using different protocols; the mouse embalmed using the Set IV protocol shows a higher degree of preservation with Set III being the least preserved, as the kidneys are no longer intact and appear damaged. It is also worth noting that the images in Figure 81 acquired from the fresh dead mouse show the presence of air in the lungs.

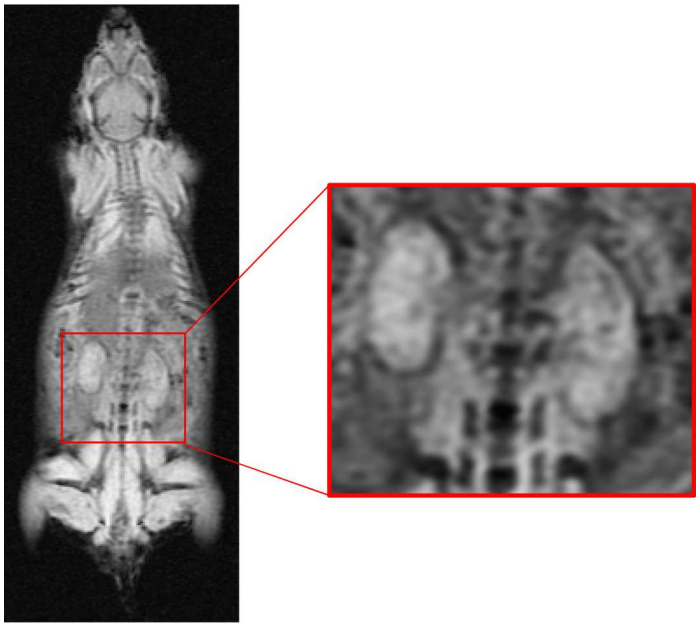

Figure 80: MRI Images of kidneys in Set IV mouse, a closer look.

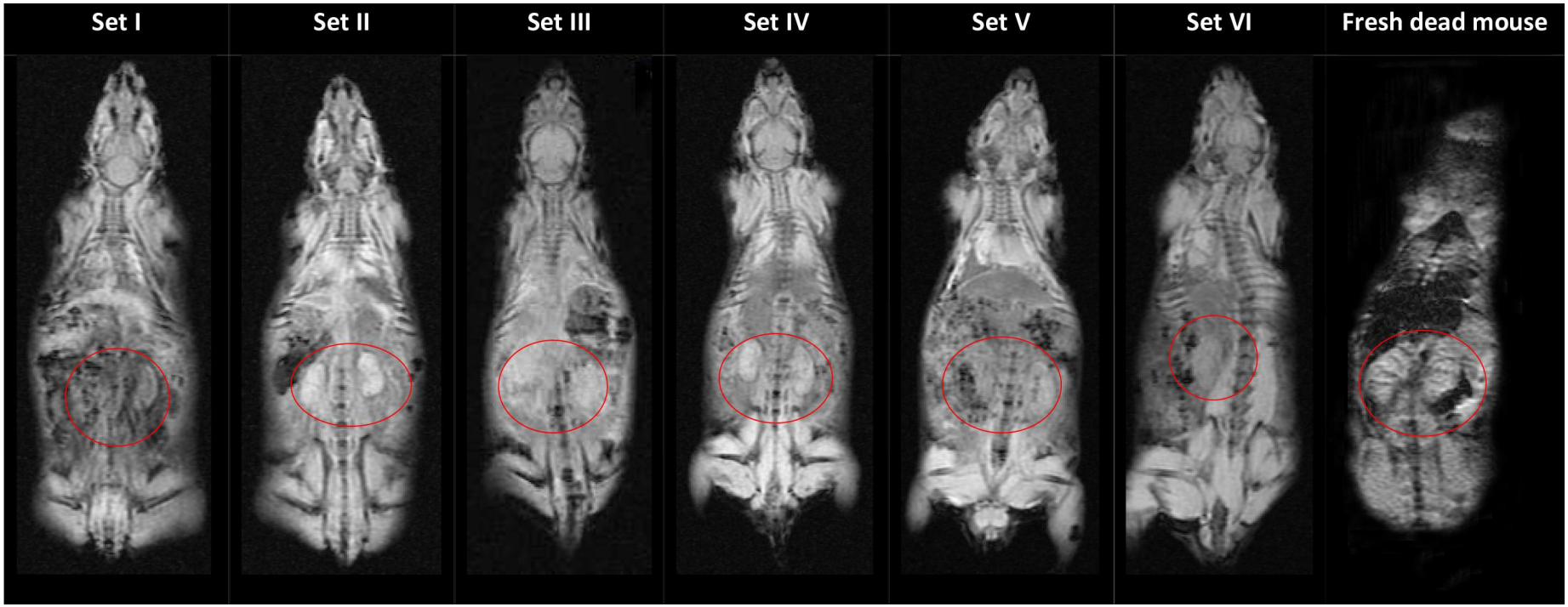

Figure 81: MRI coronal images of Thiel mice obtained IP to see the kidneys (Marked in red circles), compared with an MRI images of a fresh dead mouse.

7.4 DISCUSSION AND CONCLUSIONS

This Chapter considered different protocols for embalming small animals such as mice. The mice embalmed using six different protocols were imaged using SW-OCE, high frequency US and MRI. Two case studies are also discussed demonstrating the use of these readily accessible, qualitative anatomical models during the development and testing of high resolution imaging systems. Six embalming protocols, named as sets I to VI (3 male, 3 female) were used for embalming, with Set IV similar to the TEC protocol used for humans in the literature.

The mice were imaged using a commercial μUS imaging system after four months of embalming and the images were compared with those acquired from live mice models. There were no significant differences between different mice in the external appearance or in the US images at this stage. 12 months after the embalming date, the elasticity of the mouse skin was assessed using the SW-OCE system developed in the lab and was compared with the stiffness values acquired from fresh dead mice.

Significant differences were noted between the skin stiffness values for males and females for both the fresh and embalmed mice. However, there was no significant differences in skin stiffnesses between mice embalmed using different protocols within the same gender. This may be because the immersion fluid was the same in all protocols. In fresh mice, both sexes showed averaged shear modulus values < 12 kPa, about three times lower than the embalmed mouse skin. The lower shear modulus in female skin than male skin remained the same in both the embalmed and the fresh mice.

2.5 years after the embalming date, corresponding approximately to the maximum permitted use of human TECs, embalmed mice were imaged using a μUS step scanner developed in the US lab, University of Dundee. The images of the colon and pelvic symphysis in Figure 79 showed differences in mice embalmed using different protocols. Set II and IV mice images appeared clearer at increasing depth, as shown in Figure 78. From the images acquired from the μUS scanner and from the visible appearance of the mice, embalming Set IV, the same protocol as human TECs, appeared to be the most suitable for embalming small animals. This was confirmed by imaging the mice using MRI, which showed the best tissue preservation in the Set IV mice.

In summary, this Chapter has optimised the small animal embalming protocol and it was shown that the TEC embalming protocols described in the literature for humans can also be used to embalm small animals, like mice. The case studies that have been presented, imaging the mice with SW-OCE and with the μUS step scanner demonstrate possible uses of the novel model. To bring the SW-OCE system and the μUS scanner a step closer to *in-vivo* clinical applications, *ex-vivo* studies were carried out using fresh and embalmed mouse models. This not only shows the usefulness of small, readily accesible, anatomical tissue models for system testing, but also demonstrates the suitability of Thiel-embalmed mice for such purposes.

The advantages of using embalmed mice over fresh dead mice or frozen dead mice, or *in-vivo* small animal models when a live model is not a necessity, are that they carry no infection risk, are low cost, reusable, easier to handle and are readily accessible. The possibility to re-use the same mice repeatedly, provides experimental advantages in imaging system development. Because of their size, the embalming process is relatively easy, with no need for quantities of chemicals, and they are easily stored. Thiel mice could potentially be a successful replacement for live mice in the *in-vivo* studies where physiological feedback is not necessary. Moreover, because of their reusability they could potentially reduce the number of mice required for a study. To summarise, this Chapter has introduced Thiel mice for testing μUS systems during their development stage.

CHAPTER 8

Conclusions and Future Work

8.1 INTRODUCTION

This is the concluding Chapter of this thesis and includes a summary of key results achieved in the three main sections discussed. This thesis has discussed and analysed different models and techniques for research and testing of contemporary US systems. The key conclusions of this thesis is summarised in Table 13. The amplified summary is discussed further under each sub-section.

Table 13: Key conclusions of the thesis.

Medical Ultrasound Systems	Testing Models
SWE system	SWE system is suitable for measuring tissue stiffness in TEC models.
Interventional UGRA research	Two case studies show the suitability of TEC models for UGRA research.
Therapeutic breast cancer research	TEC breast tissue is an inappropriate model for therapeutic breast FUS research. The search for an ideal model is continuing.
µUS imaging systems	Thiel mice are a good model for testing high frequency US systems and the same protocol to preserve humans can be used with small animals.
Widely used US B-mode imaging systems	Acoustic test objects with artificial TMMs can be used for frequently performed QA tests and the automated DDP can be used during detailed QA tests as it can produce a single FoM for US system-transducer combinations.

8.2 ACOUSTIC TEST OBJECTS

Acoustic test objects with artificial TMMs are used nowadays for frequently performed US QA tests. A detailed review of these materials is presented in the literature (Culjat 2010). In addition to being used for QA, TMMs are also used as basic tissue models during research and development of US systems. In order to create a base line, a range of TMMs were prepared in the lab and their acoustic and mechanical properties were

measured and compared with the values in the literature. All materials tested, except agar, met the necessary standards (AIUM 1990, IEC 1996) in terms of the acoustic velocity, acoustic impedance and attenuation coefficient. Appendix I of this thesis includes recipes and detailed steps for the preparation of these most commonly used TMMs.

Even though TMMs have several limitations, they are the most commonly used materials for US systems testing. Hence as future work, a detailed study analysing the changes in the mechanical and acoustical properties of widely used TMMs over time would help towards appropriate selection of TMM for specific needs.

Irrespective of the wide use of acoustic test objects with TMMs, there is a need for an anatomically significant, qualitative tissue model for US systems testing. A feasible solution would be to use TEC. These specific soft-embalmed models have been shown to be increasingly used over the last decade for medical research, partly because they are US compatible, unlike the cadavers embalmed using other methods (Eisma 2013). The work discussed in this thesis has assessed the suitability of TEC for their use as a model for testing various different areas of US development.

8.3 SHEAR WAVE ELASTOGRAPHY SYSTEM

The suitability of the TEC models for testing SWE system (Bercoff 2004, Bercoff 2010) has been evaluated by conducting a quantitative analysis of TEC tissue stiffness and comparing the results with the *in-vivo* human volunteer data (Arda 2011). TEC models embalmed in tank and bags were included for the study. The tissue stiffness values for bag-embalmed TECs were found to be higher compared to those in tanks. This finding is useful as it suggests one way to achieve proper selection of a cadaver for a specific application. While a subjects embalmed in a bag is less useful for research related to tissue properties, it would find many uses for studies needing slightly stiffer subjects such as biomechanical studies and surgical training.

Close correlation was found between tank embalmed TEC tissue stiffness values and the *in-vivo* elasticity values, demonstrating the life-like characteristics of TEC. This is relevant as it indicates the possibility of using TECs during the development and testing of SWE systems (Joy 2015). One of the limitations of the study is the small number (n=8) of

cadavers assessed. A potential expansion of the study would be to include more subjects and conduct measurements of elasticity at different time points during embalming. This would help assess the changes in tissue stiffness values in the TEC models over time, thus providing more information on a time window where the properties of TECs remain almost the same. This would help users to specify a period during which these models can be used for repeated tests for research and development of systems.

8.4 INTERVENTIONAL ULTRASOUND

The use of TECs for interventional US, in UGRA research has also been assessed using two case studies. The first case study assessed TEC for a specific nerve stiffness study and the results supported the use of SWE system for nerve blocks in UGRA because of significant differences between the neural and extraneural tissue (Johnson 2009, Munirama 2012, Munirama 2013). The second case study used the TEC model to study the visibility of different types of needles, when used for UGRA nerve blocks. Because of ethical reasons, studies like needle insertion cannot be conducted on human volunteers.

TECs have proved to be very useful models for these studies because of their anatomical similarity and, in the case of UGRA, the sensing of tissue feedback compared to live human volunteers (McLeod 2010). Irrespective of the specific results from case studies, both studies demonstrate the suitability of TECs being used as tissue models during interventional US research (Munirama 2015).

8.5 THERAPEUTIC ULTRASOUND

The suitability of TEC breast tissue for pre-clinical breast cancer therapeutic US research has also been assessed. The results indicated that the TEC model may not be suitable for breast cancer research as it failed to produce any lesions on sonicating. One of the effects of Thiel embalming is that the salt solution denatures the tissues (Holzle 2012) and this might be a reason for the failure to produce lesions during sonication as heating also denatures the tissue. This was later explained to be because of differences in the US attenuation coefficient values between the two. There is also the point that if Thiel tissue is denatured, the consequent reduction in microstructure may relate to the lower levels of attenuation. The pre-existing denaturation made it not possible to locate the lesion even during the histopathology analysis.

The differences in the temperature readings between the MRI PRFS thermometry and temperature probe measurements during fatty tissue sonications has also been assessed. It was observed that there were differences between the peak temperatures at same power and the percentage difference increased significantly at higher powers.

MRI PRF thermometry is based on the phase variations with changes in temperatures (Pan 2010). Because of the reduced hydrogen bonds in fat, the phase variation with temperature is negligible and at higher powers, melting of more fat makes these phase changes almost absent, resulting in higher percentage errors. Temperature comparison experiments were repeated using fresh *ex-vivo* chicken breast samples and the measured temperature using both methods showed good agreement.

Though clinically, the use of MRI PRFS based thermometry during sonication of *in-vivo* human breast tumours would work, problems might arise in measuring temperatures in the margins especially when the tumour is surrounded by fat. The study has indicated that TEC breast tissue may not be suitable for breast HIFU pre-clinical trials and thus the search for an ideal human breast model still continues (Joy 2015b).

8.6 MICROULTRASOUND

In order to meet the demand for a small, anatomical model for testing high frequency, μUS systems, readily accessible, qualitative, reusable Thiel mice models has been considered. Different embalming protocols were tested to find the optimum the embalming procedure. It was observed that the Thiel protocol used in embalming human cadavers was suitable for embalming small animals like mice, preserving its anatomical characteristics. Among the various protocols tried, mice embalmed with the original Thiel protocol showed the greatest similarity to fresh dead mice in terms of organ and tissue preservation and mechanical properties (Song 2015).

The case studies presented in imaging the mice with the SW-OCE system (Song 2013a, Song 2013b) and the μUS step scanner not only demonstrated the usefulness of small, readily accesible, anatomical tissue models for system testing, but also demonstrated the suitability of Thiel-embalmed mice for such purposes (Song 2015).

The advantages of using Thiel mice over fresh dead mice or frozen dead mice, or *in-vivo* small animal models is that they carry no infection risk, are low cost, reusable, easier to

handle and are readily accessible. A comprehensive study by embalming more mice using the Set IV (Thiel) embalming technique (Thiel 1992a, Thiel 1992b) and assessing the changes over time would be helpful.

This would find a time period during which the properties of the mice are more or less remain the same (less deterioration), increasing the possibility to re-use the same mice repeatedly, provides experimental advantages in imaging system development. Thiel mice could potentially be a successful replacement for live mice in the *in-vivo* studies where physiological feedback is not necessary. Moreover, because of their reusability they could reduce the number of mice required for a study, thus allowing us to adherence to the three Rs in animal testing.

REFERENCES

"<Dundee et al. - 2011 - National Express Dundee Bus Times Services 28 & 29 Douglas Loop – Asda Milton – Craigiebank – Arbroat.pdf>."

Abhijeet, Y. and Y. Mukul (2014). "A Study of the Effects of Formalin on First Year MBBS Students." *Scholars Journal of Applied Medical Sciences* **2**(5B): 1588-1590.

Ahmad, S., R. Cao, T. Varghese, L. Bidaut and G. Nabi (2013). "Transrectal quantitative shear wave elastography in the detection and characterisation of prostate cancer." *Surg Endosc* **27**(9): 3280-3287.

AIUM (1990). Standard methods for measuring performance of pulse-echo ultrasound imaging equipment. Rockville,MD, American Institute of Ultrasound in Medicine**:** 43-48.

Andrew, T. G. (2006). "Ultrasound-guided Regional Anesthesia - Current State of the Art." *Anesthesiology* **104**(2): 368-373.

Ang, W., C. Hoy, W. El-Bialy, T. Tsui and Y. Chen (2010). "Design and Implementation of therapeutic ultrasound generating circuit for dental tissue formation and tooth-root healing." *IEEE Trans Biomed Circuits Syst* **4**: 19-61.

Angelique, F. V. and L. A. Newman (2007). "Complications in Breast Surgery." *Surg Clin North Am* **87**: 431-451.

Arda, K., N. Ciledag, E. Aktas, B. K. Aribas and K. Kose (2011). "Quantitative assessment of normal soft-tissue elasticity using shear-wave ultrasound elastography." *AJR Am J Roentgenol* **197**(3): 532-536.

ATS (1978). "ATS Laboratories-Phantoms." Retrieved 2 February, 2015, from http://www.atslaboratories-phantoms.com/page5/index.html.

Balta, J. Y., C. Lamb and R. W. Soames (2014). "A pilot study comparing the use of Thiel- and formalin-embalmed cadavers in the teaching of human anatomy." *Anatomical Sciences Education*.

Barr, R. (2014). Ultrasound Elastography: Applications in Tumors. *Functional Imaging in Oncology*. V. Luna, d. C. Hygino and F. Rossi Fanelli. Heidelberg, Springer**:** 159-190.

Bavu, E., J. Gennisson and B. Osmanskiy (2009). "Liver fibrosis staging using supersonic shear imaging: a clinical study on 142 patients." *Proceedings of the IEEE International Ultrasonics Symposium. Rome, Italy: IEEE*.

Bavu, E., J. L. Gennisson, M. Couade, J. Bercoff, V. Mallet, M. Fink, A. Badel, A. Vallet-Pichard, B. Nalpas, M. Tanter and S. Pol (2011). "Noninvasive in vivo liver fibrosis

evaluation using supersonic shear imaging: a clinical study on 113 hepatitis C virus patients." *Ultrasound Med Biol* **37**(9): 1361-1373.

Benkhadra, M., A. Bouchot, J. Gerard, D. Genelot, P. Trouilloud, L. Martin, C. Girard, A. Danino, F. Anderhuber and G. Feigl (2011). "Flexibility of Thiel's embalmed cadavers: the explanation is probably in the muscles." *Surg Radiol Anat* **33**(4): 365-368.

Benkhadra, M., A. Faust, S. Ladoire, O. Trost, P. Trouilloud, C. Girard, F. Anderhuber and G. Feig (2009). "Comparison of fresh and Thiel's embalmed cadavers according to the suitability for ultrasound-guided regional anesthesia of the cervical region." *Surgical Radiol Anat* **31**: 531-535.

Benkhadra, M., J. Gerard, D. Genelot, P. Trouilloud, C. Girard, F. Anderhuber and G. Feigl (2011). "Is Thiel's embalming method widely known? A world survey about its use." *Surg Radiol Anat* **33**(4): 359-363.

Bercoff, J. (2008). Shear Wave Elastography. S. Imagine**:** 1-12.

Bercoff, J. (2010). The emergence of shear wave elastography in ultrasound. *RAD Magazine for Medical Imaging and Radiotherapy Professionals.***:** 2.

Bercoff, J. (2011). Ultrafast Ultrasound Imaging. *Ultrasound Imaging - Medical Applications*. V. M. Igor and V. M. Oleg InTech**:** 342.

Bercoff, J., M. Tanter and M. Fink (2004). "Supersonic Shear Imaging: A New Technique for Soft Tissue Elasticity Mapping." *IEEE Trans Ultrason Ferroelectr Freq Control* **51**(4): 396-409.

Betz, M. M., E. E. Benninger, P. P. Favre, K. K. Wieser, M. M. Vich and N. Espinosa (2013). "Primary stability and stiffness in ankle arthrodes-crossed screws versus anterior plating." *Foot Ankle Surg* **19**(3): 168-172.

Bhatia, K., C. Cho, C. Tong, E. Yuen and A. Ahuja (2012). "Shear wave elasticity imaging of cervical lymph nodes." *Ultrasound Med Biology* **38**(2): 195-201.

BluePhantom™ (2015). "By Phantom Type." Retrieved 30 January, 2015, from www.bluephantom.com.

Bradbury, S. A. and K. Hoshino (1978). "An improved embalming procedure for long-lasting preservation of the cadaver for anatomical study." *Acta Anat (Basel)* **101**(2): 97-103.

Brenner, E. (2014). "Human body preservation – old and new techniques." *Journal of Anatomy* **224**(3): 316-344.

Bromilow, J. (2012). "New MRI procedure hailed as the next generation of the operating room." Retrieved May 5th, 2015, from http://thepositive.com/new-mri-procedure-hailed-as-the-next-generation-of-the-operating-room/.

Browne, J. E., K. V. Ramnarine, A. J. Watson and P. R. Hoskins (2003). "Assessment of the acoustic properties of common tissue-mimicking test phantoms." *Ultrasound Med Biol* **29**(7): 1053-1060.

Bruining, D. H. and A. S. Arora (2007). "Fresh frozen cadavers for percutaneous liver biopsy training." *Medical Education* **41**(5): 521-522.

Bruno, Q., Z. Jacco A. de and M. Chrit T.W (2000). "Magnetic Resonance Temperature Imaging for Guidance of Thermotherapy." *Journal of Magnetic Resonance Imaging* **12**: 525-533.

Buscarini, E. (2011). Interventional ultrasound. *Manual of diagnostic ultrasound*. L. Harald and B. Elisabetta. Geneva, Switzerland, World Health Organization **1:** 43-65.

Cancer-Research-UK (2011). "Breast cancer Key Stats." Retrieved May 5th, 2015, from http://www.cancerresearchuk.org/cancer-info/cancerstats/keyfacts/breast-cancer/.

Carty, S. and B. Nicholls (2007). "Ultrasound-guided regional anaesthesia." *Continuing Education in Anaesthesia, Critical Care & Pain* **7**(1): 20-24.

Chin, K., A. Perlas, V. Chan and R. Brull (2008). "Needle Visualization in Ultrasound-Guided Regional Anesthesia: Challenges and Solutions." *Reg Anesth Pain Med* **33**(6): 532-544.

CIRS-Inc. "Ultrasound Resolution Phantom." Retrieved 2 February, 2015, from http://www.cirsinc.com/products/modality/70/ultrasound-resolution-phantom/.

Couade, M., M. Pernot, C. Prada, E. Messas, J. Emmerich, P. Bruneval, A. Criton, M. Fink and M. Tanter (2010). "Quantitative assessment of arterial wall biomechanical properties using shear wave imaging." *Ultrasound Med Biol* **36**(10): 1662-1676.

Coussios, C. and R. Roy (2008). "Application of acoustics and cavitation to noninvasive therapy and drug delivery." *Annual Review of Fluid Mechanics* **40**: 395-420.

Crum, L., M. Bailey, J. H. Hwang, V. Khokhlova and O. Sapozhnikov (2010). "Therapeutic ultrasound: Recent trends and future perspectives." *Physics Procedia* **3**(1): 25-34.

Culjat, M. O., D. Goldenberg, P. Tewari and R. S. Singh (2010). "A review of tissue substitutes for ultrasound imaging." *Ultrasound Med Biol* **36**(6): 861-873.

Dartmouth-Hitchcock (2015). "Anesthesiology - Essential Clinical Themes." Retrieved February 25th, 2015, from http://med.dartmouth-hitchcock.org/ultrasound_guided_anesthesia/essential_clinical_themes.html.

Diagnostic-Sonar-Ltd (2015). "Ultrasound Test Objects." Retrieved 01 February, 2015, from http://www.diagnosticsonar.com/artman/publish/article_48.shtml.

Dodge, Y. (2006). *The Oxford Dictionary of Statistical Terms*. Oxford [Oxfordshire], Oxford University Press

Duck , F. (1990). *Physical Properties of Tissue: a Comprehensive Reference Book*. (London: Academic)

Duck , F. (1998). *Ultrasound in Medicine*. Great Britain, Institute of Physics Publishing

Eisma, R. (12th October 2012). Personal Communication - cadaver usage data. J. Joy.

Eisma, R. (13th February 2015). Personal Communication - Cadaver count. J. Joy.

Eisma, R., C. Lamb and R. W. Soames (2013). "From formalin to thiel embalming: What changes? One anatomy department's experiences." *Clinical Anatomy* **26**(5): 564-571.

Eisma, R., S. Mahendran, S. Majumdar, D. Smith and R. W. Soames (2011). "A comparison of Thiel and formalin embalmed cadavers for thyroid surgery training." *Surgeon* **9**(3): 142-146.

Eisma, R. and T. Wilkinson (2014). "From "silent teachers" to models." *PLoS Biol* **12**(10): e1001971.

Eljamel, S., A. Volovick, T. Saliev, R. Eisma and A. Melzer (2014). "Evaluation of Thiel cadaveric model for MRI-guided stereotactic procedures in neurosurgery." *Surg Neurol Int* **5**(Suppl 8): S404-409.

Epstein, C. L. (2008). *Introduction to the mathematics of medical imaging.* . USA, SIAM

Evans, A., P. Whelehan, K. Thomson, D. McLean, K. Brauer, C. Purdie, L. Jordan, L. Baker and A. Thompson (2010). "Quantitative shear wave ultrasound elastography: initial experience in solid breast masses." *Breast Cancer Res* **12**(6): R104.

Fahey, B. J., R. C. Nelson, D. P. Bradway, S. J. Hsu, D. M. Dumont and G. E. Trahey (2008). "In vivo visualization of abdominal malignancies with acoustic radiation force elastography." *Physics in Medicine and Biology* **53**(1): 279.

Feng, W., W. Zhi-Biao, Z. Hui, C. Wen-Zhi, Z. Jian-Zhong, J. Bai, L. Ke-Quan, J. Cheng-Bing, X. Fang-Lin and S. Hai-Bing (2005). "Feasibility of US-guided high-intensity focused ultrasound treatment in patients with advanced pancreatic cancer: initial experience." *Radiology* **236**: 1034-1040.

Fessel, G., K. Frey, A. Schweizer, M. Calcagni, O. Ullrich and J. G. Snedeker (2011). "Suitability of Thiel embalmed tendons for biomechanical investigation." *Ann Anat* **193**(3): 237-241.

Fink, M. and M. Tanter (2010). "Multiwave imaging and super resolution." *Physics Today* **63**(2).

Fredrickson, M. and T. Danesh-Clough (2013). "Ultrasound-guided femoral catheter placement: a randomised comparison of the in-plane and out-of-plane techniques." *Anaesthesia* **68**: 382-390.

Fry, F. (1958). "Precision high intensity focusing ultrasonic machines for surgery." *Phys Med Biol* **37**: 152-156.

Fry, W., J. Barnard, F. Fry, R. Krumins and J. Brennan (1955). "Ultrasonic lesions in the mammalian central nervous system. ." *Science* **122**: 517-518.

Fry, W., W. Mosberg, J. Barnard and F. Fry (1954). "Production of focal destructive lesions in the central nervous system with ultrasound." *J Neurosurg Anesthesiol* **11**: 471-478.

Fu, H., J. Mueller, M. Javid, J. Mito, D. Kirsch, N. Ramanujam and J. Brown (2013). "Optimization of a widefield structured illumination microscope for non-destructive assessment and quantification of nuclear features in tumor margins of a primary mouse model of sarcoma." *PLoS One* **8**(7): e68868.

Furusawa, H., K. Namba, H. Nakahara, C. Tanaka, Y. Yasuda, E. Hirabara, M. Imahariyama and K. Komaki (2007). "The evolving non-surgical ablation of breast cancer: MR guided focused ultrasound (MRgFUS)." *Breast Cancer* **14**(1): 55-58.

Gabriela, W., L. Marko, B. Klaus, B. Thomas, E. Peter and W. Jurgen (2007). "Thermal properties and changes of acoustic parameters in an egg white phantom during heating and coagulation by high intensity focused ultrasound." *Ultrasound in medicine and biology* **33**(6): 981-986.

Gammex-RMI (1987). "Ultrasound Products." from http://www.gammex.com/n-portfolio/projects.asp?category=Ultrasound.

Gennisson, J. L., N. Grenier, C. Combe and M. Tanter (2012). "Supersonic shear wave elastography of in vivo pig kidney: influence of blood pressure, urinary pressure and tissue anisotropy." *Ultrasound Med Biol* **38**(9): 1559-1567.

Gennisson, L., T. Deffieux, M. Fink and M. Tanter (2013). "Ultrasound elastography: Principles and techniques." *Diagnostic and Interventional Imaging* **94**: 487—495.

Gibbs, V., D. Cole and A. Sassano (2011). *Ultrasound Physics and Technology: How, Why and When*, Elsevier Health Sciences UK

Graham, S., L. Chen, M. Leitch, R. Peters, M. Bronskill and R. Henkelman (1999). " Quantifying tissue damage due to Focused Ultrasound heating observed by MRI. ." *Magnetic Resonance in Medicine* **41**: 321-328.

Grant, S. A. and D. B. Auyong (2012). "Ultrasound guided regional anesthesia."

Gueorguieva, M. J., D. T. B. Yeo, R. Eisma and A. Melzer (2014). "MRI of thiel-embalmed human cadavers." *Journal of Magnetic Resonance Imaging* **39**(3): 576-583.

Guignard, J., C. Stieger, M. Kompis, M. Caversaccio and A. Arnold (2013). "Bone conduction in Thiel-embalmed cadaver heads." *Hear Res* **306**: 115-122.

Guo, S., A. Schwab, G. McLeod, G. Corner, S. Cochran, R. Eisma and R. Soames (2012). "Echogenic regional anaesthesia needles: a comparison study in Thiel cadavers." *Ultrasound Med Biol* **38**(4): 702-707.

Habash, R., B. Rajeev, K. Daniel and T. A. Hafid (2006). "Thermal therapy, part 1: an introduction to thermal therapy." *Crit Rev Biomed Eng* **34**(6): 459-489.

Hassan, S., R. Eisma, R. Soames, S. Waterston and L. Harry (2014). "Raising of microvascular flaps using the Thiel cadaveric model." *J Plast Reconstr Aesthet Surg* **67**(4): e107-108.

Hauptmann, M., P. Stewart, J. Lubin, B. F, R. Hornung, R. Herrick, R. Hoover, J. Fraumeni, A. Blair and R. Hayes (2009). "Mortality from lymphohematopoietic malignancies and brain cancer among embalmers exposed to formaldehyde." *J Natl Cancer Inst* **101**(24): 1696-1708.

Havel, M., L. Ertl, D. Bauer, M. Schuster, K. Stelter and J. Sundberg (2014). "Resonator properties of paranasal sinuses: preliminary results of an anatomical study." *Rhinology* **52**(2): 178-182.

Hebard, S. and G. Hocking (2011). "Echogenic technology can improve needle visibility during ultrasound-guided regional anesthesia." *Reg Anesth Pain Med* **36**(2): 185-189.

Hindman, J. (1966). "Proton resonance shift of water in gas and liquid states. ." *Journal of Chemical Physics* **44**: 4582-4592.

Histology-guide (2015). "The Histology Guide." *Making histological sections for the light microscope*. Retrieved June 23, 2015, from http://www.histology.leeds.ac.uk/what-is-histology/histological_sections.php.

Hitachi, M. S. (2015). "Real-time Tissue Elastography (RTE)." Retrieved 12 February, from http://www.hitachi-medical-systems.eu/products-and-services/ultrasound/technologies/hitachi-technologies/real-time-tissue-elastography-rte/clinical-applications.html.

Hocking, G. and C. H. Mitchell (2012). "Optimizing the safety and practice of ultrasound-guided regional anesthesia: the role of echogenic technology." *Curr Opin Anaesthesiol* **25**(5): 603-609.

Holm, H. H. and B. Skjoldbye (1996). "Interventional ultrasound." *Ultrasound Med Biol* **22**(7): 773-789.

Holzle, F., E. P. Franz, J. Lehmbrock, S. Weihe, C. Teistra, H. Deppe and K. D. Wolff (2012). "Thiel embalming technique: a valuable method for teaching oral surgery and implantology." *Clin Implant Dent Relat Res* **14**(1): 121-126.

Hornak, J. P. (2008). *Basics of MRI*, Interactive Learning Software

Huber, P. E., J. Jenne, R. Rastert, I. Simiantonakis, H. Sinn, H. Strittmatter, D. Fournier, M. Wannenmacher and J. Debus (2001). " A new noninvasive approach in breast cancer therapy using magnetic resonance imaging-guided focused ultrasound surgery. Cancer Res,61, pp.8441- 47." *Cancer Research* **61**: 8441-8447.

IBSR (2012). The Benefits and Harms of Breast Cancer Screening : An Independent Review. UK, Cancer Research UK and the Department of Health (England).

IEC (1996). Ultrasonics—Real–time pulse-echo systems—Guide for test procedures to determine performance specifications. Geneva, International Electrotechnical Commission.

Illing, R., J. Kennedy, F. Wu, G. ter Haar, A. Protheroe, P. Friend, F. Gleeson, D. Cranston, R. Phillips and M. Middleton (2005). "The safety and feasibility of extracorporeal high-intensity focused ultrasound (HIFU) for the treatment of liver and kidney tumours in a Western population." *Br J Cancer* **93**(8): 890-895.

Inglis, S., K. V. Ramnarine, J. N. Plevris and W. N. McDicken (2006). "An anthropomorphic tissue-mimicking phantom of the oesophagus for endoscopic ultrasound." *Ultrasound Med Biol* **32**(2): 249-259.

Ishihara, Y., A. Calderon, H. Watanabe, K. Okamoto, Y. Suzuki, K. Kuroda and S. Yutaka (1995). "A precise and fast temperature mapping using water proton chemical shift." *Magn Reson Med.* **34**: 814–823.

Itoigawa, Y., J. W. Sperling, S. P. Steinmann, Q. Chen, P. Song, S. Chen, E. Itoi, T. Hatta and K. N. An (2015). "Feasibility assessment of shear wave elastography to rotator cuff muscle." *Clin Anat* **28**(2): 213-218.

Jaung, R., P. Cook and P. Blyth (2011). "A comparison of embalming fluids for use in surgical workshops." *Clinical Anatomy* **24**(2): 155-161.

Jiang, Y., G. Li, L. Qian, X. Hu, D. Liu, S. Liang and Y. Cao (2015). "Characterization of the nonlinear elastic properties of soft tissues using the supersonic shear imaging (SSI) technique: Inverse method, ex vivo and in vivo experiments." *Med Image Anal* **20**(1): 97-111.

Johnson, R. (2009). Analysis of Variance. *Statistics: Principles and Methods*, John Wiley & Sons**:** 544-576.

Jolesz, F. A. (2009). "MRI-Guided Focused Ultrasound Surgery." *Annu Rev Med* **60**: 417-430.

Joseph, W. (1995). "A short History of the development of Ultrasound in Obstetrics and Gynecology." Retrieved 06th February, 2015, from http://www.ob-ultrasound.net/history1.html.

Joy, J., G. McLeod, N. Lee, S. Munirama, G. Corner, R. Eisma and S. Cochran (2015). "Quantitative Assessment of Thiel Soft-embalmed Human Cadavers using Shear Wave Elastography " *Annals of Anatomy - Anatomischer Anzeiger* **202**: 52-56.

Joy, J., Y. Yang, P. Colin, R. Eisma, S. Cochran and S. Vinnicombe (2015b). "Soft-embalmed Human Breast Tissue as a Model for Pre-clinical Trials of HIFU - A feasibility study." *J Ther Ultrasound* **In Preparation**.

Julian, V. (2012). *Structural Biomaterials*. New Jersey 08540, Princeton University Press

Kainz, H., W. Reng, P. Augat and S. Wurm (2012). "Influence of total knee arthroplasty on patellar kinematics and contact characteristics." *Int Orthop* **36**(1): 73-78.

Kang, P., A. Horgan and A. Acheson (2009). "Laparoscopic surgery training. Try fresh frozen cadavers." *BMJ* **338**: b2426.

Karakitsios, I., M. Bobeica, T. Saliev, M. Rube and A. Melzer (2014). "Thermometry during MR-guided focused ultrasound in a preclinical model based on Thiel embalmed tissue." *Minim Invasive Ther Allied Technol* **23**(2): 120-126.

Katherine, A. and S. Scott (2008). "Why Epidurals Do Not Always Work." *Rev Obstet Gynecol* **1**(2): 49-55.

Kennedy, J. E. (2003). "High intensity focused ultrasound: surgery of the future?" *British Journal of Radiology* **76**(909): 590-599.

Krishnan, K. G., T. Pinzer, F. Reber and G. Schackert (2004). "Endoscopic Exploration of the Brachial Plexus: Technique and Topographic Anatomy???A Study in Fresh Human Cadavers." *Neurosurgery* **55**(5): 401-409.

Lee, W., M. Pernot, M. Couade, E. Messas, P. Bruneval, A. Bel, A. Hagege, M. Fink and M. Tanter (2012). "Mapping myocardial fiber orientation using echocardiography-based shear wave imaging." *IEEE Trans Med Imaging* **31**(3): 554-562.

Leissner, J., E. P. Allhoff, W. Wolff, C. Feja, M. Hockel, P. Black and R. Hohenfellner (2001). "The pelvic plexus and antireflux surgery: topographical findings and clinical consequences." *J Urol* **165**(5): 1652-1655.

Li, S. and P. H. Wu (2013). "Magnetic resonance image-guided versus ultrasound-guided high-intensity focused ultrasound in the treatment of breast cancer." *Chin J Cancer* **32**(8): 441-452.

Liberman, B., D. Gianfelice, Y. Inbar, A. Beck, T. Rabin, N. Shabshin, G. Chander, S. Hengst, R. Pfeffer, A. Chechick, A. Hanannel, O. Dogadkin and R. Catane (2006). "Pain palliation in patients with bone metastases using MR-guided focused ultrasound surgery: A Multicenter Study." *Annals of Surgical Oncology* **16**(1): 140-146.

Lunn, R., G. Jahnke, D. Spencer, S. Garner, S. Atwood, G. Carter, A. Ewens, D. Greenwood, J. Ratcliffe and T. Desrosiers (2010). Final report on carcinogens background document for formaldehyde**:** i-552.

Lutz, H. T. (2011). Basics of Ultrasound. *Manual of diagnostic ultrasound*. H. T. Lutz and B. Elisabetta, World Health Organization**:** 3-35.

Lynn, J., R. Zwemer, A. Chick and A. Miller (1942). "A new method for the generation and use of focused US in experimental biology." *J. Gen. Physiol* **26**: 179-193.

Lynn, J. G. and T. J. Putnam (1944). "Histology of Cerebral Lesions Produced by Focused Ultrasound." *Am J Pathol* **20**(3): 637-649.

Madsen, E. L., G. R. Frank and F. Dong (1998). "Liquid or solid ultrasonically tissue-mimicking materials with very low scatter." *Ultrasound Med Biol* **24**(4): 535-542.

Madsen, E. L., M. Hobson, H. Shi and T. Varghese (2005). "Tissue-mimicking agar/gelatin materials for use in hetrogeneous elastography phantoms." *Phys Med Biol* **20**: 5597-5618.

Maecken, T., M. Zenz and T. Grau (2007). "Ultrasound Characteristics of Needles for Regional Anesthesia." *Reg Anesth Pain Med* **32**: 440-447.

Magri, F., S. Chytiris, V. Capelli, S. Alessi, E. Nalon, M. Rotondi, S. Cassibba, F. Calliada and L. Chiovato (2012). "Shear wave elastography in the diagnosis of thyroid nodules: feasibility in the case of coexistent chronic autoimmune Hashimoto's thyroiditis." *Clin Endocrinol (Oxf)* **76**(1): 137-141.

Martin, K. (2010). Introduction to B-mode Imaging. *Diagnostic Ultrasound: Physics and Equipment*. P. R. Hoskins, K. Martin and A. Thrush, Cambridge University Press.

Martin, K. and K. V. Ramanarine (2010). Physics. *Diagnostic Ultrasound: Physics and Equipment*. P. R. Hoskins, K. Martin and A. Thrush, Cambridge University Press.

Mayer, R. (2012). *Embalming : History, Theory and Practice.* New York, McGraw-Hill.728

McLeod, G., R. Eisma, A. Schwab, G. Corner, R. Soames and S. Cochran (2010). "An evaluation of Thiel-embalmed cadavers for ultrasound-based regional anaesthesia training and research." *Ultrasound* **18**(3): 125-129.

Mikla, V. I. and V. V. Mikla (2014). 7 - Ultrasound Imaging. *Medical Imaging Technology*. V. I. Mikla and V. V. Mikla. Oxford, Elsevier**:** 113-128.

Mischi, M., N. Rognin and M. Averkiou (2014). Ultrasound Imaging Modalities. *Comprehensive Biomedical Physics*. A. Brahme. Oxford, Elsevier**:** 361-385.

Mitragotri, S. (2005). "Healing sound: the use of ultrasound in drug delivery and other therapeutic applications." *Nature Reviews-Drug Discovery* **4**: 255-0260.

Mori, M., M. Hoshiko, K. Hara, T. Saga, K. Yamaki and T. Ishitake (2013). "Changes in subjective symptoms and allergy state among medical students exposed to low-level formaldehyde 6 months after completion of a gross anatomy dissection course." *Environ Health Prev Med* **18**(5): 386-393.

Muller, M., J. L. Gennisson, T. Deffieux, M. Tanter and M. Fink (2009). "Quantitative viscoelasticity mapping of human liver using supersonic shear imaging: preliminary in vivo feasibility study." *Ultrasound Med Biol* **35**(2): 219-229.

Munirama, S., J. Joy, M. Columb, R. Habershaw, R. Eisma, G. Corner, S. Cochran and G. McLeod (2014). "A randomised, single-blind technical study comparing the ultrasonic visibility of smooth-surfaced and textured needles in a soft embalmed cadaver model." *Anaesthesia*: n/a-n/a.

Munirama, S., J. Joy, M. Columb, R. Habershaw, R. Eisma, G. Corner, S. Cochran and G. McLeod (2015). "A randomised, single-blind technical study comparing the ultrasonic visibility of smooth-surfaced and textured needles in a soft embalmed cadaver model." *Anaesthesia* **70(5)**: 537-542.

Munirama, S., J. Joy, R. Eisma, G. Corner, S. Cochran and G. McLeod (2013). "Images in anesthesiology: shear wave elastography: novel technology for ultrasound-guided regional anesthesia." *Anesthesiology* **119**(3): 698.

Munirama, S., J. Joy, R. Eisma, G. Corner, S. Cochran and G. McLeod (2013). "Shear wave elastography: novel technology for ultrasound-guided regional anesthesia." *Anesthesiology* **119**(3): 698.

Munirama, S., J. Joy, R. Habeshaw, R. Eisma, G. Corner, S. Cochran, R. Soames and G. McLeod (2012). *Comparison of intraneural and extraneural shear modulus in the Thiel-embalmed human cadaver*. British Journal of Anaesthesia. 712-713

Nakagawa, K., T. Kamiya, K. Arakawa, S. Akiyama and K. Sakai (2015). "Objective and subjective comparison of the visibility of three echogenic needles and a nonechogenic needle on older ultrasound devices." *Acta Anaesthesiol Taiwan*.

Namba, K. (2014). *MR-guided Focused Ultrasound Surgery for Breast Cancer: Reliability and Effectiveness*

National-Statistics (2013). NHS Imaging and Radiodiagnostic activity in England. England, National Statistics**:** 1-7.

Nayar, V. T., J. D. Weiland, C. S. Nelson and A. M. E. Hodge (2012). "Elastic and viscoelastic characterization of agar." *J. Mech. Behav. Biomed. Mater* **7**: 60-68.

Nightingale, K., M. L. Palmeri, R. W. Nightingale and G. E. Trahey (2001). "On the feasibility of remote palpation using acoustic radiation force." *The Journal of the Acoustical Society of America* **110**(1): 625-634.

Nightingale, K., M. S. Soo, R. Nightingale and G. Trahey (2002). "Acoustic radiation force impulse imaging: in vivo demonstration of clinical feasibility." *Ultrasound in medicine and biology* **28**(2): 227-235.

Nimrod, M. T. (2005). Chapter 3: Interaction of ultrasound with matter. *Basic Physics of Ultrasonographic Imaging*
O. Harald, World Health Organisation.

Nyborg, W. L. M. and J. Wu (2006). *Emerging Therapeutic Ultrasound*. New Jersey, World Scientific.346

Odobescu, A., S. Moubayed, P. Harris, J. Bou-Merhi, E. Daniels and M. Danino (2014). "A new microsurgical research model using Thiel-embalmed arteries and comparison of two suture techniques." *J Plast Reconstr Aesthet Surg* **67**(3): 389-395.

Olympus (2015). "Beam Characteristics & Wave Propogation." Retrieved 06 Febraury, 2015, from http://www.olympus-ims.com/en/ndt-tutorials/flaw-detection/wave-propagation/.

Ophir, J., I. Céspedes, H. Ponnekanti, Y. Yazdi and X. Li (1991). "Elastography: A quantitative method for imaging the elasticity of biological tissues." *Ultrason Imaging* **13**(2): 111-134.

Optocon (2010). FOTEMP1 User Manual. O. O. S. a. Systems. Germany**:** 21.

Packer, M., W. Fishkind, I. Fine, B. Seibel and R. Hoffman (2005). "The physics of phaco: a review." *J Cataract Refract Surg* **31**: 424-431.

Pan, P., T. Bogard and M. Owen (2004). "Incidence and characteristics of failures in obstetric neuraxial analgesia and anesthesia: a retrospective analysis of 19,259 deliveries." *International Journal of Obstetric Anesthesia* **13**(4): 227-233.

Pan, X., C. Li, K. Ying, D. Weng, W. Qin and K. Li (2010). "Model-based PRFS thermometry using fat as the internal reference and the extended Prony algorithm for model fitting." *Magn Reson Imaging* **28**(3): 418-426.

Pattanshetti, V. M. and S. V. Pattanshetti (2010). "Laparoscopic surgery on cadavers: a novel teaching tool for surgical residents." *ANZ Journal of Surgery* **80**(10): 676-678.

Paul, E. B., A. O. Assad, C. B. Jeffery, P. B. Gearoid, D. Jean-Francois, R. F. Elizabete, G. Sevan and H. Timothy J (2015). Nonlinear and poroelastic Biomechanical Imaging:

Elastography beyond Young's modulus. *Handbook of Imaging in Biological Mechanics*. P. Corey and M. Guy. London, CRC Press.

Pavan, T., E. Masdsen, G. Frank, A. Carneiro and T. Hall (2010). "Nonlinear elastic behavior of phantom materials for elastography." *Phys Med Biol* **55**(9): 2679-2692.

Payne, A., R. Merrill, E. Minalga, U. Vyas, J. de Bever, N. Todd, R. Hadley, E. Dumont, L. Neumayer, D. Christensen, R. Roemer and D. Parker (2012). "Design and characterization of a laterally mounted phased-array transducer breast-specific MRgHIFU device with integrated 11-channel receiver array." *Med Phys* **39**(3): 1552-1560.

Payne, A., N. Todd, E. Minalga, Y. Wang, M. Diakite, R. Hadley, R. Merrill, R. Factor, L. Neumayer and D. L. Parker (2013). "In vivo evaluation of a breast-specific magnetic resonance guided focused ultrasound system in a goat udder model." *Med Phys* **40**(7): 073302.

Pengfei, S., L. Yutao, Y. Jie, W. Wuran, D. Yi, Z. Hao and W. Jia (2011). "The Results of ureteral stenting after ureteroscopic lithotripsy for ureteral calculi: a systematic review and meta-analysis. ." *J Urology* **186**: 1904-1909.

Peuker, E. T., R. Werkmeister, F. Pera, U. Joos and T. J. Filler (2001). "[Surgical procedures in mouth, jaw and facial surgery in Thiel embalmed body donors]." *Mund Kiefer Gesichtschir* **5**(2): 141-143.

Poorter, J., C. Wagter, Y. Deene, C. Thomsen, F. Ståhlberg and E. Achten (1995). "Noninvasive MRI Thermometry with the Proton Resonance Frequency (PRF) Method: In Vivo Results in Human Muscle." *Magnetic Resonance in Medicine* **33**(1): 74-81.

Prokop, A. F., S. Vaezy, M. Noble, P. Kaczkowski and R. Martin (2003). "Polyacrylamide gel as an acoustic coupling medium for focused ultrasound therapy." *Ultrasound in medicine and biology* **29**(9): 1351-1358.

Qiu, W., Y. Yu, H. Chabok, C. Liu, F. Tsang, Q. Zhou, K. Shung, H. Zheng and L. Sun (2013). "A Flexible Annular-Array Imaging Platform for Micro-Ultrasound." *IEEE Trans Ultrason Ferroelectr Freq Control* **60**(1): 178-186.

Qiu, Z. (2014). Development of MRI-compatible Transducer Array for Focused Ultrasound Surgery : The Use of Relaxor-based Piezocrystals. *School of Engineering*. Dundee, University of Dundee. **PhD:** 229.

Quesson, B., M. Merle, M. O. Kohler, C. Mougenot, S. Roujol, B. D. de Senneville and C. T. Moonen (2010). "A method for MRI guidance of intercostal high intensity focused ultrasound ablation in the liver." *Med Phys* **37**(6): 2533-2540.

Raju, P. and C. Grant (2013). "Practical aspects of ultrasound-guided regional anaesthesia." *Anaesthesia & Intensive Care Medicine* **14**(4): 137-141.

Ramanarine, K. V., T. Andeson and P. R. Hoskins (2001). "Construction and geometric stability of physiological flow rate wall-less stenosis phantoms." *Ultrasound Med Biol* **27**(2): 245-250.

Ramnarine, K. V., J. W. Garrard, K. Dexter, S. Nduwayo, R. B. Panerai and T. G. Robinson (2014). "Shear wave elastography assessment of carotid plaque stiffness: in vitro reproducibility study." *Ultrasound Med Biol* **40**(1): 200-209.

Reid, C., A. Lewis, K. Habig, B. Burns, F. Billson, S. Kunkel and W. Fisk (2013). "Sustained life-like waveform capnography after human cadaveric tracheal intubation." *Emerg Med J*.

Rewcastle, J. C. (2006). "High intensity focused ultrasound for prostate cancer: a review of the scientific foundation, technology and clinical outcomes." *Technology in Cancer Research & Treatment* **5**(6): 619-625.

Richard, B., M. Richard and c. Carl (2012). "Shear Wave Ultrasound Elastography of the Prostate- Initial Results." *Ultrasound Quarterly* **28**(1): 13-20.

Rieke, V. and K. Butts Pauly (2008). "MR thermometry." *J Magn Reson Imaging* **27**(2): 376-390.

Sarvazyan, A., A. Skovoroda, S. Emelianov, J. Fowlkes, J. Pipe, R. Adler, R. Buxton and P. L. Carson (1995). "Biophysical bases of elasticity imaging." *Acoustic Imaging* **21**: 223-240.

Sarvazyan, A. P., O. V. Rudenko, S. D. Swanson, J. B. Fowlkes and S. Y. Emelianov (1998). "Shear wave elasticity imaging: a new ultrasonic technology of medical diagnostics." *Ultrasound Med Biol* **24**(9): 1419-1435.

Schafhalter-Zoppoth, I., C. McCulloch and A. Gray (2004). "Ultrasound visibility of needles used for regional nerve block: An in vitro study." *Reg Anesth Pain Med* **29**(5): 480-488.

Schafhalter-Zoppoth, I., C. E. McCulloch and A. T. Gray (2004). "Ultrasound visibility of needles used for regional nerve block: an in vitro study. ." *Reg Anesth Pain Med* **29**: 480-488.

Serway, R. and C. Vuille (2011). Solids and fluids. *College Physics*. B. Killion. USA, Hartford, Charles. **1:** 283.

Sharma, M. and A. Horgan (2012). "Comparison of fresh-frozen cadaver and high-fidelity virtual reality simulator as methods of laparoscopic training." *World J Surg* **36**(8): 1732-1737.

Song, S., Z. Huang, T. M. Nguyen, E. Y. Wong, B. Arnal, M. O'Donnell and R. K. Wang (2013a). "Shear modulus imaging by direct visualization of propagating shear waves with phase-sensitive optical coherence tomography." *J Biomed Opt* **18**(12): 121509.

Song, S., Z. Huang and R. K. Wang (2013b). "Tracking mechanical wave propagation within tissue using phase-sensitive optical coherence tomography: motion artifact and its compensation." *J Biomed Opt* **18**(12): 121505.

Song, S., J. Joy, R. K. Wang and Z. Huang (2015). *Mapping tissue shear modulus on Thiel soft-embalmed mouse skin with shear wave optical coherence elastography*. Optical Elastography and Tissue Biomechanics II.93270Y-93270Y-93274

Steinborn, M., J. Fiegler, V. Kraus, C. Denne, A. Hapfelmeier, L. Wurzinger and H. Hahn (2011). "High resolution ultrasound and magnetic resonance imaging of the optic nerve and the optic nerve sheath: anatomic correlation and clinical importance." *Ultraschall Med* **32**(6): 608-613.

Stieger, C., C. Candreia, M. Kompis, G. Herrmann, F. Pfiffner, D. Widmer and A. Arnold (2012). "Laser Doppler vibrometric assessment of middle ear motion in Thiel-embalmed heads." *Otol Neurotol* **33**(3): 311-318.

Szabo, T. L. (2014). Chapter 16 - Elastography. *Diagnostic Ultrasound Imaging: Inside Out (Second Edition)*. T. L. Szabo. Boston, Academic Press**:** 699-733.

Takegami, K., Y. Kaneko, T. Watanabe, T. Maruyama, Y. Matsumoto and H. Nagawa (2004). "Polyacrylamide gel containing egg white as new model for irradiation experiments using focused ultrasound." *Ultrasound in medicine and biology* **30**(10): 1419-1422.

Tang, M. Y., T. W. Chen, X. M. Zhang and X. H. Huang (2014). "GRE T2-Weighted MRI: Principles and Clinical Applications." *Biomed Res Int* **2014**: 12.

Teirlinck, C. J., R. a. Bezemer, C. Kollmann, J. Lubbers, P. R. Hoskins, K. V. Ramnarine, P. Fish, K. E. Fredeldt and U. G. Schaarschmidt (1998). "Development of an example flow test object and comparison of five of these test objects, constructed in various laboratories." *Ultrasonics* **36**(1-5): 653-660.

ter-Haar, G. T. and F. Duck (2000). *The safe use of ultrasound in medical diagnosis*. London, British Institute of Radiology

Thiel, W. (1992a). "Die Konservierung ganzer Leichen in naturlichen Farben [The preservation of the whole corpse with natural color]." *Ann Anat* **174**: 185-195.

Thiel, W. (1992b). " Eine Arterienmasse zur Nachinjektion bei der Kon-servierung ganzer Leichen [An arterial substance for subsequent injection during the preservation of the whole corpse]." *Ann Anat* **174**: 197-200.

Thiel, W. (2002). "[Supplement to the conservation of an entire cadaver according to W. Thiel]." *Ann Anat* **184**(3): 267-269.

Timothy J, H., B. Mehmet, I. Michael F and K. Thomas A (1997). "Phantom Materials for Elastography." *IEEE transactions on Ultrasonics, ferroelectronics and frequency control* **44**(6): 1335-1365.

Torr, G. (1984). "The acoustic radiation force." *American Journal of Physics* **52**: 402–408.

Ultrasoundpaedia (2014). "Ultrasoundpaedia- a portal world of ultrasound." Retrieved December 18, 2014, from http://www.ultrasoundpaedia.com.

Unger, S., M. Blauth and W. Schmoelz (2010). "Effects of three different preservation methods on the mechanical properties of human and bovine cortical bone." *Bone* **47**(6): 1048-1053.

Unisciel (2013, 25th April 2015). "Mouse Dissection." from https://www.youtube.com/watch?v=KYSRjtYjiHA.

Ustun, Y., O. Erdogan, M. Kurkcu, T. Akova and I. Damlar (2008). "Effects of low-intensity pulsed ultrasound on dental implant osseointegration: a preliminary report." *Eur J Dent* **2**: 254-262.

VirtualMedicalCentre (2014). "Human Anatomy |myVMC." Retrieved 18 December 2014, from www.myvmc.com/anatomy.

Wells, P. and H. Liang (2011). "Medical ultrasound: imaging of soft tissue strain and elasticity." *J R Soc Interface* **8**(64): 1521-1549.

Wells, P. N. T. (2006). "Ultrasound imaging." *Physics in Medicine and Biology* **51**(13): R83-98.

Wendie, A., O. David, J. Caroline, K. Fritz, E. William, J. Regina, O. Ralf, B. Ellen, B. Catherine, L. Martina, T. Christophe, C. Barbara, J. Valérie, S. Thomas, T. Anne, G. Joel, J. Henry and C. Claude (2012). "Shear-wave Elastography Improves the Specificity of Breast US: The BE1 Multinational Study of 939 Masses." *Radiology* **262**(2): 435-449.

Wilke, H.-J., K. Werner, K. Häussler, M. Reinehr and T. M. Böckers (2011). "Thiel-fixation preserves the non-linear load-deformation characteristic of spinal motion segments, but increases their flexibility." *J Mech Behav Biomed Mater* **4**(8): 2133-2137.

Wlodarczyk, W., M. Hentschel, P. Wust, R. Noeske, N. Hosten, H. Rinneberg and R. Felix (1999). "Comparison of four magnetic resonance methods for mapping small temperature changes." *Phys Med Biol* **44**(2): 607-624.

Wolff, K.-D., M. Kesting, T. Mücke, A. Rau and F. Hölzle (2008). "Thiel embalming technique: A valuable method for microvascular exercise and teaching of flap raising." *Microsurgery* **28**(4): 273-278.

Wood, L. and A. Loomis (1927). "Physical and biological effects of high frequency sound waves of great intensity " *Philosophical Magazine* **14**: 417 - 436.

Wu, F., Z. Wang, Y. Cao, X. Zhu, H. Zhu, W. Chen and J. Zou (2007). ""Wide local ablation" of localized breast cancer using high intensity focused ultrasound." *Journal of Surgical Oncology* **96**(2): 130-136.

Wurm, S., H. Kainz, W. Reng and P. Augat (2013). "The influence of patellar resurfacing on patellar kinetics and retropatellar contact characteristics." *J Orthop Sci* **18**(1): 61-69.

Zell, K., J. I. Sperl, M. W. Vogel, R. Niessner and C. Haisch (2007). "Acoustical properties of selected tissue phantom materials for ultrasound imaging." *Phys Med Biol* **52**(20): N475-484.

Zhou, Y.-F. (2011). "High intensity focused ultrasound in clinical tumor ablation." *World Journal of Clinical Oncology* **2**(1): 8-27.

Zowall, H., J. Cairns, C. Brewer, D. Lamping, W. Gedroyc and L. Regan (2008). "Cost-effectiveness of magnetic resonance-guided focused ultrasound surgery for treatment of uterine fibroids." *BJOG* **11**: 5653-5662.

APPENDICES

APPENDIX I - TMM Recipes

This Appendix contains all the recipes for the TMMs prepared and tested in Chapter Three.

1. Evaporated Milk Liquid TMM

The recipe for the preparation of evaporated milk liquid TMM is adapted from existing protocol (Madsen 1998).The liquid low scatter TMM is a mixture of evaporated milk, distilled water, propan-2-ol and bio-cleanse. Some of these ingredients are slightly different from the original recipe due to the limited availability of exact chemicals. Thimersol, used to increase the anti-fungal properties of the TMM was replaced with bio-cleanse (Coalite Chemicals, Chesterfield, UK). In addition, propan-2-ol (Scientific & Chemical Supplies Ltd, Aberdeen, UK) was used instead of n-propanol. The quantity of materials needed for producing 1L of liquid evaporated milk TMM are shown in Table 14.

Table 14: Ingredients to prepare 1 L of evaporated milk liquid TMM.

Ingredient	Quantity
Distilled water	370ml
Propan-2-ol	30ml
Bio-cleanse	1.33g
Evaporated milk	800ml

The detailed step by step procedure to make the liquid TMM is as follows.

1) Combine the bio-cleanse and evaporated milk in a glass beaker.
2) Heat the mixture to 68^{o}C in a hot water bath/hot plate to reduce the viscosity of the mixture. Stir continuously for uniform heat distribution and to prevent any parts of the mixture reaching temperatures near 72^{o}C as this will start coagulating the milk solids.
3) Carefully filter the hot mixture using filter paper and cool the filtrate to 40^{o}C.

4) Combine distilled water and propan-2-ol in a 1L glass beaker and add the mixture to the filtered solution from step 3.
5) Degas the mixture in a vacuum chamber or by warming to 40^{o}C.
6) Cool the liquid TMM to 30^{o}C before storing in a phantom container.

(a) (b) (c)

Figure 82: (a) Preparing Liquid TMM, (b) Removing air bubbles in the vacuum chamber and (c) Prepared degassed TMM.

2. Evaporated Milk Solid TMM

The recipe for the preparation of evaporated milk solid TMM is adapted from existing protocol (Madsen 1998). The solid form of evaporated milk TMM is made from the same ingredients as for the liquid evaporated milk TMM except that there is an agarose component (Millipore Ltd, Feltham, UK) added to produce a solid TMM. It is important to use high purity agarose as impurities in agar can result in a relatively high echoic final product (Madsen 1998).The list of ingredients and quantities needed for making a 1L TMM are shown in Table 15.

Table 15: Ingredients to prepare 1 L of evaporated milk solid TMM.

Ingredient	**Quantity**
Distilled water	644ml
Propan-2-ol	56ml
Bio-cleanse	1.33g
Agar	28g
Evaporated milk	700ml

The detailed step by step procedure to make the solid evaporated TMM is as follows.

1) Combine distilled water and propan-2-ol at room temperature in a 1L beaker and rapidly mix the high purity agarose.
2) Cover the beaker with a plastic food wrap (pierced to control the pressure differences in and out the beaker) and warm up the solution in heated water bath until the mixture is transparent (around 90^{o}C).
3) Cool the molten agarose solution to 55°C by immersing the lower part of the beaker in a large container of cold water and stirring continually.
4) Repeat steps 1, 2 and 3 in the liquid TMM manufacturing procedure to produce a 500ml of filtrate evaporated milk solution.

5) Warm the 500 ml of filtered evaporated milk to 55°C.
6) Combine the 500 mL of 55°C evaporated milk with 500 mL of 55°C molten agarose and mix well.
7) After cooling to about 45°C, the liquid can be poured into any container and allowed to cool.

The solution solidifies at 36 ± 1°C and the evaporated solid TMM has a melting point of 80°C.

(a) (b) (c)

Figure 83: (a) Condensed milk TMM preparation, (b) Filtering and (c) Final preparation.

3. EPP Grey TMM

The recipe for the preparation of EPP grey TMM is adapted from existing protocols (Ramanarine 2001, Inglis 2006). EPP grey agarose base TMM is robust TMM with a life span of few years. This is highly uniform and robust and the ingredients required for its preparation are shown in Table 16.

Table 16: Ingredients to prepare 1 L of EPP Grey TMM

Ingredient	**Quantity**
Distilled water	832.94ml
99% Glycerol	119.86
10% Benzalkonium Chloride	48.9ml
Agar	31.8g
400 grain SiC	5.6g
3µm Al_2O_3 powder	10g
0.3µm Al_2O_3 powder	9.3g

Main steps of preparation as follows:

1. Weight 0.3 µm and 3 µm Al_2O_3 powder and SiC particles in to a mixing beaker. Mix this well with a dry spoon and set this aside.
2. Weigh agar separately and keep aside.
3. Measure degassed water, pour majority of it to a cooking beaker, and leave the rest in another beaker.
4. Add glycerol and 10% Benzalkonium chloride to the cooking beaker containing the water and place the cooking beaker to a water bath with stirrer attached.
5. Set-up the stirrer speed to 135 rev/min and leave running.
6. Add the left behind water, pour to the dry ingredients, and make it a fine paste.

7. Carefully add this paste to the cooking beaker stirring continuously.
8. Slowly add the agar without stopping the stirring.
9. Set the water bath temperature to 95°C and stirrer speed to 120 rev/min.
10. When the temperature inside the cooking beaker reaches 95°C, start the clock and set the stirrer speed to 110 rev/min.
11. The cooking time is 60-70 min. On completion of cooking time, set the heater temperature to 39 °C and stirrer speed to 100 rev/min.
12. When the TMM temperature reaches 40.3 °C, remove the cooking beaker from the water bath, pour the TMM to the container, and leave it overnight to set.

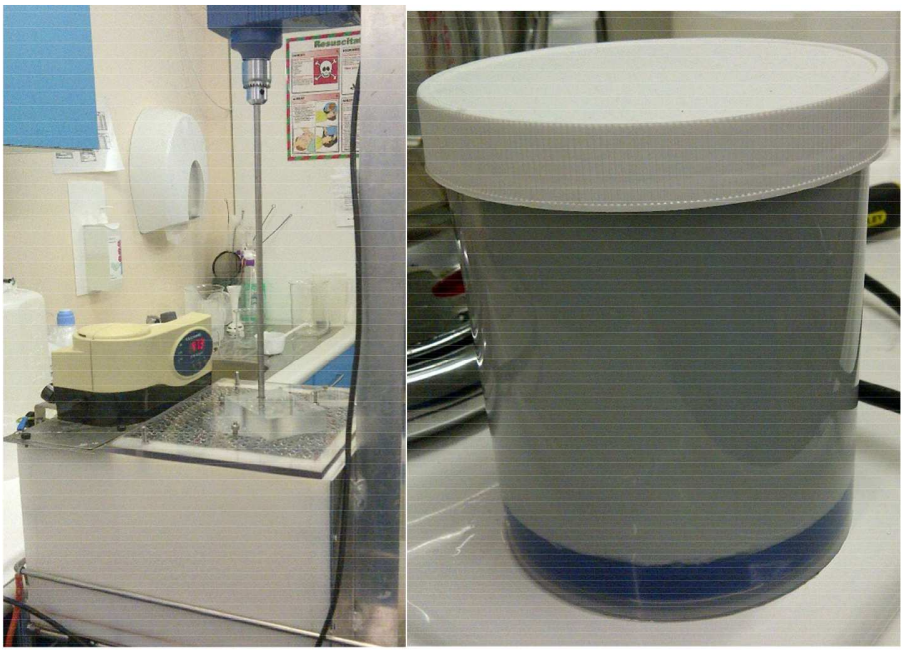

(a) (b)

Figure 84: (a) EPP TMM preparation and (b) prepared TMM (Courtesy- Royal Infirmary, Edinburgh)

4. Agar TMM

Agar TMM (Figure 85) has a very simple manufacturing procedure (Zell 2007). A 2% agar TMM requires 2% weight high purity agarose powder and 98% degassed water. The ingredients has to be combined and heated up to 160 degrees or until the agar component melts completely and a clear solution is obtained. Continuous stirring of the solution is needed throughout the heating process to avoid formations of lumps. Bubbles formed at the top of the mixture is removed and the mixture is poured to the container to set over night. The TMM has a low life span of only few weeks, but the simple manufacturing procedure increases its use.

Figure 85: Agar TMM

6. PAA Gel-based TMM

PAA based gel TMM is a clear TMM with fairly easy manufacturing process. However, precautions needs to be taken during preparation because of the neurotoxic and carcinogenic nature of monomer acrylamide. This TMM is specifically used for applications were a transparent material is required for testing such as photo-acoustic applications. The recipe for PAA was adapted from literature (Zell 2007). The ingredients needed to make 1 L PAA TMM is shown in Table 17.

Table 17: Ingredients for making 1 L of PAA TMM

Ingredient	**Quantity**
Degassed water	745 ml
40% w/v acryl amide + 2% w/v N,N-Methylene-bis Acrylamide*	162 ml
10% w/v ammonium peroxodisulfate(APS)	5 ml
TEMED	2 ml

*The recipe used 40% w/v acryl amide+ 2% w/v N, N-Methylene-bis-Acrylamide instead of 40% w/v acrylamide in the original recipe.

Main steps of preparation as follows:

1) Add acrylamide to degassed water and stir to combine. Any bubbles formed are carefully removed.

2) Add APS and TEMED to the mixture solution to catalyse the polymerization of acrylamide.

3) Pour mixture solution into the mould to set for approximately 30-45 minutes.

It is important that the mixture is poured to in to the container soon after addition of APS and TEMED as the solidification process can start momentarily and any delay in step 3 could introduce bubbles in the sample and can produce a non-uniform TMM. PAA should be stored in the fridge after wrapping it in plastic wrap or cling film to prevent evaporation of fluids. The TMM has a life span for few months.

5. PAA Gel-based HIFU TMM

PAA gel-based HIFU TMM is a relatively clear TMM almost the same manufacturing process as the PAA clear gel TMM. Like the name suggests, HIFU TMM is specifically used for focused ultrasound applications were a visible lesion need to be produced for testing. The recipe for PAA-HIFU TMM was adapted from literature (Teirlinck 1998, Prokop 2003, Gabriela 2007). The ingredients needed to make 1 L PAA TMM is shown in Table 17.

Table 18: Ingredients to make 1 L of PAA gel-based HIFU TMM.

Ingredient	Quantity
Degassed water	445ml
Fresh egg white	300ml
40% w/v acryl amide+ 2% w/v N,N-Methylene-bis-Acrylamide *	248 ml
10% w/v APS	5 ml
TEMED	2 ml

* The recipe used 40% w/v acryl amide+ 2% w/v N, N-Methylene-bis-Acrylamide instead of 40% w/v acrylamide in the original recipe.

Main steps of preparation as follows:

1) Separate the egg whites from the eggs at room temperature and add degassed water.

2) Stir the mixture at very low speeds to get rid of any clumps until a mixture of uniform consistency and colour is achieved. It is important to stir at low speeds to prevent air bubbles getting in to the solution.

3) If any air bubbles or foam is produced during stirring, remove them using a pipette.

4) Add acrylamide to the mixture while continuously stirred. Any bubbles formed are carefully removed.

5) Add APS and TEMED to the mixture solution to catalyse the polymerization of acrylamide.

6) Pour mixture solution into the mould to set for approximately 20-30 minutes. It is important that the mixture is poured to in to the container soon after addition of APS and TEMED as the solidification process can start momentarily and any delay in step 6 could introduce bubbles in the sample and can produce a non-uniform TMM.

This TMM should be stored in the fridge after wrapping it in plastic wrap or cling film to prevent evaporation of fluids. The TMM has a life span for few months.

APPENDIX II – MRI Compatible FUS chamber: Design and development

This Appendix describes the main steps during the designing and development of the MRI compatible FUS chamber used for TEC breast HIFU experiments in Chapter Six.

Table 19: Design and development of MRI compatible HIFU chamber.

<table>
<tr>
<td>Step 1: Chamber designing
 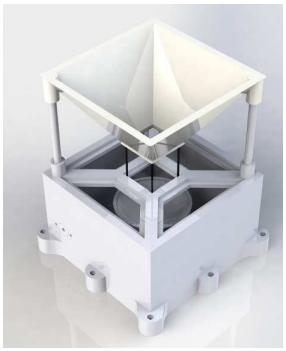 </td>
<td>Step 2: Laser cutting the Perspex sheets
  </td>
</tr>
<tr>
<td>Step 3: Building the glass chamber
  </td>
<td>STEP 4: Applying 3 coats of adhesion promoter
 
</td>
</tr>
<tr>
<td>Step 5: Applying 3 coats of matt lacquer
 
</td>
<td>STEP 6: Gluing the glass chamber and support rods
 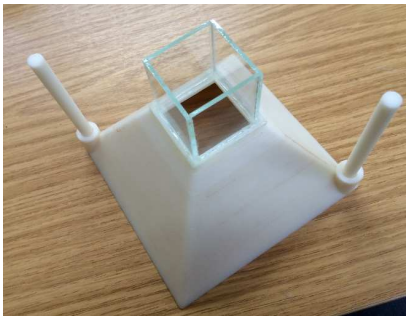 </td>
</tr>
</table>

STEP 7: Gluing the Perspex and applying the putty 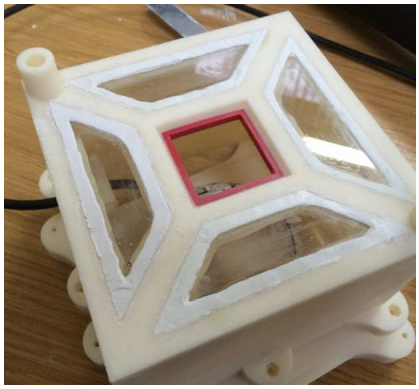	STEP 8: Gluing the glass chamber to the base 
STEP 9: Attaching the base with the screws 	STEP 10 :Applying the hard glue to the base